UC San Diego

Title

Ultrafast Dynamics and Control in Layered Transition Metal Oxides

Permalink

Author

Kaj, Kelson James

Publication Date

2023

UNIVERSITY OF CALIFORNIA SAN DIEGO

Ultrafast Dynamics and Control in Layered Transition Metal Oxides

A dissertation submitted in partial satisfaction of the
requirements for the degree
Doctor of Philosophy

in

Physics

by

Kelson Kaj

Committee in charge:

Professor Richard Averitt, Chair
Professor Shaya Fainman
Professor Michael Fogler
Professor Oleg Shpyrko
Professor Wei Xiong

2023

The dissertation of Kelson Kaj is approved, and it is acceptable in quality and form for publication on microfilm and electronically.

University of California San Diego

2023

DEDICATION

Dedicated to my parents, who have always encouraged and supported me.

EPIGRAPH

The data's the data.

—Rick

TABLE OF CONTENTS

LIST OF FIGURES

ACKNOWLEDGEMENTS

Completing a PhD in physics is a fun but long and difficult task. This was made even more difficult by the majority of this time also coinciding with a global pandemic which makes every aspect of performing research and completing the degree more difficult. Although I am proud to have accomplished this, my ability to make it through and finish this PhD is in large part to the many different people who have helped me along the way, who I can only begin to express their greatness and importance to me in this section.

The most important person for my PhD is my advisor, Dr. Richard Averitt. I first of all would like to thank him for allowing me to join his lab and take a chance on me, I'm aware going into things it's hard to know which students will work out in an experimental lab. Although I had some previous research experience, the PhD is really where I learned how to be a scientist, and Rick is the main person I learned this from. He has certainly shaped my philosophy towards experimental physics, how to think about physics, how to design experiments and plan data collection, and how to think about the data we have. He has also done a good job both through teaching and leading by example of how to go about science and research with integrity. His interactions with other scientists I also see as a great example that one can be successful while remaining nice and encouraging at all times. I and my peers have also all been subject to his infectious excitement about science as well. Rick has a very hands-off advising style, which allows his students the freedom to do what we want in terms of projects and how we progress on experiments in lab. This allows us to make mistakes and learn from them in lab, and creates independent students from his lab. Rick has also been extremely helpful in teaching me scientific writing, and this area is one that I started with nearly 0 knowledge of and have learned so much of during my PhD. Overall Rick has made my PhD in his lab as enjoyable as possible.

Nearly as important as my advisor are the other members of the Averitt Lab during my PhD. First of all, when I joined the lab there was the previous generation in the last year or two of their PhDs who I learned a huge amount from. These students and mentors are those of which I learned nearly all of the nitty-gritty

details and hands-on lab techniques needed for ultrafast and THz experiments. Even if there aren't specific publication-collaborations we did together, I learned many extremely important things from Kevin, Peter, Gufeng, Jacob, and Dylan, and I am extremely aware and grateful for this. On the other hand there are also my peers in the Averitt Lab, Ian, Varun, Mustafa, Peter, Max, Yuan, and Erick. Once the older generation had graduated, the lab was left to us, and it has been a pleasure to learn physics and running experiments alongside them, both from directly working together on some experiments and observing and discussing each others experiments. In addition to the science, both the older generation and my peers in the Averitt Lab have been part of friendships that has made completing a PhD during a global pandemic not only tolerable but enjoyable. Although graduation is somewhat of an end to one era of my life I am happy to know that the friendships formed in the Averitt Lab will last for the rest of our lives.

Outside of the Averitt Lab, there are many important collaborations that allowed the science to get done. The closest collaboration during my PhD has been with the group of Dr. Xin Zhang at Boston University, specifically with Yuwei, Chunxu, Xiaoguang, and Zhiwei. Specifically collaborating with Yuwei and Chunxu during their PhDs we were able to complete quite a few projects together, and I have learned a great deal from working with them. This group has experts in many key fabrication techniques for metamaterials and MEMS, and for all metamaterial projects, those within this thesis and others, they did all of the fabrication and consistently made high quality samples.

There are many other collaborations that have been important for my PhD. At UCSB, Alex, Andrea, and Abhay have all been key collaborators looking at THz spectroscopy of superconductors and discussing some finer details of pump-probe experiments. From Cornell, Anita and Andrej led x-ray experiments on Ca_2RuO_4 and were key in discussions related to my THz measurements. Additionally at Cornell Darrell, Kyle, and Hari grew the films in the experiment. I have also had many great conversations about phonons and photoinduced phase transitions with Jeff, Guru, and Sabrina at Cornell. Related to the LSCO-MM project, Dmitri at

Columbia and Michael Fogler at UCSD have helped with great discussions. Some other helpful collaborators with various topics in condensed matter physics and optics are Danilo and James at Northwestern, Hugo at Penn State, Oleg and Erik at UCSD, Thomas Gebert at wiredsense, and Jak and Michael at Rutgers.

As is the case with many PhDs working with lasers, I dealt with a fair deal of laser trouble and time with our laser being down. However there would have been much more time of our laser being down without the help of Dennis Merritt at Spectra. He was very consistently reachable and helpful via email for discussions of our laser system. He was also extremely candid and knowledgeable when he came to fix parts of our laser on service calls.

I have also taken many classes from the UCSD physics department in my time here that have shaped my understanding and thinking in physics. I want to particularly acknowledge Dr. John McGreevy, who I was fortunate enough to take six classes under. I have learned a wide variety of physics in these classes, and Dr. McGreevy has undoubtedly shaped my physical thinking as well.

My life during grad school and the completion of my thesis is also largely thanks to those in my personal life who have helped me along the way. I first of all need to thank my parents, both for their help and encouragement during my time in grad school, but also for putting high value on education while raising me, while at the same time allowing me to follow my passions and be independent. I also want to thank my girlfriend Alexis for constant encouragement and support during my PhD. Finally my close friends and roommates during my PhD, Ben, Eric, David, and Miranda were all instrumental in making my time during grad school enjoyable.

Schalch, Jacob; Huang, Yuwei; Fogler, Michael; Basov, Dmitri N.; and Averitt, Richard D. *In Preparation.* The dissertation author was the primary investigator and first author of the paper.

Chapter 6 is in full a reprint of the material being prepared for submission. Kaj, Kelson; Verma, Anita; Ramaprasad, Varun, Nair, Hari P.; Schlom, Darrel G.; Shen, Kyle M.; Singer, Andrej; and Averitt, Richard D. *In Preparation.* The dissertation author was the primary investigator and first author of the paper.

VITA

2017	B. S. in Physics *Summa Cum Laude*, University of California San Diego
2017-2019	Graduate Teaching Assistant, University of California San Diego
2023	PhD. in Physics, University of California San Diego

PUBLICATIONS

Kelson Kaj, Kevin Cremin, Ian Hammock, Jacob Schalch, Dmitri N. Basov, Richard D. Averitt. "*Terahertz Third Harmonic Generation in C-Axis $La_{1.85}Sr_{0.15}CuO_4$*" Phys. Rev. B **107**, L140504 (2023).

Kelson Kaj, Ian Hammock, Chunxu Chen, Xiaoguan Zhao, Kevin Cremin, Jacob Schalch, Yuwei Huang, Michael Fogler, Dmitri N. Basov, Xin Zhang, Richard D. Averitt. "*Terahertz Metamaterial Strong Coupling with Superconducting Josephson Plasmons in $La_{1.85}Sr_{0.15}CuO_4$*" *To be submitted* (2023).

Kelson Kaj, Anita Verma, Varun Ramaprasad, Hari P. Nair, Darrel G. Schlom, Kyle M. Shen, Andrej Singer, Richard D. Averitt. "*Photoinduced Insulator-to-Metal Transition Dynamics in Ca_2RuO_4*" *To be submitted* (2023).

Anita Verma, Denis Golez, Oleg Gorobtsov, **Kelson Kaj**, Ryan Russel, Guru B. S. Khalsa, Erik Lamb, Jeffrey Z. Kaaret, Hari P. Nair, Y. Sun, R. Bouck, Nathaniel Schreiber, Jacob P. Ruf, Y. Kubota, Vladmir A. Stoica, Hari Padmanabhan, John W. Freeland, Nicole A. Benedek, Oleg Shpyrko, John W. Harter, Richard D. Averitt, Darrel G. Schlom, Kyle M. Shen, Andrew J. Millis, Andrej Singer. "*Picosecond Volume Expansion Drives a Later-Time Insulator-Metal Transition in a Nano-Textured Mott Insulator*" **arxiv:2304.02149**, *Under Review* (2023).

Yuwei Huang, **Kelson Kaj**, Chunxu Chen, Zhiwei Yang, Xiaoguang Zhao, Richard D. Averitt, Xin Zhang. "*Tunable Bound States in the Continuum in a Reconfigurable Terahertz Metamaterial*" *Under Review* (2023).

Alex M. Potts, Abhay K Nayak, Michael Nagel, **Kelson Kaj**, B. Stamenic, D. D. John, Richard D. Averitt, Andrea F. Young. "*On-chip time-domain Terahertz spectroscopy of superconducting films below the diffraction limit*" ACS Nano Letters **23**, 3835 (2023).

Yuwei Huang, Xuefei Wu, Jacob Schalch, Guangwu Duan, Chunxu Chen, Xiaoguang Zhao, **Kelson Kaj**, Hai-Tian Zhang, Roman Engel-Herbert, Richard D. Averitt, Xin Zhang. "*Complementary Vanadium Dioxide Metamaterials with Enhanced Modulation Amplitude at Terahertz Frequencies*" Phys. Rev. App. **18**, 054086 (2022).

Chunxu Chen, **Kelson Kaj**, Xiaoguan Zhao, Yuwei Huang, Richard D. Averitt, Xin Zhang. "*On-demand terahertz surface wave generation with microelectromechanical-system-based metasurface*" Optica **9**, 17-25 (2022).

Yuwei Huang, **Kelson Kaj**, Chunxu Chen, Zhiwei Yang, Sheikh R. Haque, Yuan Zhang, Xiaoguang Zhao, Richard D. Averitt, Xin Zhang. "*Broadband Terahertz Silicon Membrane Metasurface Absorber*" ACS Phot. **9**, 1150 (2022).

Chunxu Chen, **Kelson Kaj**, Yuwei Huang, Xiaoguang Zhao, Richard D. Averitt, Xin Zhang. "*Tunable toroidal response in a reconfigurable terahertz metamaterial*" Adv. Opt. Mat. **9**, 2101215 (2021).

Xiaoguang Zhao, Chunchu Chen, **Kelson Kaj**, Ian Hammock, Yuwei Huang, Richard D. Averitt, Xin Zhang. "*Terahertz investigation of bound statesin the continuum of metallic metasurfaces*" Optica **7**, 1548 (2021).

ABSTRACT OF THE DISSERTATION

Ultrafast Dynamics and Control in Layered Transition Metal Oxides

by

Kelson Kaj

Doctor of Philosophy in Physics

University of California San Diego, 2023

Professor Richard Averitt, Chair

Ultrafast and time-resolved THz techniques have emerged as an important tool not only for measuring the equilibrium properties of quantum materials, but also for exhibiting control over their phases and degrees of freedom. This thesis focuses on the use of THz light to drive nonlinearities, probe strong coupling, and probe photoinduced phase transitions in layered transition metal oxides. After a brief introduction to the thesis in chapter 1, the physics behind the materials discussed in this thesis will be described in chapter two. Then an introduction to the experimental techniques used in this thesis will be given in chapter three. Chapter four consists of a project measuring the THz nonlinearities in a superconducting cuprate. Strong coupling in the THz range on the same superconducting cuprate is the subject of chapter five. Finally, experiments concerning the photoinduced insulator-to-metal transitions are discussed in chapter 6. This will be followed by a conclusion, summarizing the work of this thesis.

Chapter 1

Introduction

Quantum materials, and more specifically transition metal oxides, are a class of materials that lie at the forefront of current research in condensed matter physics. First, this is because of the wide array of material phases that can be realized including superconductivity, exotic magnetism, and Mott transitions, and the uses of these phases in devices and real world applications[2]. Secondly, quantum materials and transition metal oxides are complicated, and are generally made up of multiple competing degrees of freedom and nearby energy scales, which makes understanding them a long process which must utilize a wide variety of experimental and theoretical methods[2]. However, to bridge between studying quantum materials because they are interesting and complicated, and their possible real-world applications necessitates understanding how to control the properties and phases of these materials. There are many well-studied static methods to tune the properties of quantum materials, such as strain, chemical doping, magnetic field, and many more[2, 3, 4]. Another, newer, tuning knob for material properties is the use of light, and specifically the use of ultrafast light[2, 3, 4]. The use of ultrashort laser pulses allows researchers to tune (pump) and measure (probe) materials on their intrinsic timescales ranging from nanoseconds to femtoseconds. Along with advances in making pulses shorter over recent decades, there have also been many important advances in generating pulses of light near the energy scale of many of the most important excitations in quantum materials. In particular, this includes the THz range ($\sim$0.1 - 30 THz)[5]. The goal of the research in this thesis is to

use ultrafast pulses and THz light to study and control the phases of some layered transition metal oxides, which exhibit a variety of phases that occur due to their correlated nature.

The thesis will be organized as follows. Chapter 2 will introduce the relevant physics concepts for understanding the materials shown in this thesis and their interaction with light. It will introduce the physics of cuprate superconductivity and $La_{1.85}Sr_{0.15}CuO_4$ (LSCO), which is the material studied in two projects of chapters 4 and 5. An introduction to the experimental techniques used in this thesis, THz spectroscopy and pump-probe spectroscopy, makes up chapter 3. The first study of LSCO, THz-third harmonic generation from the Josephson Plasma Mode, is the subject of chapter 4. Chapter 5 is a THz study of coupling of the Josephson plasma mode in LSCO to metamaterial resonators. Pump-probe dynamics of the photoinduced insulator-to-metal transition in Ca_2RuO_4 are the subject of chapter 6. This thesis will then conclude and mention some possible future directions in chapter 7.

Chapter 2

Introduction to Layered Transition Metal Oxides and their Optical Properties

Contained within this thesis are studies of strongly correlated materials using THz and ultrafast light. A huge variety of phenomena have been observed in strongly correlated materials, but the two that will be focused on in this thesis are insulator-metal transitions and high-temperature superconductors. I will review some of the physics related to both of these phenomena, specifically focusing on the equilibrium physics of these phases and materials. This is to set the stage for studying these materials with ultrafast and nonlinear optics as discussed in subsequent chapters.

2.1 Strongly Correlated Mott Insulators

2.1.1 Band Theory of Solids and Basic Optical Properties

Before tackling the problem of strongly correlated (i.e., strongly interacting) solids, we will first review some of the basic properties of non-interacting solids. The properties of many non-interacting solids are well-explained by the band theory of electrons[6, 7]. Atoms in a periodic potential can be described by Bloch
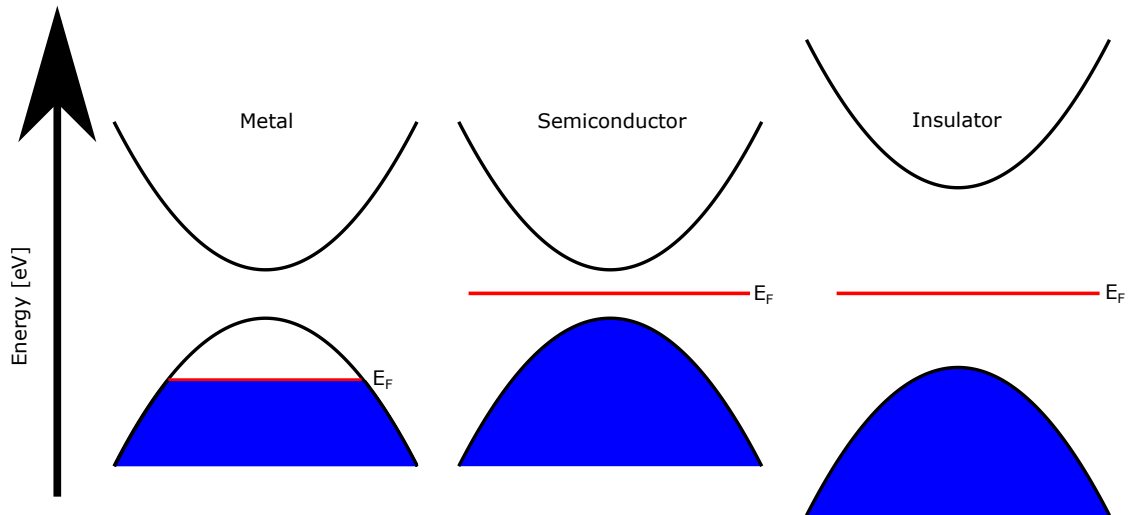
Figure 2.1: Schematic of band structure for a metal, semiconductor, and insulator. Here all three have a lower valence band and upper conduction band, separated by an energy gap. The Fermi energy is given by the horizontal red line labelled E_f. The filling of electrons in the bands goes up to the Fermi energy, and the filled states are shaded blue. The metal has the Fermi energy lying within the band, whereas both the semiconductors and insulators have the Fermi energy in the gap between the bands. The only difference between the semiconductor and insulator is that the gap between the bands is larger for an insulator.

wavefunctions with well defined momentum and energies that lie in various energy bands[6, 7]. For a non-interactiong solid, the bandstructure can be solved related to the positions of the ions that make up the crystal, and then these bands are filled with electrons up to the Fermi level[6, 7]. Metals can then be understood as materials where the band is partially filled with the Fermi level lying within the band. Semiconductors and insulators are then materials with a completely filled band where there is a bandgap and the Fermi level is in the middle of the gap between the conduction and valence band. Semiconductors are when this gap is small, and insulators are when this gap is large, with the crossover between these two not being a hard definition, but is generally around 1.5 eV. A schematic of band structure for these three types of solids is shown in figure 2.1, where the same band structure can be metallic or insulating depending on the Fermi level or filling of the material.

The band picture of solids along with the Drude model can describe some

of the basic optical properties of solids[8, 6, 7]. Non-correlated metals and their interaction with light were first described by the Drude model. Here all interactions and scattering are phenomenologically captured by an effective scattering time, which is the average time between conduction electron scattering events. This gives the following equation of motion for an electron in the presence of an electric field.

$$\frac{dp}{dt} = -eE - \frac{p}{\tau} \tag{2.1}$$

Here p is the electron's momentum, E is the applied electric field, e is the electron charge, and τ is the Drude scattering time. When the electric field is at a finite frequency, the frequency domain form of this equation can be used, and this can be simplified to give the following relation between the applied electric field and the momentum of electrons, which can be related to the current through $j = -enp/\omega$ with n being the density of electrons.

$$-i\omega p(\omega) = -eE(\omega) - \frac{p(\omega)}{\tau} \tag{2.2}$$

$$j(\omega) = \frac{e^2 n/m}{\frac{1}{\tau} - i\omega} E(\omega) \tag{2.3}$$

Where ω is the frequency of the applied field, n is the density of electrons, and m is their effective mass. The final equation shows a proportionality between the applied electric field and a current density, so through Ohm's law this gives a conductivity.

$$\sigma(\omega) = \frac{ne^2\tau/m}{1 - i\omega\tau} \tag{2.4}$$

This is the Drude optical conductivity, describing the currents at a given frequency for an applied electric field. The numerator of equation 2.4 has units of frequency squared, and defines the plasma frequency of a metal, $\omega_p^2 = ne^2\tau/m$. This form of the optical conductivity holds for a wide variety of metals, where both the plasma frequency and scattering times can vary by orders of magnitude. Two examples of optical conductivity are shown in figure 2.2. The conductivity is shown for two choices of parameters, when the scattering rate $(1/\tau)$ is equal to the plasma

frequency, and where it is 10 times larger than the plasma frequency. First, when $\omega_p = 1/\tau$, the real part of the conductivity is peaked at 0 frequency (sometimes referred to as the Drude peak), and gradually falls of, with magnitude related to the plasma frequency as $\sigma(0) = \omega_p^2 \tau$ and a width related to the scattering rate. The imaginary part is 0 at 0 frequency, and rises to a maximum at $\omega = 1/\tau$, which is also where it is equal to the real part. The conductivity where the scattering rate is larger than the plasma frequency is also shown in purple and green curves of figure 2.2. If plotted over a larger frequency, the same overall features as the red and blue conductivity would be seen, except much broader. However, it can be seen that the optical conductivity in this frequency range exhibits an overall flat real part and a very small imaginary part that only becomes significant at the highest frequencies. What this illustrates is that a flat optical conductivity that is dominated by the real part is consistent with the Drude model when measured over a finite frequency range. This is a very common case for many strongly correlated transition metal oxides, which often have stronger interactions (and more defects)[9, 10, 11, 12], making scattering rates much larger (compared to the plasma frequency) than cleaner systems, such as doped semiconductors[13].

Another response function that gives information about solids is the dielectric function which is related to the index of refraction and optical conductivity as follows:

$$n = \sqrt{\epsilon} \tag{2.5}$$

$$\sigma = \frac{\omega}{4\pi}(1 - i\epsilon) \tag{2.6}$$

where n is the index of refraction, ϵ dielectric function, and σ is the optical conductivity. Some details of extracting these response functions will be discussed in Chapter 3 of this thesis, but in short the index of refraction can be calculated from the reflection and transmission of light, from which the dielectric response and/or optical conductivity can be determined.

$$r = \frac{n_1 - n_2}{n_1 + n_2} \tag{2.7}$$
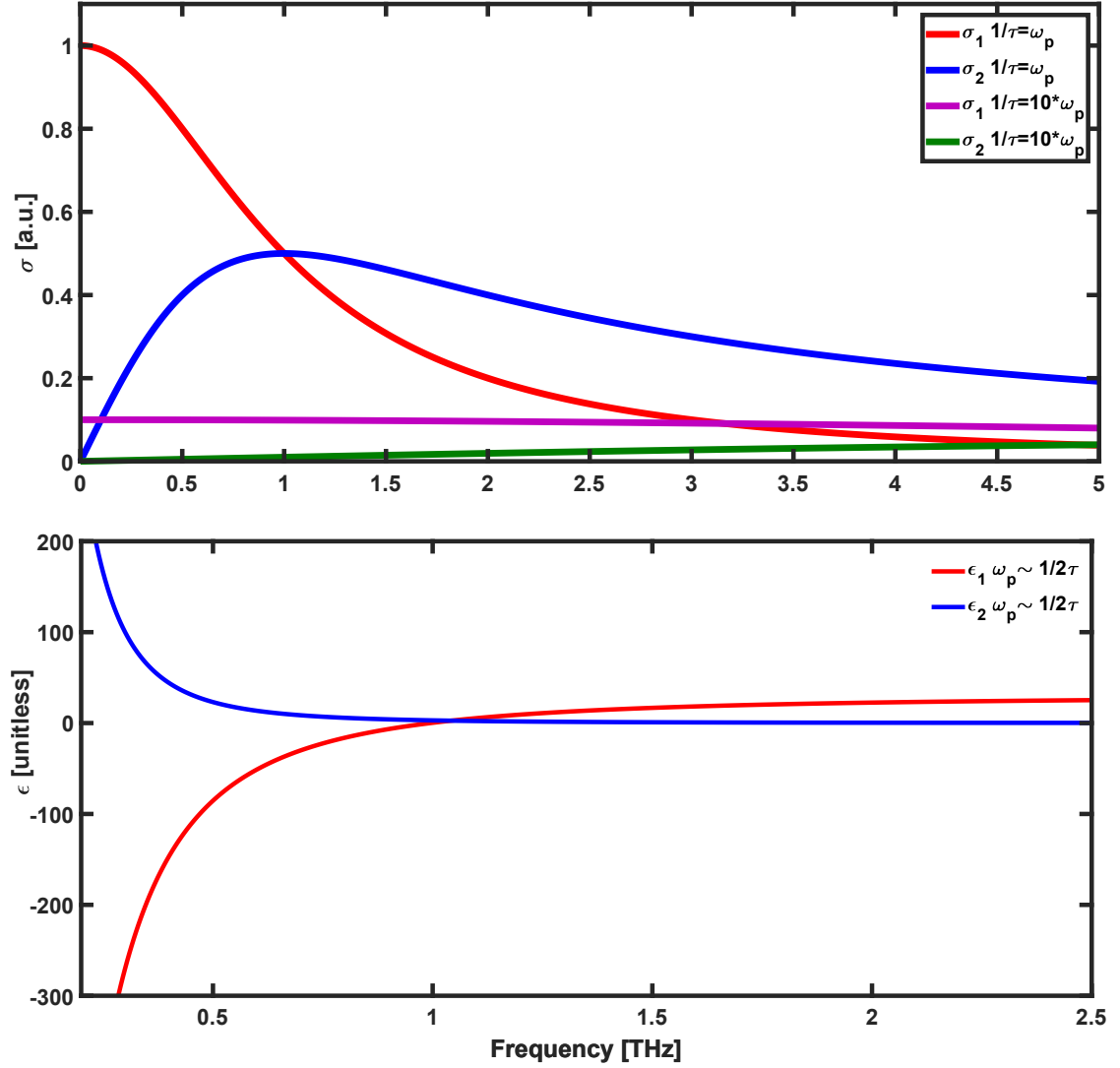
Figure 2.2: a) Optical Conductivity of the Drude model where the plasma frequency is equal to the scattering rate (red and blue) or is one tenth of the scattering rate (purple and green). b) Dielectric function for the Drude model when the plasma frequency is approximately one half the scattering rate.

$$t_{12} = \frac{2n_1}{n_1 + n_2} \tag{2.8}$$

The dielectric function for the Drude model is shown in figure 2.2 for a plasma frequency of 1 THz. The real part of the dielectric function, shown in red, goes from positive above the plasma frequency to negative and decreasing with a $-1/\omega^2$ dependence below the plasma frequency. The real part of the dielectric function crosses zero near the plasma frequency (only slightly shifted by the scattering rate contribution). This crossover at the plasma frequency is when a metal goes from transparent above the plasma frequency, where ϵ is not too large and not all light reflects, to highly metallic and reflective below the plasma frequency, where ϵ becomes very large in magnitude. The imaginary part of ϵ for the Drude model is always positive, and increases with decreasing frequency.

A key to the previously described understanding of materials is that they do not include electron-electron interactions, except in the phenomenological Drude scattering time. First of all, if these correlations were taken into account it would make the phenomenological equation of motion for electrons in the Drude model much harder to solve. However, if the electron-electron interaction is strong enough, this energy can dominate over the kinetic energy and cause the ground state of electrons in the solid to instead be composed of localized electrons in order to minimize the interaction energy, leading to an insulating state. This means that the drude model will not be a valid description of electrons in the solid, even if the non-interacting band structure and fermi energy would predict metallic behavior.Although these materials are where many of the interesting phenomena studied in modern condensed matter physics lie, the band theory of solids and the Drude model are still very helpful in building an intuition for how electrons behave in solids and interact with light before more realistic complications are taken into account.

2.1.2 Correlated Electron Materials

Taking electron-electron interactions into account makes the problem of modeling solids much more complicated. In the non-interacting picture, the band structure can essentially be calculated from the ionic potential, and then electrons

fill up these states up to the Fermi-energy. However, in correlated materials the makeup of the states that electrons fill is related to the filling of those electrons, since they interact strongly with each other. The effects of electron correlations can be made apparent with one of the simplest models of interacting electrons in a solid, the Hubbard model, which has the following hamiltonian[14].

$$H = -t \sum_{<i,j>,s} c_{i,s}^{\dagger} c_{j,s} + U \sum_{i} n_{i,\uparrow} n_{i,\downarrow} \tag{2.9}$$

Here i is the index for a given site, $c^{\dagger}$ and c are the creation and annihilation operators for electrons, t is the hopping matrix element from site to site, and U is the energy cost of having two electrons occupying the same site, which comes from coulomb repulsion. If t is held constant, changing the strength of U tunes how important electron-electron interactions are to the band structure, although in reality it is the ratio of U/t that is important, and oftentimes t (which is related to the bandwidth of a given band) is what changes the most for given tuning parameters. The effect of electron-electron interactions can be made most apparent by looking at two extreme cases of the Hubbard model at half filling, $U = 0$ and $U = \infty$.

First, for $U = 0$, the Hubbard hamiltonian can be made diagonal by using momentum space creation and annihilation operators $c_k = \sum e^{ikx} c_x$ [15]. This gives a bandstructure with dispersion $\epsilon(k) = -2tcos(k)$. For half-filling, which is one electron per site (full filling is two electrons per site since electrons are spin 1/2, this puts the Fermi-energy in the middle of the band, giving a metal. On the other hand, for $U = \infty$ (more realistically $U >> t$, the coulomb repulsion will dominate over any energy saved by electron-electron hopping, and the ground state in this case will be one electron confined to each site, with an energy cost U to doubly occupy a site. Here the electrons become localized to minimize the coulomb repulsion energy, so instead of having states that are spread out in space with well-defined momentum, the states do not have a well-defined momentum but are localized in space. The schematic density of states for these two cases are shown in figure 2.3 from [16]. The key takeaway is that, contrary to non-interacting band structure where being a metal or insulator simply depends on

where the Fermi energy is, in correlated materials Coulomb repulsion can make a material that would otherwise be metallic (since in the non-interacting case the Fermi energy is in the middle of a band) an insulator. This type of insulator is called a Mott Insulator.

2.1.3   Insulator-to-Metal Transition in Ca_2RuO_4

The Mott insulator that is studied in detail in this thesis is Ca_2RuO_4. It hosts a variety of phases, particularly when doped with strontium, including multiple structural phases, insulating and metallic phases, antiferromagnetism, orbital order, and even superconductivity [17]. What is most relevant here is that it undergoes a metal-insulator transition at $\sim 360K$[18], as shown by the drop in resistivity in 2.4a. The metal-insulator transition is caused by a structural transition at the same temperature[18, 19], as seen by the jump in the b-axis and drop in the a-axis in 2.4. The structure of calcium ruthenate is that of a Ruddlesden-Popper perovskite, where the octahedra of ruthenium-oxide are organized in quasi-2d planes separated by calcium-oxygen layers. A picture of the structure of Ca_2RuO_4 is shown in figure 2.4c. The hopping integrals, and therefore the electronic bandwidth in Ruddlesden-Popper ruthenates is very sensitive to the octahedral rotations and distortions[19]. Upon cooling below 360K, there is a lengthening of the c-axis, and a large orthorhombic distortion that involves an increase of Ru-O octahedral rotation about the x-axis and a tilt of the Ru-O basal planes [18, 19]. This change in structure changes the bandwidth of the Ru-d bands to be smaller than the Coulomb interaction strength, leading to a Mott insulating state and a metal-insulator transition.

The coexistence of a structural transition with the metal-insulator transition is a fairly common trait, seen in Ca_2RuO_4, $NdNiO_3$, VO_2, and V_2O_3 [18, 20, 21, 22, 23, 24, 25]. An unfortunate byproduct of this is that cycling through the insulator-to-metal transition causes cracks and structural defects to form, which makes studying the transition, particularly with ultrafast stroboscopic measurements, very difficult[20]. One solution to this is to (instead of studying bulk crystal samples) study epitaxially grown thin films, which are more stable to cycling
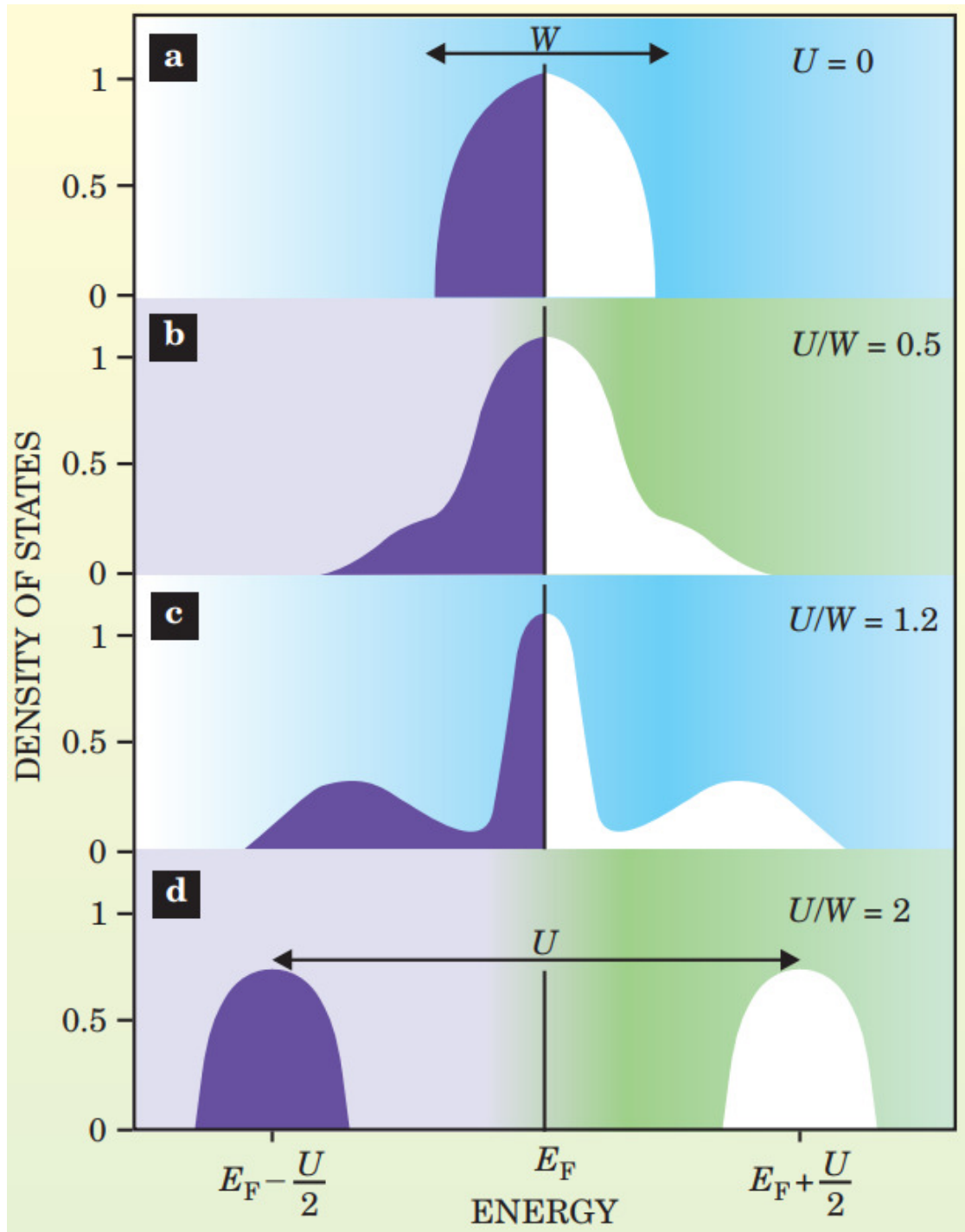
Figure 2.3: From [16] Schematic of the density of states in a material where the ratio of Coulomb repulsion to bandwidth (U/W)is varied to make a half-filled metallic band (a) eventually turn into an insulator (d).

11
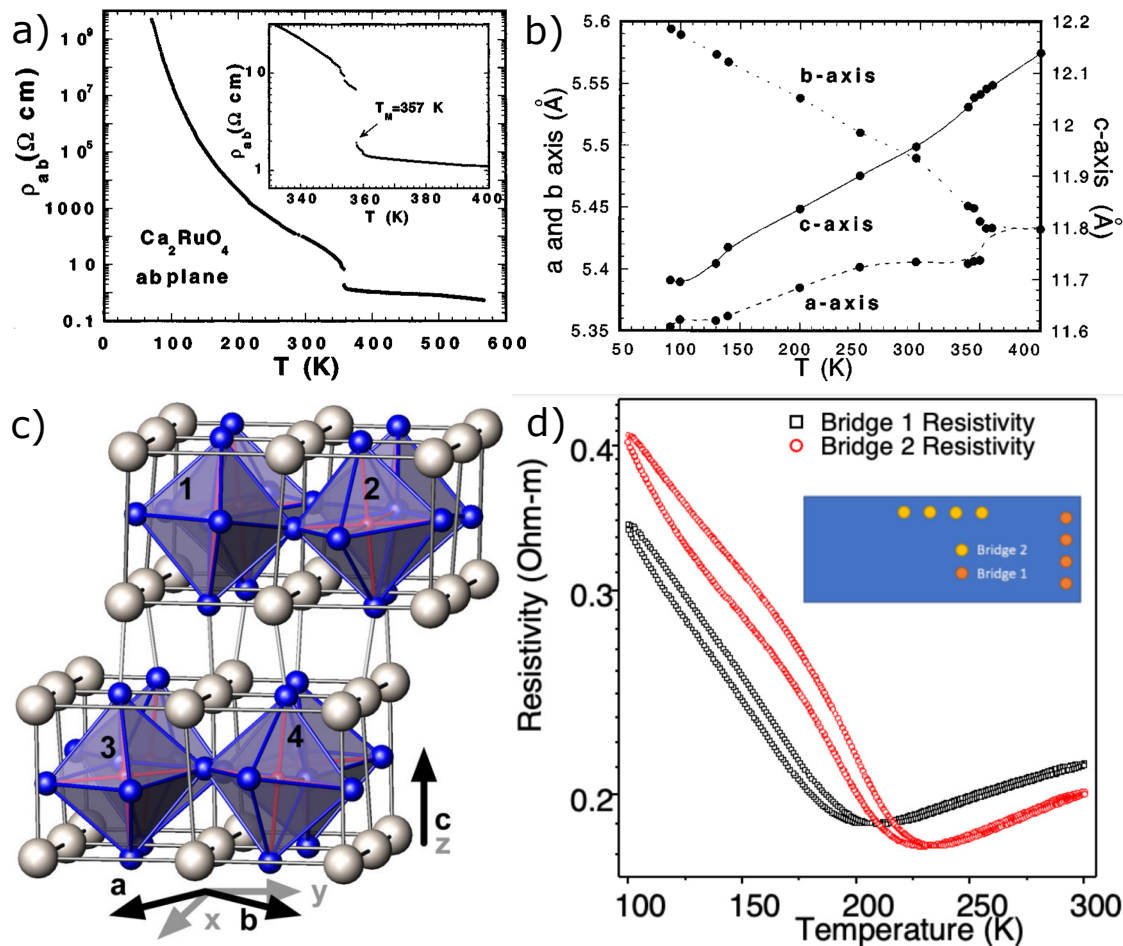
Figure 2.4: a) Resistivity and b) Lattice constants of Ca_2RuO_4 as a function of temperature, showing an insulator to metal transition occurring along with a structural transition at 357K. c) An image of the crystal structure of Ca_2RuO_4. d) Resistivity of a Ca_2RuO_4 thin film on $LaAlO_3$. a), b) from [17], c) from [18], and d) from [27].

through the transition, largely because they are much thinner and have their structure clamped to the bulk substrate. A substrate that calcium ruthenate can be grown on that still preserves the insulator-to-metal transition is lanthanum aluminate (LAO)[26, 27]. On LAO, the IMT in Ca_2RuO_4 occurs at $\sim 220K$, lower than in bulk crystals. The reason that the transition temperature is lower for films on LAO has been attributed to this compressive strain fighting against the orthorhombic distortion of the Ru-O octahedra[26, 27]. Nevertheless, Ca_2RuO_4 films on LAO are stable and undergo a first-order insulator-to-metal transition, so they are an ideal playground to study photoinduced insulator-to-metal transitions.

2.2   Superconductivity

Other than insulator-to-metal transitions, the other phase of matter that will be studied in this thesis is superconductivity, specifically in $La_{1.85}Sr_{0.15}CuO_4$ (LSCO). Superconductivity is a phenomenon where the electrons in a metal have a bosonic attractive interaction (whose source is material specific and in many cases unknown), pair up to form Cooper pairs, which then condense into a single macroscopic "condensate" and behave essentially as a perfect conductor[28, 29]. The two physical phenomena that are signatures of, and essentially define superconductivity are zero electrical resistance and the Meissner effect[28]. Zero electrical resistance means that when a voltage is applied to a superconductor, current flows with zero measurable resistance. This means, for example, that if a current is set in a closed loop of a superconductor, it will flow indefinitely, and although it's impossible to measure forever currents flowing for years at a time have been measured [30]. This has the obvious application that it could make the transport of power by electricity much cheaper and work over arbitrarily long distances with minimal losses. This is however not currently possible for two reasons. First, superconductivity generally only occurs at low temperatures. Most simple metals superconduct with critical temperatures below 30K, a temperature that requires liquid helium [28]. Second, if the applied current goes beyond the critical current, the superconducting state is destroyed and the material goes back to behaving like a conventional metal,

13

exhibiting resistive losses[28]. For these reasons, there has been an enormous effort to realize superconductors that have higher critical temperatures and critical currents, and a variety of different methods of to achieve this are currently being investigated.

The second experimental signature of a superconductor is the Meissner effect, where a material expels a magnetic field when it goes through the superconducting transition, thus behaving as a perfect diamagnet. This is in contrast to how a "perfect metal" (a metal where the Drude scattering time is taken to infinity) would behave, where it only perfectly expels a time varying magnetic field [31, 32]. The ability of a superconductor to perfectly expel an applied magnetic field comes from the quantum mechanical nature of the superconducting state, that all of the superconducting electrons behave like a single macroscopic wavefunction[28, 31, 32].

Another experimental signature of the quantum mechanical nature of the superconducting state is the Josephson effect[33]. The Josephson effect concerns the current that can flow between two superconductors that are separated by an insulating layer. This comes from the overlap of the superconducting wavefunction in the first superconducting region with the second one. The superconducting wavefunction essentially makes up the order parameter of the superconducting state, and it has both a magnitude and a phase.

$$\psi = \rho e^{i\phi} \tag{2.10}$$

Here ρ is the magnitude of the order parameter, which is directly proportional to the density of superconducting carriers, and ϕ is the phase order parameter. Behaving as the superconducting wave function it has the corresponding bra and ket vectors which satisfy the following.

$$\langle \psi | \psi^* \psi | \psi \rangle = | \psi |^2 = \rho \tag{2.11}$$

For the Josephson effect, we consider two wavefunctions for the left and right superconducting regions, ψ_L, ψ_R and their corresponding state vectors $|L\rangle, |R\rangle$. The situation is depicted schematically in figure 2.5.
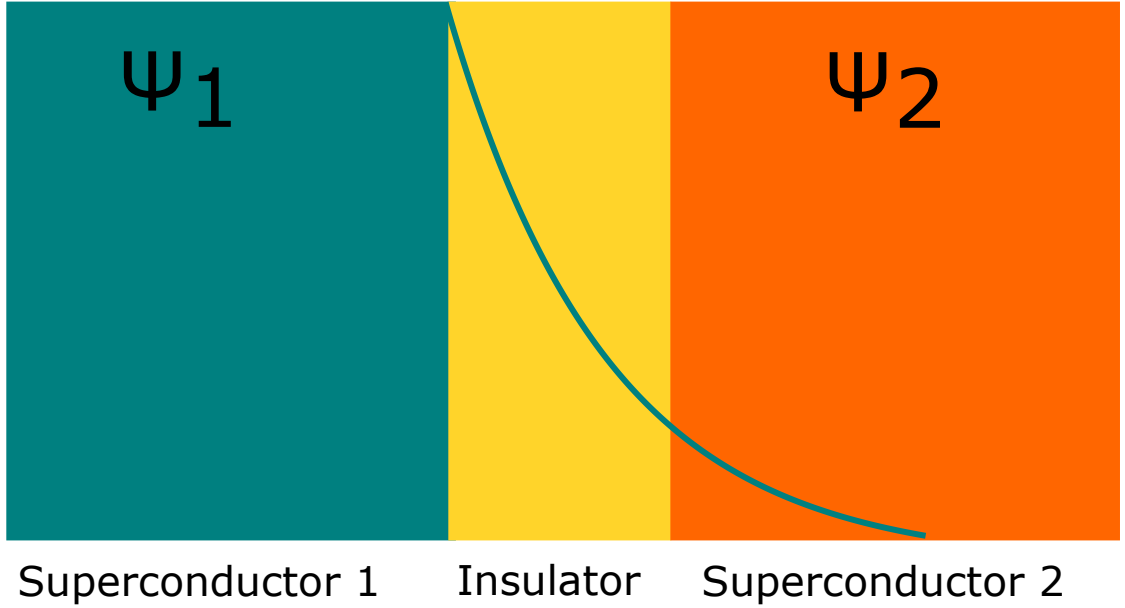
Figure 2.5: Schematic of a Josephson Junction, where ψ_1 and ψ_2 represents the superconducting wavefunction of regions 1 and 2, respectively. The decaying green curve of ψ_1 represents the overlap of the wavefunction through the yellow insulating region into region 2.

The total state vector satisfies the Schrodinger Equation for the full Hamiltonian of the system.

$$|\psi\rangle = \psi_R |R\rangle + \psi_L |L\rangle \tag{2.12}$$

$$i\hbar \frac{\partial |\psi\rangle}{\partial t} = H |\psi\rangle \tag{2.13}$$

$$H = E_R |R\rangle \langle R| + E_L |L\rangle \langle L| + K(|R\rangle \langle L| + |L\rangle \langle R|) \tag{2.14}$$

Here $E_{L/R}$ is the uncoupled energy of a superconducting region, which won't be important for the Josephson effect, and K is a phenomenological coupling parameter that allows for tunneling between the two regions. This form is the simplest term we could write to couple the two regions. We will remain ambiguous about what exactly is contained in it because the Josephson equations derived from this approach holds very generally for systems that span orders of magnitude in size

and complexity, from cuprates (which will be discussed more below), to artificially constructed Josephson junctions, but is generally related to the overlap of the wavefunctions of the two superconducting condensates in the two regions. Using the orthogonality of the state vectors $|L\rangle$ and $|R\rangle$ we can project out two individual equations from the Schrodinger equation.

$$i\hbar\frac{\partial\psi_{L/R}}{\partial t} = E_{L/R}\psi_{L/R} + K\psi_{R/L} \tag{2.15}$$

And for an individual superconducting wavefunction.

$$\frac{\partial\psi}{\partial t} = i\frac{\partial\phi}{\partial t}\rho^{1/2}e^{i\phi} + \frac{\partial\rho}{\partial t}\frac{e^{i\phi}}{2\rho^{1/2}} \tag{2.16}$$

If we put a DC potential difference V across the junction, the two energies E_L, E_R which are really the chemical potential for the two ensembles, will each be shifted by $\pm eV$ (sign depending on whether potential drop is left to right or right to left). This creates an energy difference between the two superconducting regions of $2eV$. We can choose the zero of the energy to be in between these two, so now our Schrodinger equation is the following:

$$i\hbar\frac{\partial\psi_L}{\partial t} = eV\psi_L + K\psi_R \tag{2.17}$$

$$i\hbar\frac{\partial\psi_R}{\partial t} = -eV\psi_R + K\psi_L \tag{2.18}$$

If we then use the total derivative defined above along with the two coupled equations for the two regions we get the following (defining the phase difference between the two regions as θ).

$$\phi = \phi_L - \phi_R \tag{2.19}$$

$$\frac{\partial\rho_L}{\partial t} = \frac{2}{\hbar}K\sqrt{\rho_L\rho_R}sin(\phi) \tag{2.20}$$

$$\frac{\partial\rho_R}{\partial t} = -\frac{2}{\hbar}K\sqrt{\rho_L\rho_R}sin(\phi) \tag{2.21}$$

The first two equations, being time derivatives of a charge density, can be identified as equations for the current in each individual region, which is directly related to

the order parameter phase difference of the two regions with the $\sin \phi$ term. The second term relates the order parameter phase difference between the regions to the applied voltage. The difference in sign between the two current equations is related to the fact that current will flow from one region to another and vice verse, and the individual signs come from the choice of convention for the phase difference, $\phi = \phi_L - \phi_R$ vs $\phi = \phi_R - \phi_L$. For the case of two equivalent superconducting regions, $\rho_L = \rho_R = \rho$, these equations can be written in the following simpler form:

$$I = I_0 sin(\phi) \tag{2.22}$$

$$\frac{\partial \phi}{\partial t} = \frac{2eV}{\hbar} \tag{2.23}$$

where $I_0 = 2\rho K/\hbar$ is the critical current of the Josephson junction, which depends on the coupling between the two superconducting regions. To reiterate, the essential physical picture of the Josephson effect is the following: A tunneling current can flow between two superconducting regions that are separated by an insulating barrier, and that current is related to the order parameter phase difference between the two regions and the spatial overlap of their wavefunctions. As will be discussed below, this picture is successful in explaining some of the interesting properties of superconducting cuprates and their interaction with light.

2.3 High-T_c Cuprates and the Josephson Plasma Mode

The most straightforward definition of cuprates is that they are materials that contain both copper and oxygen (in a square-planar geometry). Intense interest in studying cuprates started with the discovery of high-temperature superconductivity in $La_{2-x}Ba_xCuO_4$(LBCO) [34]. Soon after, many different cuprate compounds were discovered with superconducting critical temperatures, with some having transition temperatures above 100K[35]. What causes these materials to exhibit superconductivity is still not fully understood, as these materials have very
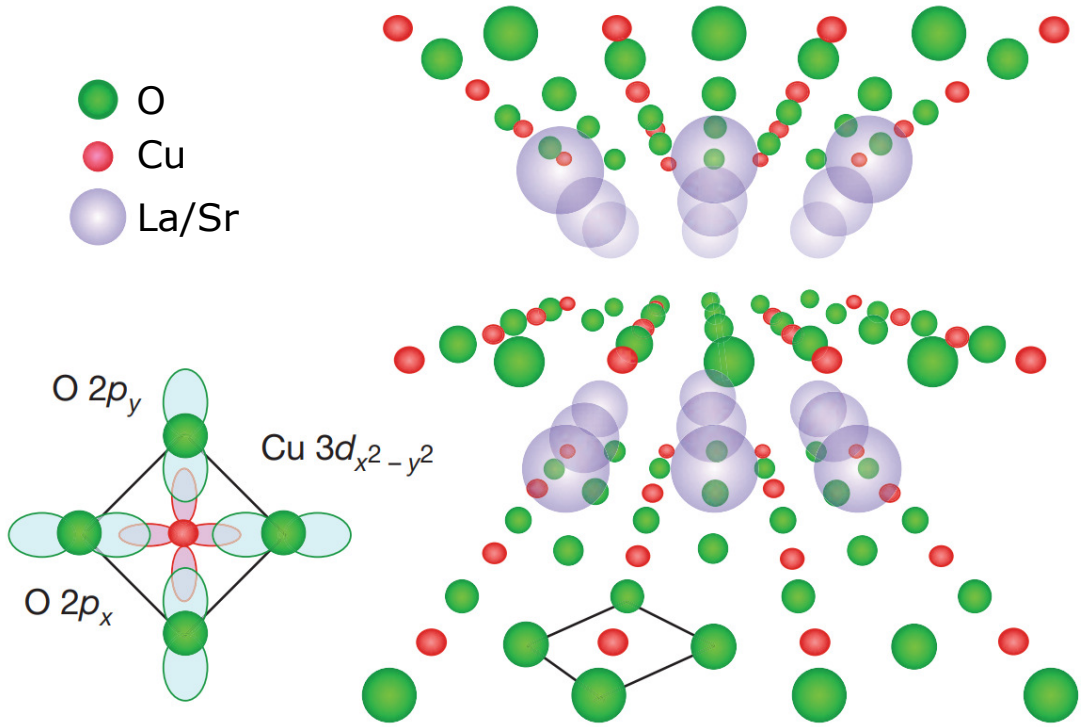
Figure 2.6: From [35] Schematic of crystal structure for a single-layer cuprate superconductor.

complex phase diagrams which include a wide variety of phases in addition to superconductivity, such as charge and spin density waves, strange metal, nematic order, pseudogap, antiferromagnetism, and more[35]. The details of these phases and their interplay, although incredibly important, is not what is studied in this thesis. What is most important here is that cuprates are highly anisotropic, quasi-2d metals. This means that, in the normal state, although the resistivity measured in the ab-plane is conducting, perpendicular to these planes along the c-axis the material is insulating. This paints the general picture of cuprates as weakly coupled copper-oxygen planes, which then become superconducting below a critical temperature. A schematic of the cuprate crystal structure is shown in figure 2.6.

Although cuprates are insulating along the c-axis in the normal state, as just described earlier, there is a mechanism to have transport between superconducting regions separated by insulating regions. Here the superconducting regions are the individual copper-oxygen planes. Below T_C, Cooper-pair tunneling yields a Drude-

like optical response along the c-axis of cuprates, with a plasma frequency termed the Josephson Plasma Mode (JPM) [36]. The derivation of the JPM involves using the same Josephson equations derived above with an oscillating applied electric field. Starting with the Josephson equation for the time evolution of the phase, in terms of electric field we have

$$\frac{\partial \phi}{\partial t} = \frac{2edE}{\hbar} \tag{2.24}$$

which for an AC field gives

$$E = E_0 e^{-i\omega t}, \phi = \phi_0 e^{-i\omega t} \tag{2.25}$$

$$-i\omega\phi_0 = \frac{2ed}{\hbar}E_0 \tag{2.26}$$

We can then use the other Josephson equation, which in the limit of small electric field (and thus small interlayer phase difference) is:

$$J = J_1 \sin \phi_0 \approx J_1 \phi_0 \tag{2.27}$$

where J_1 is the c-axis critical current. Using the relationship in equation 2.27 for ϕ_0 and the relationship between E_0 and ϕ_0 we can obtain a proportionality between the applied electric field and the current, which then gives the conductivity through Ohm's Law.

$$J = -\frac{2edJ_1}{i\omega\hbar}E_0 \tag{2.28}$$

The conductivity here then has the same form as the Drude optical conductivity, but with no scattering.
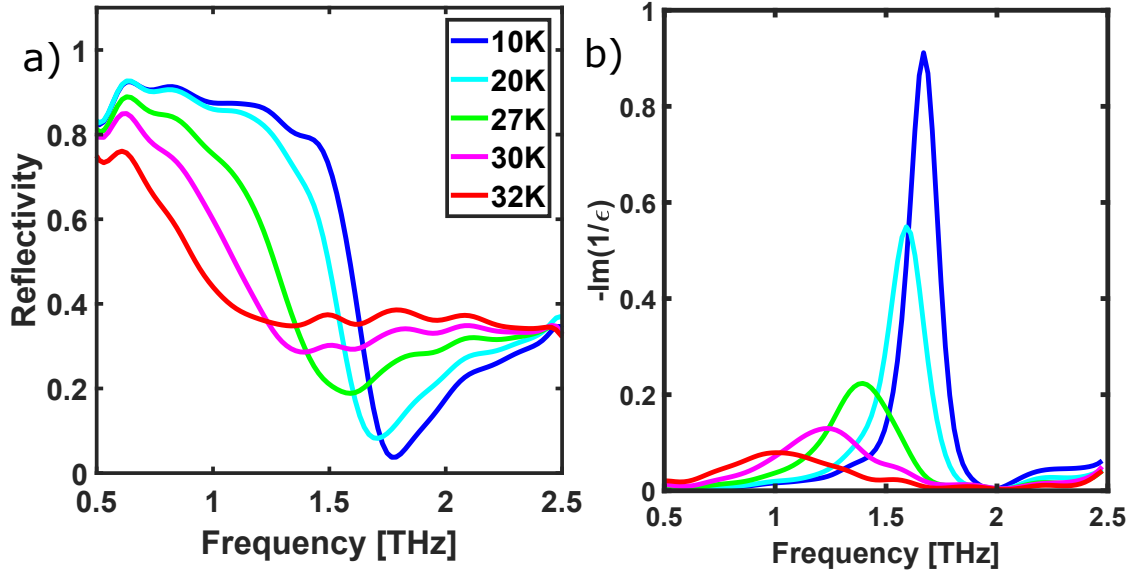
Figure 2.7: a) THz reflectivity of LSCO in the superconducting state. b) Loss function of LSCO in the superconducting state.

$$\sigma = -\frac{i\omega_J^2}{\omega} \tag{2.29}$$

$$\omega_J^2 = 2edJ_1/\hbar \tag{2.30}$$

where ω_J is the JPM frequency. A key here is that J_1 scales directly with the superfluid density. The physics is that the optical response of the superconducting condensate along the c-axis of cuprates is a Drude response with a plasma frequency that scales directly with the superconducting cooper pair density. This longitudinal plasma mode is known as the Josephson plasma mode, and manifests as an edge in reflectivity. The JPM and the associated edge in reflectivity is thus a direct reporter of superconductivity in cuprates. Reflectivity on the LSCO crystal studied in this thesis is shown in figure 2.7, where the edge in reflectivity shows a clear redshift with increasing temperature as the cooper pair density decreases as the sample gets closer to T_C. For the specific case of cuprates, the JPM lies in the THz range[37]. This is a consequence of both the c-axis lattice spacing and the cooper pair density in cuprates, and is not tied to this energy range for any other fundamental reason. For example, in contrast artificially made arrays of Josephson junctions have JPM frequencies at much lower frequencies, in the microwave range [38].

In addition to the linear optical response, the Josephson equations also give insight into the nonlinear optical response of the JPM. The first nonlinear optical effect from the JPM is high-harmonic generation, which can be seen from the current Josephson equation.

$$J = J_1 sin(\phi) = J_1 sin(\phi_0 cos(\omega_{pump}t))$$
$$\approx J_1(\phi_0 cos(\omega_{pump}t) - \frac{\phi_0^3}{6}cos^3(\omega_p t) + ...) \quad (2.31)$$

$$\phi_0 = \frac{2edE}{\hbar\omega_{pump}} \quad (2.32)$$

When the Josephson phase ϕ is driven harmonically at frequency ω, because of the sinusoidal relationship between current and phase, this will create higher order currents oscillating at odd harmonics of ω. An important note is that the Josephson equations predict that the high-harmonic should scale with the JPM frequency, so it should increase monotonically as temperature decreases. The lowest order nonzero high harmonic generation, third harmonic generation, is studied experimentally in chapter 4 of this thesis, and it is found to actually have non-monotonic temperature dependence. The details of this will be discussed in chapter 4.

The other nonlinear optical effect of the JPM is a redshift of the JPM frequency with applied electric field. This can be seen by looking at the voltage equation for an applied electric field between two copper oxygen layers in a cuprate superconductor.

$$V = \frac{q}{C} + V_{app} \cos \omega t \quad (2.33)$$

where q is the charge on the junction, C is the junction's capacitance, V_{app} is the applied voltage, and ω is the frequency of the drive. This can be combined with

the two Josephson equations (shown again below) by using the relationship $I = \frac{dq}{dt}$, taking a time derivative, and using the relationship in equation 2.35 for $\frac{d\phi}{dt}$.

$$I_p = I_c \sin \phi \tag{2.34}$$

$$\frac{d\phi}{dt} = \frac{2eV}{\hbar} \tag{2.35}$$

$$\frac{dq}{dt} = -I_c \sin \phi \tag{2.36}$$

$$\frac{d^2q}{dt^2} = -I_c \frac{d\phi}{dt} \cos \phi = -I_c \frac{2eV}{\hbar} \cos \phi \tag{2.37}$$

Then using our equation for the voltage drop between the two layers we get the following.

$$\frac{d^2q}{dt^2} = -I_c \frac{2e}{\hbar} (\frac{q}{C} + V_{RF} \cos \omega t) \cos \phi \tag{2.38}$$

This can be arranged to have the form of a harmonic oscillator, whose resonant frequency has a parametric dependence on the Josephson phase ϕ.

$$\frac{d^2q}{dt^2} + \omega_J^2 \cos \phi q = -\omega_J^2 C V_{RF} \cos \omega t \cos \phi \tag{2.39}$$

$$\omega_J^2(\phi) = \omega_J^2 \cos \phi \tag{2.40}$$

For an AC field drive, the JPM frequency can be expanded in powers of the field strength.

$$\omega_{jp}^2 = \frac{1}{L(\phi)C} = \omega_{jp0} cos(\phi) \approx \omega_{jp0}^2 (1 - \frac{\phi_0^2}{4} - \frac{\phi_0^2 cos(2\omega_{pump}t)}{4}) \tag{2.41}$$

This final equation shows that as larger electric fields are applied, the JPM frequency redshifts. Experimental measurements of this in LSCO will be presented in chapter 4. It should also be noted that the above relation between JPM frequency and applied field allows for parametric driving of the JPM. This was demonstrated experimentally in a cuprate similar to the LSCO studied in this thesis, LBCO [39]. There it was demonstrated through THz-pump THz-probe spectroscopy that Josephson plasma waves could be parametrically amplified by control of the pump frequency.

Chapter 3

Experimental Techniques

In this chapter a variety of techniques that were used to study quantum materials and metamaterials during the course of this thesis will be introduced. All of the experiments in this thesis involve THz light in some capacity, for a few reasons. Many of the excitations and energy scales of quantum materials lie in the THz and midinfrared regime, such as superconducting gaps, phonons, magnons, etc[4]. Additionally, THz is at a low-enough energy to be close to a measurement of DC conductivity, and for some materials the Drude parameters can be extracted from measuring in the THz regime[13]. THz is still however on ultrafast timescales (1 THz $\rightarrow$ 1 ps) and is therefore it is a good probe of the metallicity while also being compatible with pump-probe experiments on ultrafast timescales. We will first introduce the concept of THz Time Domain Spectroscopy (THz-TDS), including different ways to generate and detect THz, and how to extract material parameters from THz measurements. We will then introduce a pump-beam into the experiment and review Optical-Pump, THz Probe spectroscopy. Finally, we will briefly discuss using midinfrared pump (still low-energy and close to THz compared to optical frequencies), optical probe spectroscopy to drive (and probe) low-energy excitations in materials with strong fields.

3.1 Terahertz Time Domain Spectroscopy

We first introduce Terahertz Time Domain Spectroscopy (THz-TDS) and how the THz pulses are generated, detected, and used to extract material parameters. THz-TDS is essentially used as the experimental probe in all three of the main projects of this thesis, particularly as a probe of THz nonlinearities, light-matter coupling, and a photoinduced insulator-to-metal transition.

3.1.1 THz Generation

First we will review a few methods of THz generation that wereused for the work of this thesis. The details for measuring the generated THz pulses will be explained in the next section. The first method of generating THz is optical rectification in nonlinear crystals. Optical rectification is one of the frequency mixing processes of light in a nonlinear crystal. The optical response of a crystal can be written in terms of its linear and nonlinear susceptibilities, which can be written as a series in powers of the incident electric field[40].

$$P = \chi^1 E + \chi^2 E^2 + \chi^3 E^3 + ... \qquad (3.1)$$

where P is the induced dipole moment, E is the electric field, and χ^i is the "ith"-order susceptibility, where χ^1 is the linear susceptibility, and $\chi^{>1}$ are the nonlinear susceptibilities. Optical rectification (and also difference frequency generation, which will be discussed later), are processes related to χ^2, the second order susceptibility, so we will discuss this further. The second order (and any even order susceptibilities) must vanish for crystals that preserve inversion symmetry. Inversion symmetry involves flipping the sign of the spatial coordinate $r \rightarrow -r$, which in turn acts on the electric field as $E \rightarrow -E$. A crystal that does preserve inversion symmetry then has it's induced dipole moment flipped $P \rightarrow -P$. However, the χ^2 term in the equation for induced dipole moment transforms as $\chi^2 E^2 \rightarrow \chi^2 E^2 \neq -\chi^2 E^2$ unless $\chi^2 = 0$, since there's an even number of powers of the electric field for that term of the dipole moment. Thus crystals that preserve inversion symmetry must have vanishing even order nonlinear susceptibilities.

For crystals that do break inversion symmetry, which includes all crystals used for THz generation through optical rectification, we can look at the effect of mixing electric fields of two different frequencies, ω_1 and ω_2.

$$E = E_0 \cos(\omega_1 t) + E_0 \cos(\omega_2 t) \tag{3.2}$$

$$P^2 = \chi^2 E_0^2 (\cos^2(\omega_1 t) + \cos^2(\omega_2 t) + 2\cos(\omega_1 t)\cos(\omega_2 t)) \tag{3.3}$$

The 2nd-order trigonometric functions can be shown to contain terms such as $\sin((\omega_1 + \omega_2)t)$ and $\sin((\omega_1 - \omega_2)t)$, which correspond to sum and difference frequency generation. Additionally, the first two terms can both be written as $(1/2)(1 + \cos(2\omega_I t)$, showing that each term has a second harmonic term oscillating at $2\omega_i$ and a constant term, which is termed rectification. To reiterate, optical rectification is the constant, DC polarization induced in a nonlinear crystal by an electric field interacting with itself. For generation of THz pulses, optical rectification comes from different frequency components in the same optical pulse mixing with each other in the nonlinear crystal. This means that for a spectrum containing frequencies of light between ω_1 and ω_2, the highest possible frequency generated from optical rectification, is $\omega_2 - \omega_1$, and the lowest frequency generated is (in principle) a DC component. A gaussian pulse that is sent into a nonlinear crystal also has a gaussian spectrum, and since χ^2 gives a 2nd-order polarizability proportional to E^2, the output from optical rectification will also be a gaussian pulse, whose bandwidth is determined (in part) by the bandwidth of the incoming pulse.

One crystal that is commonly used for THz generation is ZnTe, a semiconductor with zincblende structure that breaks inversion symmetry[41]. An example of a THz pulse generated through optical rectification of an ultrafast, 800nm pulse from two similar lasers is shown in figure 3.1. The difference between the generation pulses of these two systems is that one is slightly more narrowband, with a 30nm bandwidth and 100fs pulse width in time, while the other is more broadband, with a 60nm bandwidth and 35fs pulse width in time. What can be highlighted here is that when the generation pulse has a larger bandwidth, more high-frequency components are generated. Another property that makes ZnTe good for gener-
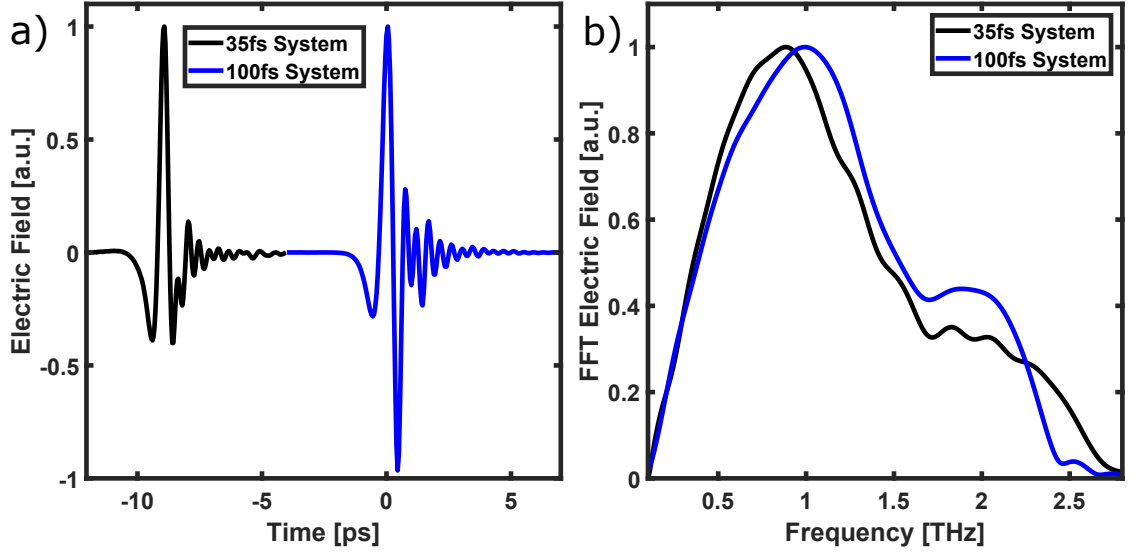
Figure 3.1: a) Time Domain Scans and b) Frequency Domain Spectra of THz pulses generated with ZnTe through optical rectification for two different laser systems with different pulse generation bandwidths

ating THz is that the group velocity of the 800nm generation beam matches the phase velocity for the generated THz pulse. This means that as the 800nm pulse propagates through the ZnTe generating additional THz radiation that is in phase with the previously generated THz pulse. A mismatch between these two velocities would cause destructive interference reducing the THz generation efficiency. The length at which the generation and THz pulses need to propagate for the difference in phase of THz generation to become out of phase by π is know as the coherence length L_c of the crystal.

Optical rectification can also be used to generate high-field THz pulses to study nonlinear THz phenomena. There is not a strict definition for high-field THz, it is essentially THz pulses with a field strength (the electric field at the peak of the pulse) that is strong enough to drive nonlinearities in a sample. Realistically, high-field THz pulses generally means at least 10kV/cm, whereas the maximum acheived in tabletop THz sources is on the order of 1MV/cm [42, 43].There are crystals, such as organics BNA and OH1, where this is a straightforward process similar to generation in ZnTe where an optical pulse can passes through a thick crystal generating high-field THz pulses[44, 45, 46]. Although many of these crys-

tals generate high-field THz very efficiently, they also have low damage thresholds. The nonlinear THz pulses used in this thesis were instead generated using optical rectification in crystals of LiNbO$_3$, using the tilted pulse front technique[47]. In short, the tilted pulse front technique is a way to greatly increase the THz generation efficiency in a crystal where the optical generation pulse group velocity differs from the generated THz pulse phase velocity.

The idea of the tilted pulse front technique is to use the fact that generated THz radiation propagates perpendicular to the pulse front of the generation beam, and since the group velocity of the generation beam is faster than the phase velocity of the THz beam $n_{THz}^{phase} > n_{gen}^{group}$, where n refers to the index of refraction for generation (gen) or THz pulses for either group or phase velocities. A tilted pulse front will cause the generation beam to propagate at a slower speed along the direction of THz generation, which is perpendicular to the pulse front. For a generation beam with a pulse front tilted at angle θ, the component perpendicular to the pulse front will propagate at a velocity that is the projection of the velocity along that direction, $v_{gen}^{group}cos(\phi)$. This is shown schematically in figure 3.2. The phase matching condition for a tilted pulse front is then the following:

$$v_{gen}^{group}cos(\phi) = v_{THz}^{phase} \tag{3.4}$$

For LiNbO$_3$ the 800nm group index of refraction is $n_{gen}^{group} = 2.25$ and the THz phase index of refraction is $n_{gen}^{group} = 4.96$, leading to a phase matched tilted pulse front of $\phi = \cos^{-1}(2.25/4.96) = 63^0$[47]. Due to refraction of the generation pulse as it enters into the crystal, the in-air pulse front should be tilted to an angle of $\phi = \tan^{-1}(2.25\tan(\phi) = 77.2^0$. The tilted pulse front can be generated by using the 1st-order diffracted beam from a grating, which satisfies the following equation.

$$\sin\gamma_i - \sin\gamma_r = \lambda_{gen}p \tag{3.5}$$

Here $\gamma_{i,r}$ are the angles of the beam incident on and diffracted from the grating, λ_{gen} is the THz generation beam wavelength, and p is the grating periodicity, in this case we use a density of 2000 grooves/mm. Having a pulse front tilted at an
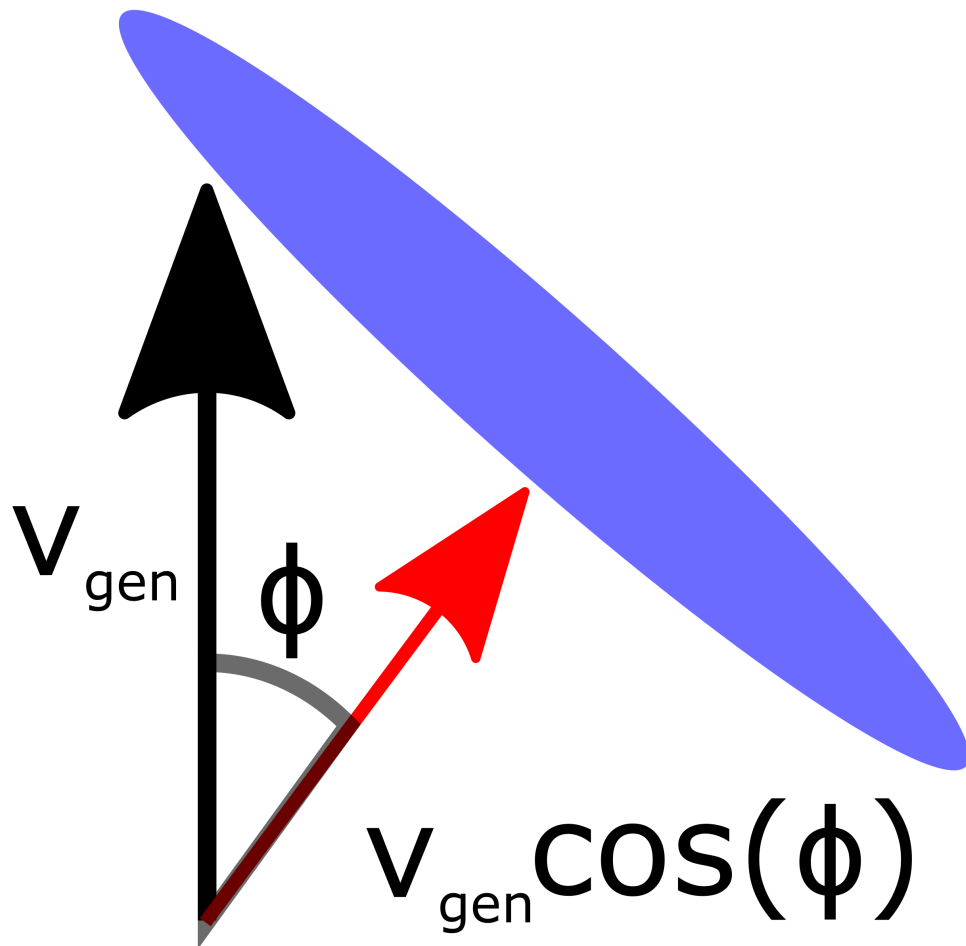
Figure 3.2: Schematic of angles for tilted pulse front scheme between generation beam propagation v_{gen}, the pulse-front (blue ellipse), and the projection perpendicular to the pulse front, $v_{gen} \cos \phi$.

angle ϕ' gives the following constraint.

$$\frac{\sin\gamma_i + \sin\gamma_r}{\cos\gamma_r} = \tan\phi' \tag{3.6}$$

For the experimental setup here, with 800nm generation light and 2000 grooves/mm this is satisfied by an incident angle of 60^0 and a diffracted angle of 47^0. A picture of the experimental setup is shown in figure 3.3. After diffracting off the grating the beam has it's polarization rotated by a half waveplate and is imaged onto the LiNbO$_3$ by an 80mm focal length lens. After THz generation, the pulse is collimated by another lens, and then directed to 4-inch parabolic mirror to focus it onto the sample spot. An example THz transient generated by this setup is shown in figure 3.6c.

The other method of generating THz pulses in this thesis is through the use of photoconductive antennas, which does not make use of any optical rectification in any nonlinear crystals. Instead, THz can be generated from metallic antennas fabricated on a semiconductor. When a 1.55eV generation pulse is incident on a semiconductor, such as GaAs, it will generate free carriers in the conduction band. When the excited spot is between two metallic antennas with a voltage between them, the carriers will be accelerated, giving a current. Specifically the process of the generation beam creating carriers while there is a voltage between the antennas will create a quickly changing current, which will then radiate a power given by Larmor's formula [48].

$$P = \left(\frac{dI}{dt}\right)^2 \frac{2q^2}{3c^3} \tag{3.7}$$

In this equation, c is the speed of light, dI/dt is the time derivative of the current, and q is the total charge being accelerated. The temporal waveform and bandwidth of the THz pulse can be tuned by choice of semiconductor, antenna design, pump fluence, and antenna bias voltage [40]. An example THz waveform and spectrum for the THz pulse generated by a photoconductive antenna is shown in figure 3.4.
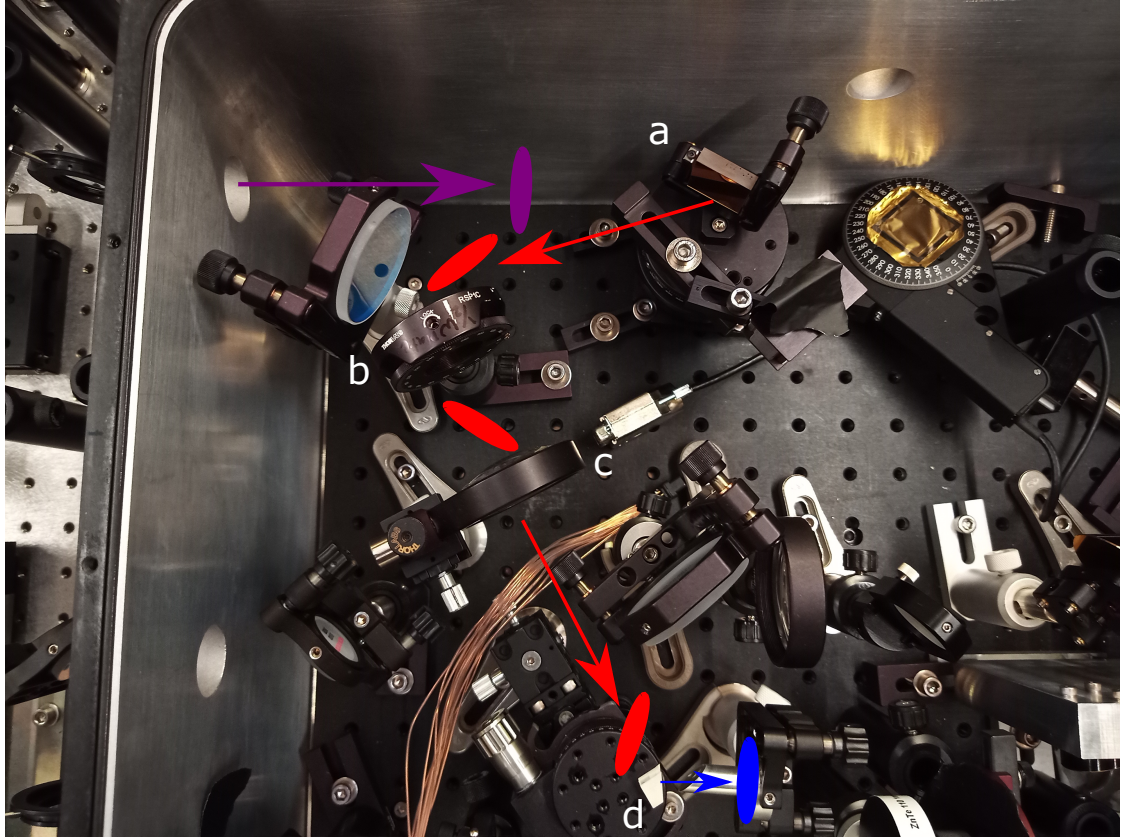
Figure 3.3: Picture of tilted pulse front setup used to generate high-field THz pulses. The beams are indicated by arrows in the direction of propagation and an ellipse to indicate their pulse front, where the size is not to scale, more to indicate the tilt of pulse-front at various stages of the beam path. The incoming 800nm beam without a tilted pulse front is indicated in purple, with a pulse front perpendicular to propagation. After diffracting off of the grating, the tilted pulse front beam is indicated in red with an ellipse at an angle to propagation. The THz generation is indicated by a blue arrow, with the pulse front perpendicular to the propagation direction. Key optical elements are labelled: a-diffraction grating, b-half waveplate, c-lens to image beam onto $LiNbO_3$, d-$LiNbO_3$ crystal
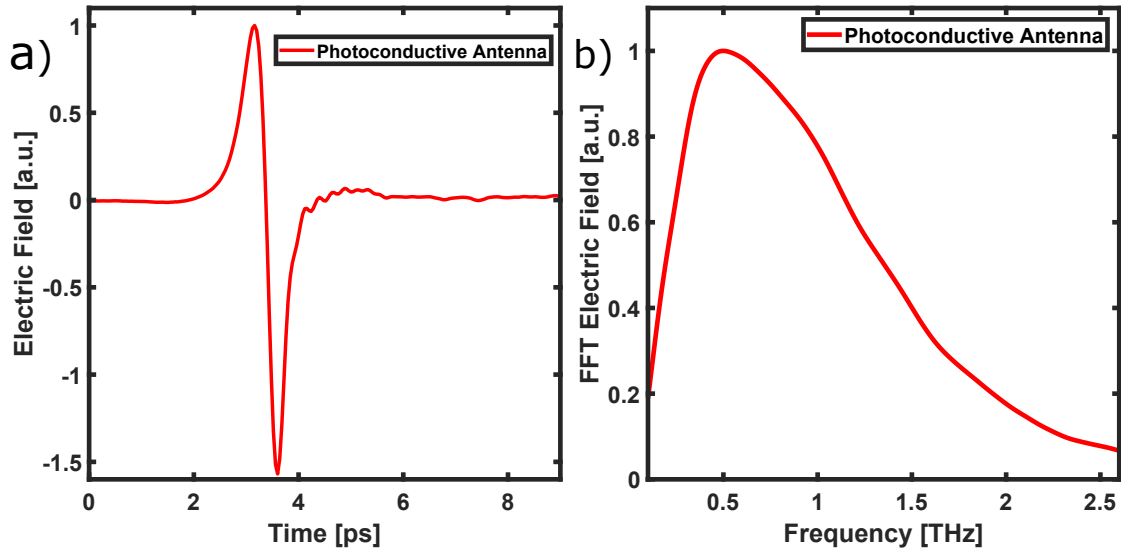
Figure 3.4: a) Time domain pulse and b) Frequency domain spectrum for THz generated by photoconductive antenna.

3.1.2 Time-Domain Spectroscopy

Since THz is a relatively low frequency of light, it is possible to directly measure THz pulses in the time domain. An obvious reason this is helpful is that it is then easy to integrate into pump-probe geometries. Of even greater importance is that the THz waveform can be directly measured in time yelding both the amplitude and phase of the terahertz electric field. This makes it possible to extract both the real and imaginary parts of the optical parameters of a material directly from THz transmission or reflection, without the need of Kramers-Kronig relations.

The general principle behind THz-TDS is to use a shorter "gate" pulse to measure instants of the THz electric field of the pulse at different delays, and then sweeping the gate delay through the THz field. In order to make use of this fast pulse, a measurement scheme that can sample small windows in time of the electric field of a THz pulse is necessary. The measurement of a THz pulse is very similar to that of a pump-probe measurement, where the gate and THz pulse need to be brought together to the same spot and their delay varied between being overlapped and arriving before and after each other. However, it is key that the detection of the THz does not have long-lived dynamics due to the THz probe, and instead

32

acts as a cross-correlation of the gate-pulse and the instantaneous electric field of the THz pulse. If the detection scheme had longer-lived dynamics this would cause smearing and distortion of the measured time trace. The two ways in which THz pulses are measured for experiments in this thesis are with Electro-Optic Sampling (EOS) and with a photoconductive antenna.

Electro-Optic Sampling (EOS) is the use of a nonlinear crystal and specifically a 2nd-order susceptibility effect to measure the THz pulse[49]. In properly chosen crystals, such as ZnTe, GaP, and GaSe, birefringence can be induced from an applied electric field. This is known as the pockels effect[49, 40]. Thus for EOS, this birefringence is caused by the THz probe field in the EOS crystal. Then, as the gate pulse propagates through the EOS crystal that has birefringence from the THz pulse, it will have its polarization rotated. This polarization can then be detected by passing through the gate pulse through a quater waveplate, and then a Wollaston prism, separating the two components of polarization, and measuring both components on two photodiodes. The use of the quarter waveplate and Wollaston prism enables balanced detection, which is shown schematically in figure 3.5[49]. Specifically, without any THz pulse, the quarter waveplate can be aligned to the gate pulse's polarization so that the output is circularly polarized light. This has equal components of horizontally and vertically polarized light, so passing through the Wollaston prism splits the pulse into two equally intense components, which then each go to a photodiode. What can then be measured is the difference in signal between these two photodiodes, which without any THz pulse present will be zero. Then, in the presence of a THz pulse, the gate pulse will be rotated from the birefringence in the EOS crystal, and then going through the quarter waveplate the pulse will have additional ellipticity compared to without the THz field. This will then lead to one polarization component having more intensity than the other, giving a net difference in intensity on the photodiodes. The difference in signal between the two photodiodes is given by the following formula, when the fractional difference in intensity on the two photodiodes satisfies $\Delta I / I << 1$[50].

$$\frac{\Delta I}{I} = \frac{E_{THz} 2\pi L n_0^3 r_{kl} t_0}{\lambda_0} \tag{3.8}$$

33

where $\Delta I/I$ is the fractional diffrence in intensity on the two photodiodes, E_{THz} is the THz electric field, L is the thickness of the EOS crystal, n_0 is the index of refraction of the EOS crystal at the gate wavelength, r_{kl} is the electro-optic coefficient of the EOS crystal, t_0 is the transmission coefficient at the gate wavelength, and λ_0 is the gate wavelength. A key to EOS is that the birefringence induced in the EOS crystal is linearly proportional to the THz electric field, including its sign, not just the magnitude. This means that when the THz field changes from positive to negative, the polarization rotation of the gate pulse is in the opposite directions, in turn making the signal on the opposite photodiode larger than when the THz field is in the positive direction.

Other than having a nonzero Pockels effect, there are a few considerations to take into account when picking the best EOS crystal for a given experiment. First, too large of an electro-optic response can cause artifacts in the THz measurement, due to over-rotation of the probe beam. This is because if the gate beam's polarization rotates more than 45 degrees, the ellipticity of the beam after the quarter waveplate will actually go down, since it's polarization is now closer to being at the equilibrium angle to the fast-axis of the quarter waveplate. This would then lead to a smaller $\Delta I/I$ for larger fields, and an inaccurate measurement of the THz field. For this reason, for high enough fields, one needs to be careful not to use a crystal that is too thick or with too strong of an electro-optic coefficient.

Another key property for a good EOS crystal is small group velocity mismatch between the THz and gate beam. This will mean that upon entering the EOS crystal the gate and the THz will propagate through the whole crystal together. This first increases the signal, since the gate's polarization will be rotated during it's whole trip through the crystal. Also, this keeps the gate from sampling other points in the THz pulse than the intended one. The final important factor for an EOS crystal is the dispersion of the various optical coefficients of that crystal in the THz range, specifically the index of refraction and absorption, which will effect the group velocity mismatch, the transmission of the THz into the EOS crystal, and how the THz pulse is attenuated in the crystal. For example, the dip in the spectrum measured with ZnTe as an EOS crystal in figure 3.6 is due to a phonon
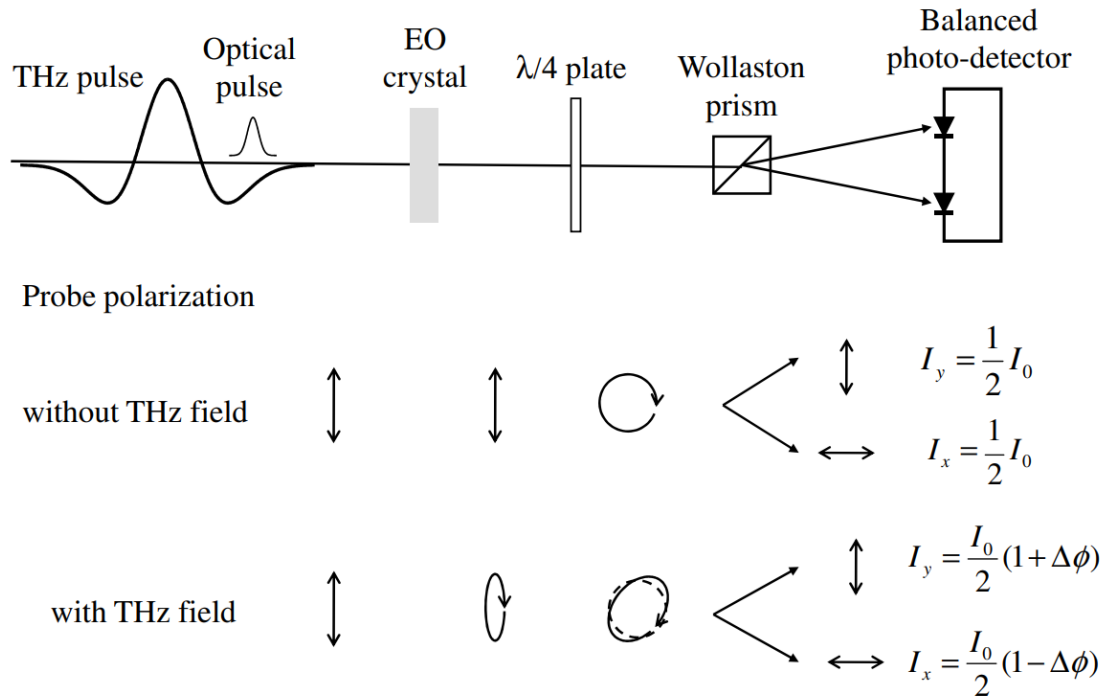
Figure 3.5: From [49]. Schematic of Electro-Optic-Sampling for detection of THz. When the gate pulse propagates without the THz pulse the quarter waveplate makes it circularly polarized, then both polarization components are split by a Wollaston to balanced detection by two photodiodes. When the THz pulse is present in the EOS crystal the field induced birefringence causes a rotation of the gate pulse, which adds some ellipticity to the gate pulse after it passes through the quarter waveplate, giving different amounts of vertical and horizontal polarization that will lead to an imbalance in the signal detected by the photodiodes and a net THz signal.

in ZnTe at that frequency. There is additionally a phonon at $\sim 2.5THz$ that is the main limiting factor in pushing the bandwidth of measured THz to higher frequencies. An even more dramatic realization of this can be seen with extremely broadband THz, for example plasma-based THz generation. There, although the generated THz has a very high bandwidth (i.e. 1-20THz), there is not actually any individual EOS crystal that can sample the whole spectrum. These TDS measurements must be done twice with two separate EOS crystal, for example GaP for the 1-7THz range and GaSe for the 8-20THz range [51].

The other way to measure THz pulses is with a photoconductive antenna[40]. The process is somewhat the reverse of THz generation in a photoconductive antenna, except also utilizing a gate beam whose delay is varied with respect to the THz beam. An antenna on a semiconductor won't measure any current when the THz pulse impinges on it unless carriers have been excited in it. So for detecting THz, the gate pulse, again at optical frequencies, excites carriers between the two ends of the photoconductive antenna. In the absence of the THz pulse, there will be no current between the antenna since there is no voltage. However when the THz pulse hits the antenna, while there are photoexcited carriers in the substrate, the THz E-field will accelerate the carriers, creating a measurable current that will be proportional to the applied field and can be measured. A key to this, similar to EOS, is that the photoconductive antenna measures both the magnitude and sign of the current. As with EOS, this enables measurement of both the amplitude and phase of the terahertz pulse.

With the aforementioned THz generation and measurement techniques we can measure time-traces of the THz pulses, and Fourier transform them to do spectroscopy. Example time traces for three different THz experiments and their fourier transformed spectra are shown in figure 3.6. Figure 3.6a shows a THz pulse that is both generated and detected by a photoconductive antenna. PC antenna generate very low THz fields but are also very sensitive to THz fields, yielding a high signal-to-noise ratio. The working bandwidth is $\sim$0.2-2.5 THz, based on the 10% lines (i.e., where the spectral amplitude is 10% of the peak value). Next, in figure 3.6b is a THz spectrum that is generated with ZnTe with optical rectification and

36
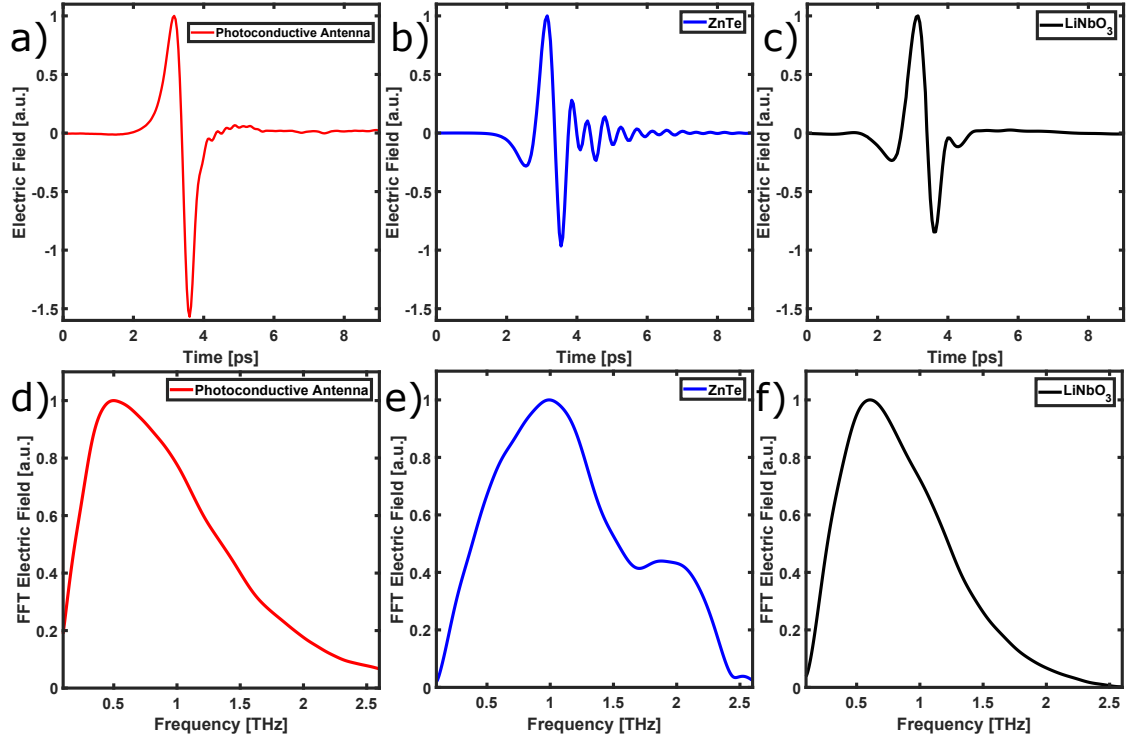
Figure 3.6: Time domain scans and associated spectra of THz generated from a,d) Photoconductive Antenna, b,e) ZnTe, c,f) LiNbO$_3$.

also measured with a different cut of a ZnTe crystal with EOS. Here the working bandwidth is also about 0.2-2.4 THz. Finally, figure 3.6c shows the time trace and spectrum of THz generated by LiNbO$_3$ using the tilted pulse front technique. Here the THz maximum field strength is ~80kV/cm, which is sufficient for nonlinear THz spectroscopy (the subject of chapter 4 of this thesis) or as a THz pump. Compared to the photoconductive antenna and ZnTe THz sources the bandwidth is smaller, about 0.2-1.8 THz based on the 10% lines. Here the THz is measured using EOS with a GAP crystal, which has a smaller electro-optic coefficient than ZnTe, to prevent overrotation of the gate beam in EOS.

Details of optical parameter extraction will be reviewed in the next section, but here we can review some spectroscopic features manifest in THz-TDS spectroscopy. Figure 3.7 shows a reference THz pulse transmitted through air, along with a pulse transmittedthrough a metamaterial designed to have resonances at THz frequencies. In the spectra, these resonances show up as dips in the transmis-

sion at the resonance frequencies. How this manifests in the time domain is that the transmitted THz field oscillates at the resonance frequency, with a number of cycles related to the linewidth of the resonance, as seen in figure 3.7a. Even though less light is transmitted at the resonance frequency (there is a dip in transmission), there is an oscillation at the resonance frequency is because in the reference pulse the different Fourier components add up with phase relationships to have a nearly single cycle pulse, so when a frequency is taken out, the rest of the Fourier components that were canceled at that frequency no longer are, causing an oscillation in the time domain at that frequency. How this manifests in the transmission in terms of frequency is shown in figure 3.7b, where there are dips in the transmission at the metamaterial resonances.

3.1.3   Material Parameters using THz-TDS

As mentioned earlier, one of the great benefits of THz-TDS is that both the magnitude and phase information of the transmitted THz pulse is measured, which allows for direct extraction of optical parameters over the frequency range contained in the THz pulse. Here I will go through the example of extracting the optical conductivity of a thin film on a thick substrate, but it should be made clear that with the phase information of THz-TDS and Fresnel equations in transmission and reflection, optical parameter extraction can be done for any number of linear optical experiments. The situation of a thin-film on a thick substrate is shown schematically in figure 3.8.

The total pulse transmitted through the sample will be attenuated by the transmission coefficients at the air-sample interface, sample substrate interface, and substrate-air interface. The Fresnel coefficient for transmission between two media with indices of refraction n_1 and n_2 is given by the following, where we restrict ourselves to normal incidence transmission in this section.

$$T_{12} = \frac{2n_1}{n_1 + n_2} \tag{3.9}$$

$$T_{21} = \frac{2n_2}{n_1 + n_2} \tag{3.10}$$
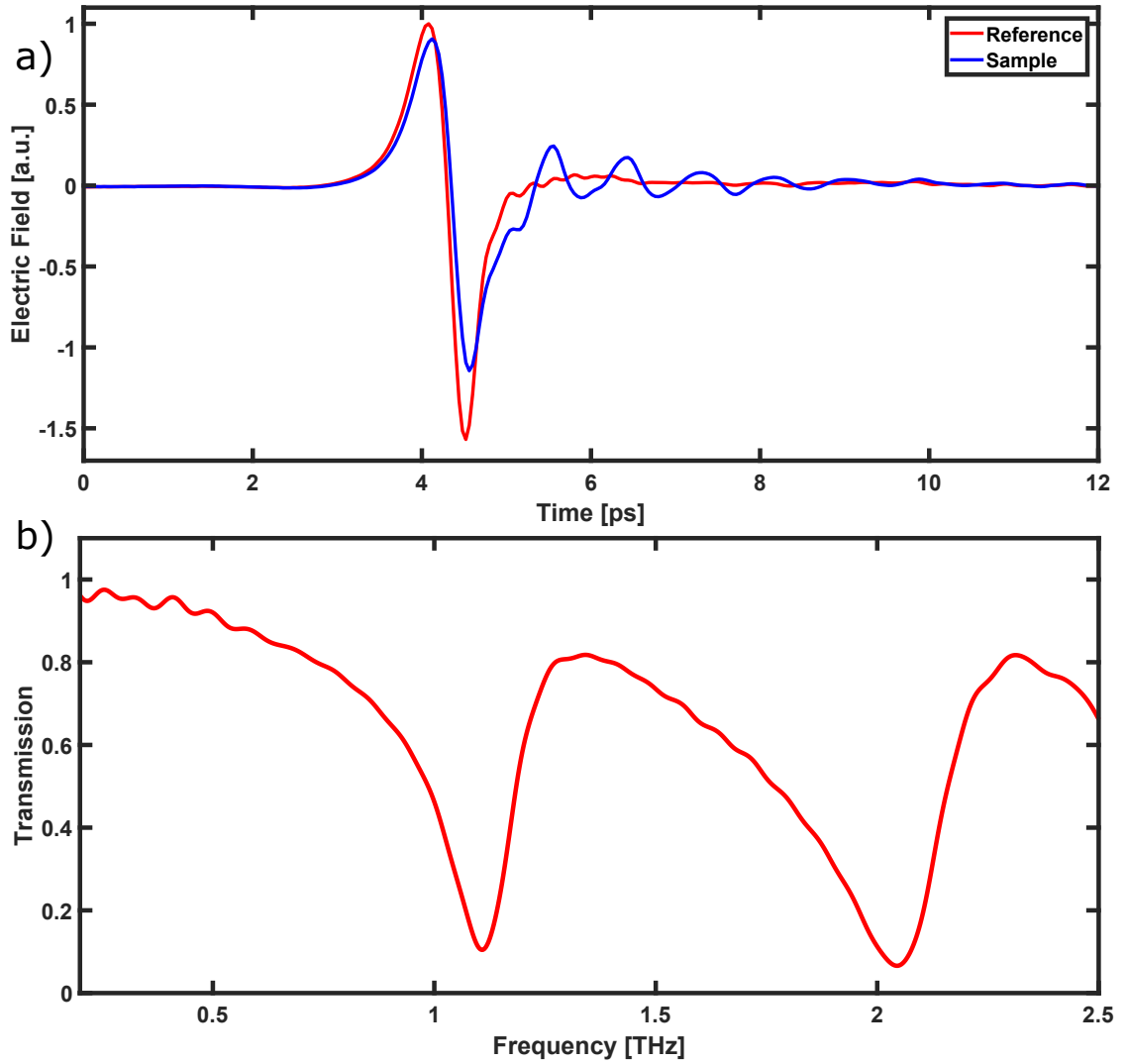
Figure 3.7: a) Time Domain Scans of THz transmission through a Metamaterial (blue) along with a reference pulse measured through air (red). The metamaterial resonances cause clear oscillations of the transmitted field in the time domain. b) Transmission spectrum calculated from the above pulses.
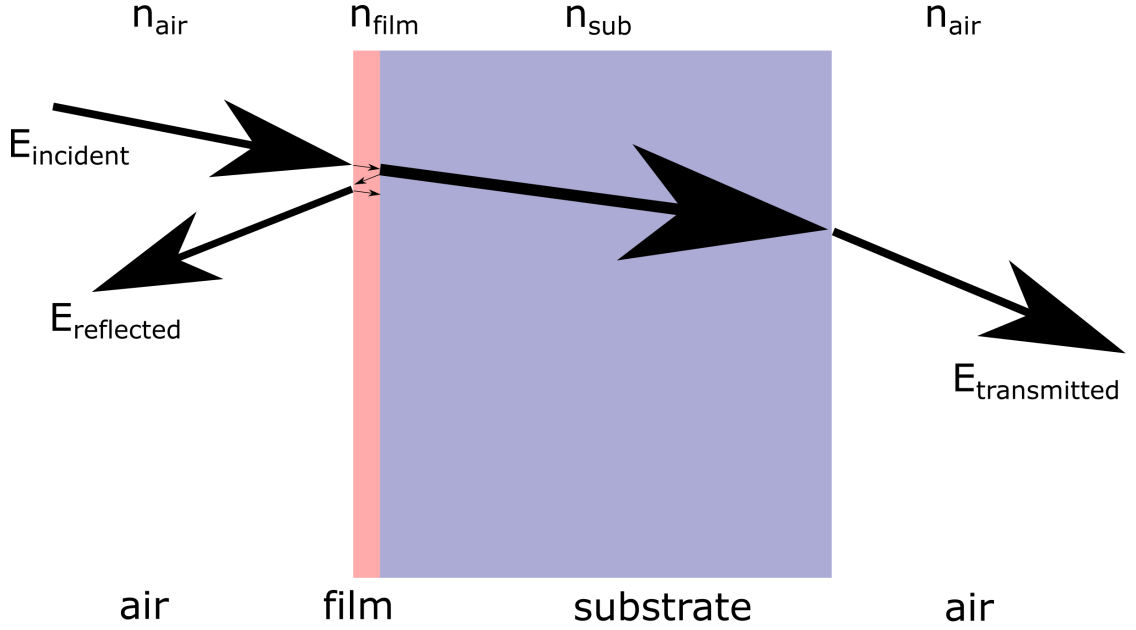
Figure 3.8: Schematic of THz transmission through a thin film on a thick substrate. The incident, reflected, and transmitted Electric fields are indicated by large arrows. Fabry-perot reflections inside the thin film are also indicated by smaller arrows.

Additionally, there is a phase delay picked up by the pulse as it passes through a medium. This is true even when propagating through air, however for THz pulses we generally compare the THz pulse transmitted through a sample compared to a reference. The phase delay, as a function of frequency ω, propagating through a material of index n_2 compared to a material of index n_1 is given by the following.

$$P_{21} = e^{\frac{i\omega d}{c}(n_2 - n_1)} \tag{3.11}$$

Where d is the thickness of the film and c is the speed of light. The final piece that needs to be taken into account is the Fabry-Perot reflections of the THz inside of the sample. This comes from internal reflections of the pulse inside of the sample that eventually transmit and add to the overall measured transmission. For thin media, such as thin films, these will have very small separation from the pulse, so these contribute to the overall transmission and need to be taken into account. For thick samples, the separation in time is large enough that the higher Fabry-Perot terms can be referenced out using temporal windowing. An example of this is
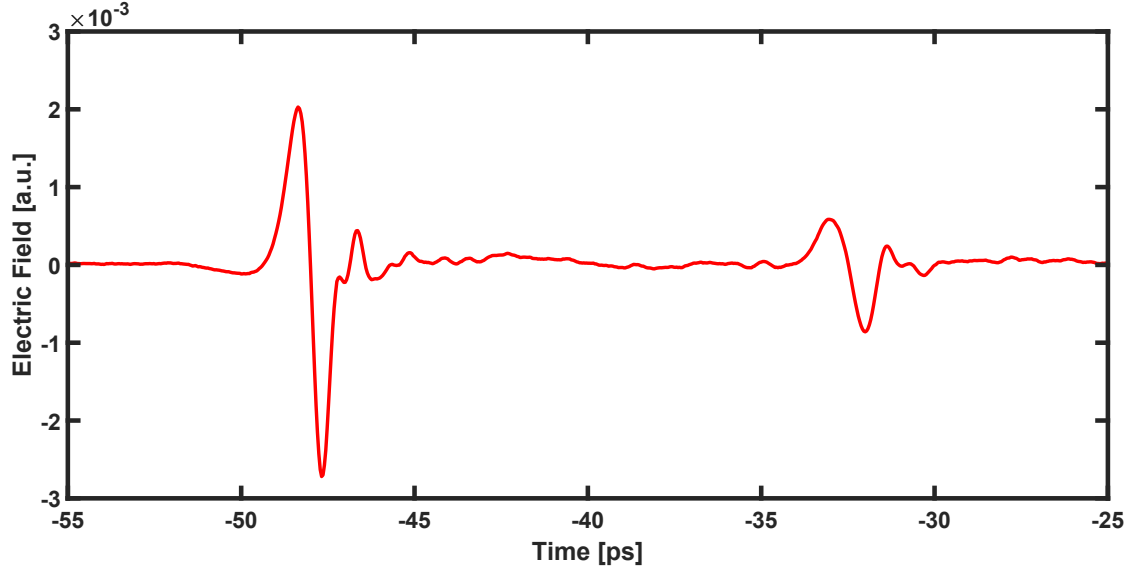
Figure 3.9: Time Domain Scan of THz transmission through a thin film of $SrTiO_3$ on LSAT. The back-reflection of the THz pulse from the back of the LSAT, off of the thin film, then transmitting again through the back of the substrate can be seen ~15ps after the first transmitted pulse. Since this back-reflection is separated from the main pulse in time enough, it can be windowed out and does not need to be considered for calculation of optical properties in equation 3.15.

shown in figure 3.9. For thin samples, the addition of all the internal reflections can be summed up in a geometric series, to give the following Fabry-Perot term.

$$F = \frac{1}{1 + R_{12}R_{21}e^{\frac{2i\omega d}{c}n_2}} \tag{3.12}$$

$$R_{12} = \frac{n_1 - n_2}{n_1 + n_2} \tag{3.13}$$

Now with all the individual ingredients for transmission through a medium, we can look at the transmission through a thick substrate. This will be made up of the transmission coefficients at the air-sample interface, the phase delay picked up during propagation, and the transmission coefficient at the sample-air interface. For a thick substrate the Fabry-Perot reflections can be windowed out, with a sacrifice in the spectral resolution. This gives the following transmission of the

substrate.

$$T_{sub} = T_{air,sub}P_{sub}T_{sub,air} = \frac{4n_{sub}}{(1+n_{sub})^2}e^{\frac{i\omega L_{ref}}{c}(n_{sub}-1)} \tag{3.14}$$

where n_{sub} is the index of refraction of the substrate, c is the speed of light, ω is the frequency of light, and L_{ref} is the thickness of the reference substrate. Next we can look at the transmission of the thin-film on the thick substrate, who will have transmission coefficients at each interface, phase picked up during propagation, and the Fabry-Perot term to account for internal reflections in the thin film. The total transmission will be given by the following.

$$\begin{aligned} T_{filmonsub} &= T_{air,film}F_{film}P_{film}T_{film,sub}P_{sub}T_{sub,air} \\ &= \frac{8n_{film}n_{sub}/(n_{film}+1)(n_{film}+n_{sub})}{1+R_{air,film}R_{film,sub}e^{\frac{2i\omega d}{c}n_{film}}}e^{\frac{i\omega d}{c}n_{film}}e^{\frac{i\omega L_{sub}}{c}n_sub} \end{aligned} \tag{3.15}$$

where n_{film} is the index of the film, and all other terms were previously defined. Both of the total transmission equations are somewhat complicated, but the benefit of using a bare substrate as a reference is that some of the effect of the substrate index on the transmission can be referenced out. The total transmission is then the ratio of the two, which causes some of the terms to cancel. The total transmission is given by the following formula.

$$T_{total} = \frac{\frac{2(n_{sub}+1)}{(1+n_{film})(n_{film}+n_{sub})}e^{\frac{i\omega d}{c}(n_{film}-1)}}{1+\frac{(n_{film}-1)(n_{sub}-n_{film})}{(n_{film}+1)(n_{sub}+n_{film})}e^{\frac{2i\omega d}{c}n_{film}}}e^{\frac{i\omega(L_{sub}-L_{ref})}{c}(n_sub-1)} \tag{3.16}$$

This is the technically correct equation that can be used to extract the optical properties of one medium on top of another, using a bulk slab of the other as the

reference substrate and measuring THz transmission. For the specific case of a thin film, this equation can be made even simpler by taking advantage of the following assumptions: $n_{film} >> n_{sub} > 1$ and $1 >> \omega d n_{film}/c$. In this case, the thin film transmission can be approximated by the following.

$$T_{total} = \frac{1 + n_{sub}}{1 + n_{sub} + Z_0 \sigma(\omega) d} e^{\frac{i\omega\Delta L}{c}(n_{sub}-1)} \tag{3.17}$$

where $\sigma(\omega)$ is the frequency-dependent optical conductivity, $\Delta L = L_{sub} - L_{ref}$ and Z_0 is the impedance of free space, 377Ω. It can also be inverted to directly write conductivity (or whichever optical constants are desired) in terms of transmission, the directly measured quantity.

$$\sigma(\omega) = \left(\frac{1 + n_{sub} e^{\frac{i\omega\Delta L}{c}(n_{sub}-1)}}{T_{meas}} - 1 - n_{sub} \right) \frac{1}{Z_0 d} \tag{3.18}$$

Here I am being explicit that the transmission used is the measured transmission of the thin film on a thick substrate with another substrate used as a reference. An example of a material where large changes to the THz optical conductivity show up going through a phase transition is a superconductor, which we will examine below, illustrating the information gained by the explained measurement and extraction process. Figure 3.10 shows the THz transmission through a thin film of the cuprate superconductor $YBa_2Cu_3O_{7-x}$ (YBCO) on a $LaAlO_3$ substrate over a wide temperature range. YBCO is a metal at all temperatures measured, and the decrease in the THz transmission demonstrates that it becomes more metallic as the temperature is decreased. Additionally, at lower temperatures the transmission shows a roughly linear increase in transmission from low to high frequencies, compared to the flatter response at high temperature. More insight into this behavior can be gained from looking at the optical conductivity, which can be directly

extracted from the transmission using equation 3.18.

The extracted optical conductivity for a few select temperatures is shown in figure 3.11. Looking first at the non-superconducting state conductivity, above 80K, we can see a few distinct features. First, the real part of the conductivity dominates over the imaginary part of the conductivity. Second it has very little dispersion over the THz range measured. Both of these are consistent with the Drude model in the limit where the scattering rate and the plasma frequency are very large, much larger than the THz bandwidth measured. This can be seen by looking at the Drude model conductivity, and taking the limits $\omega_p >> \omega$ and $\gamma >> \omega$.

$$\sigma(\omega) = \omega_p^2 \tau \tag{3.19}$$

On the other hand, at the lowest temperatures measured, deep in the superconducting state, we can see a very different behavior of the optical conductivity. Here the conductivity is dominated by a large imaginary part and very small real part. Although it is true that a gap opens in superconductors, which leads to a decrease in the real part of the conductivity, that is not actually necessary to capture the behavior of cuprate THz optical conductivity, and can be seen by looking at the Drude model and the behavior of the imaginary part of the conductivity. Additionally, in cuprates the gap has a momentum dependence and actually vanishes at some momenta, so the story of the gap is more complicated and won't be considered here. Contrary to the real part of the conductivity in the normal state, the imaginary part of the conductivity shows clear dispersion, with a $1/\omega$-like dependence in the THz range. This is actually also able to be seen from the Drude model in the limit that the scattering rate goes to 0 (consistent with zero resistance, a hallmark of superconductivity).

$$\sigma(\omega) = i\frac{\omega_p^2}{\omega} \tag{3.20}$$

The strength of the superfluid contribution to the conductivity, the plasma frequency, is directly proportional to the cooper-pair density as $\omega_p \sim \sqrt{n}$ where n is the cooper pair density. Examining the normal state and superconducting state optical conductivity shows that the effect that the superconducting transition has
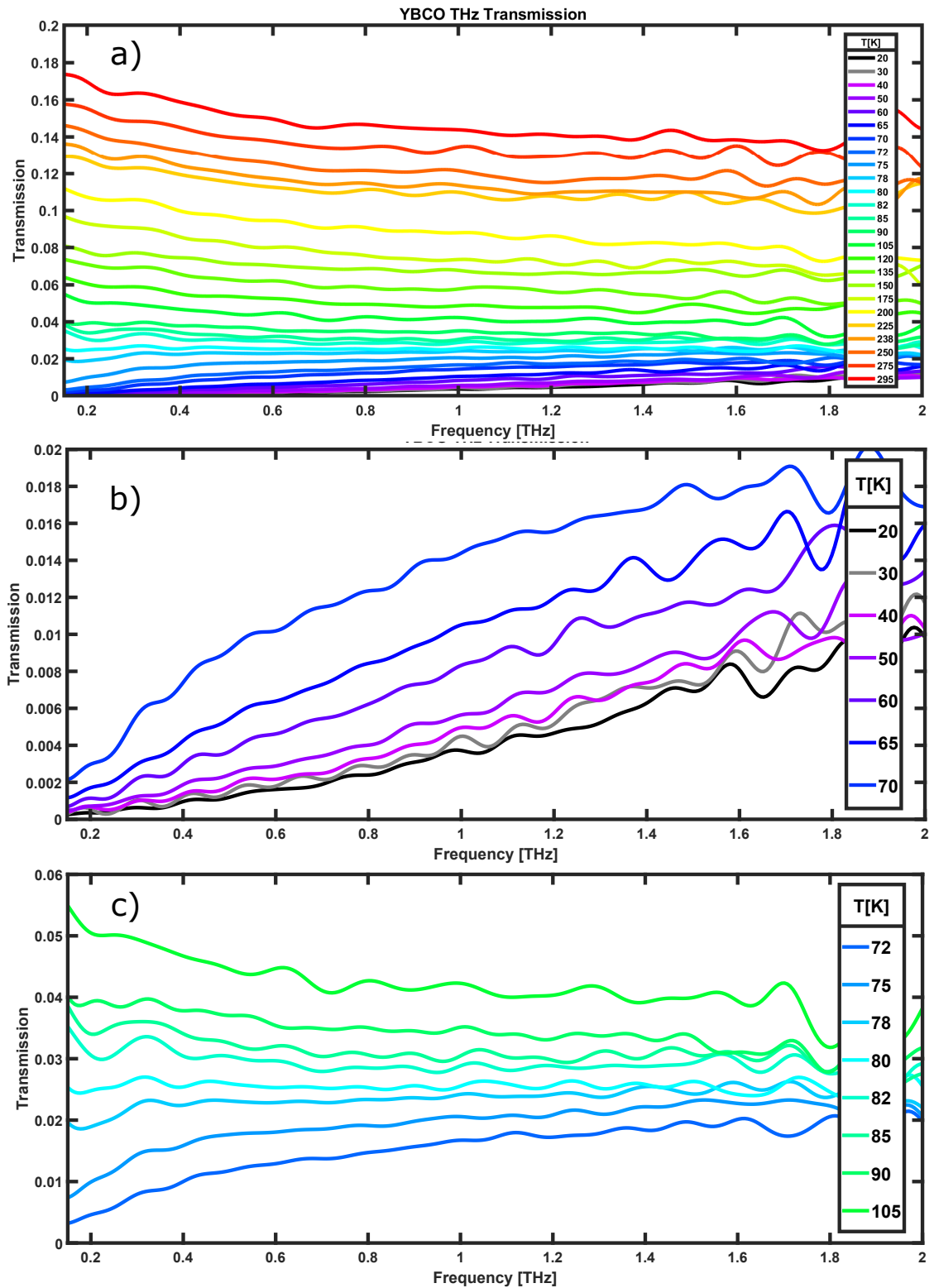
Figure 3.10: THz Transmission of YBCO for various temperatures in the normal state and in the Superconducting state. a) Shows all temperatures measured from 295 K to 20K. b) shows temperatures all within the superconducting state. c) Shows temperatures right above and below the transition.

on THz conductivity is essentially a decrease in the real part of the conductivity with a corresponding increase in imaginary part conductivity as qasiparticles join the condensate. The temperature evolution of the optical conductivity of a superconductor can be captured by the two fluid model which is a two-compenent Drude model with finite scattering rate and 0 scattering rate components[52].

$$\sigma_{2fluid}(\omega) = \omega_p^2 \left(\frac{(1 - f(T))}{\frac{1}{\tau} - i\omega} - f(T)\frac{i}{\omega} \right) \tag{3.21}$$

where $f(T)$ is the fraction of electrons participating in superconductivity at a given temperature. In the two fluid model the total density of electrons is kept constant, and what changes as a function of temperature is the fraction of the total density of electrons that are in the superconducting state, along with the quasiparticle (non-superconducting electrons) scattering rate. This is able to qualitatively capture the gradual decrease in real conductivity and increase in $1/\omega$ imaginary conductivity as a superconductor is cooled through the superconducting transition and deeper into the superconducting state.

3.2   Optical Pump-THz Probe Spectroscopy

In addition to being able to measure the equilibrium properties of solids, THz-TDs is also amenable to measuring non-equilibrium properties of solids in pump-probe experiments, particularly since the THz generated using the techniques described above generates ∼ps pulses. There are a huge variety of possible states that can, in principle, be induced by carefully chosen pumps, with unique signatures in the THz range, some of which may not even fit with the conventional linear-optical-properties analysis that was described in the previous section. Nevertheless, when probing with THz there are two basic kinds of measurements one can do that give different, yet complementary information, which I will illustrate with two experiments performed by the author.
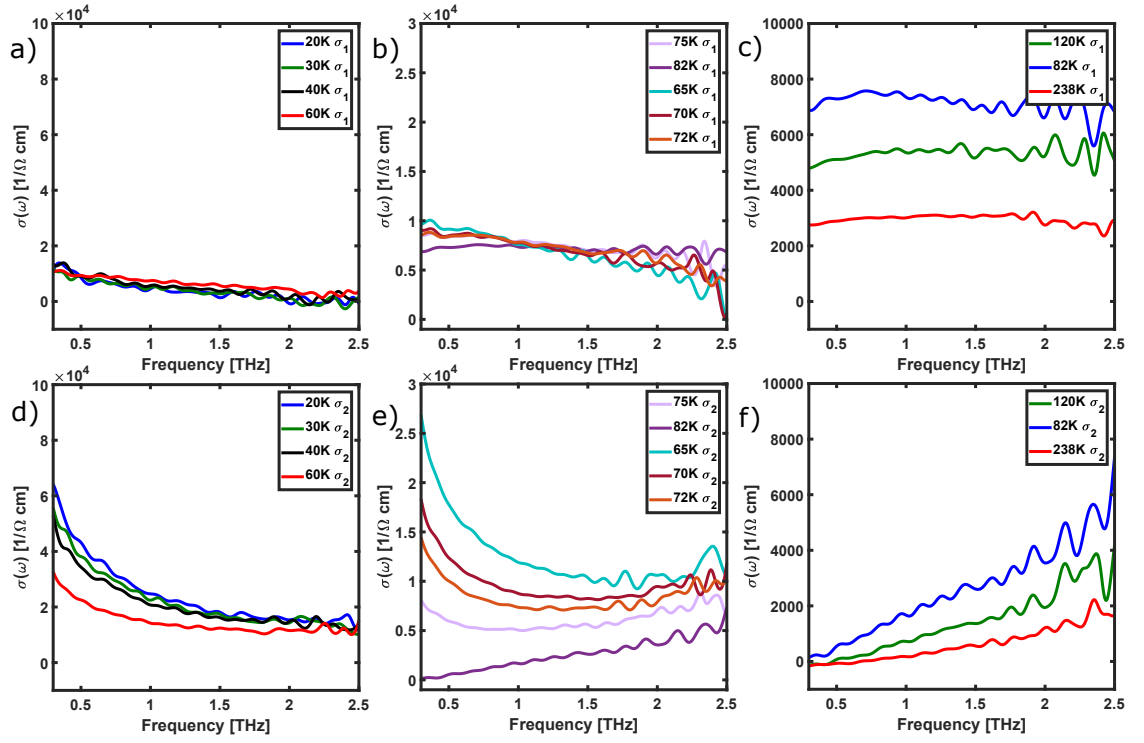
Figure 3.11: Optical conductivity of YBCO thin films extracted from transmission, with a-c) the real part and d-f) the imaginary part for temperature ranges deep within the superconducting state a,d), near T_c b,e) and in the normal state c,f).

The first kind of Optical pump, THz probe (OPTP) measurement one can perform is a "1-d" scan. With the introduction of a pump beam into a THz-TDS experiment there are now two time axes associated with the experiment. First there is the gate time, which is the time axis along the THz probe pulse. For example, the previously shown THz scans, such as in figures 3.1, 3.4, 3.6, 3.7, and 3.9 are all scanned along this gate time, which is varying the time between the THz probe pulse and the gate pulse in the detection scheme (either the EOS crystal or the PCA). In pump-probe experiments there is also the pump-probe delay time, which is the time between the pump and probe pulses at the sample. A "1-d" scan is when the gate-time of the THz pulse is fixed, and the pump delay is changed. Explicitly what is being measured here is how much the transmitted THz pulse at a single point in time is changing as the delay between that and a pump pulse is changed. What this means physically is essentially that the change in THz properties averaged over the entire spectrum is being measured. One conclusion that can be taken from this is that 1-d scans are most meaningful when the pump-probe dynamics do not create clear phase shifts in the THz pulse and when the spectroscopic signatures of the photoexcited change are not changing a lot during the pump-probe delay. If either of these is the case, this can cause changes that can only truly be captured by measuring the entire photoexcited THz pulse at each pump delat,as described in the next chapter. That being said, 1-d scans are a good, and much less time-intensive way, to capture the overall THz-energy scale photoinduced dynamics. An example of a THz 1-d scan measurement is shown in 3.12, where Sr_2IrO_4 was pumped with an above gap, 800nm pump. The dynamics are well-characterized by a fast rise, an exponential decay, and a long-lived offest. The overall amplitude of the signal increases with increasing fluence.

In the case of Sr_2IrO_4, the pump is above the electronic gap, so it is introducing electronic excitations, called quasiparticles. The fast decay time of the pump-probe 1-d scan can then have information about the lifetime of the photoexcited quasiparticles. A complementary but not fully equivalent way to interpret the fast time scale is as a measure of the time for energy that is put into the electronic system (by the pump) to go into the lattice and other degrees of freedom and reach

a quasi steady-state. In this case the relaxation will be related to electron-phonon coupling, and this behavior can be captured by the two-temperature model [53]. The long-lived offset of the signal can then be understood as increased reflectivity due to net heating of the sample.

The second kind of OPTP measurement one can perform is a "2-d" scan, where both the pump and THz gate time are varied. This enables one to measure the change in the transmission or reflection of the entire THz pulse, which means this information can be Fourier transformed to obtain spectroscopic dynamics of the photo-induced state. One clear example showing this is measuring the properties of photoexcited carriers in GaAs. Figure 3.13 shows a measurement of photoinduced THz reflectivity of GaAs after being excited with an 800nm (above bandgap) pump pulse. The equilibrium THz reflectivity is shown as the black curve in figure 3.13a, which is flat and relatively featureless, consistent with a semiconductor with very few carriers in equilibrium. The loss function is flat and featureless, ϵ_1 is relatively flat and positive, and ϵ_2 is small, all consistent with this picture. Upon photoexcitation, the photoinduced reflectivity shows a clear plasma edge, seen as the red curve in figure 3.13a. This is consistent with a Drude response arising from the photoexcited carriers where the plasma frequency is in the THz regime. This is corroborated by the loss function showing a peak at around 1 THz, similar to the plasma edge in reflectivity, the crossover of the photoinduced ϵ_1 going from positive to negative, crossing 0 at $\sim 1THz$, and ϵ_2 showing the $1/\omega^2$ dependence.

3.3   Mid-Infrared Pump, Optical Probe

Many of the relevant excitations and degrees of freedom in quantum materials lying in the THz and mid-infrared (mid-IR) means that THz pulses can be used not only to measure these excitations, but also to drive them nonlinearly with strong THz or mid-IR pulses. The generation of high-field THz pulses with optical rectification in LiNbO$_3$ has already been discussed. To generate strong pulses in the mid-IR frequency regime, we use difference frequency generation (DFG) in GaSe, and measure pump-probe dynamics with an optical probe. This section will review
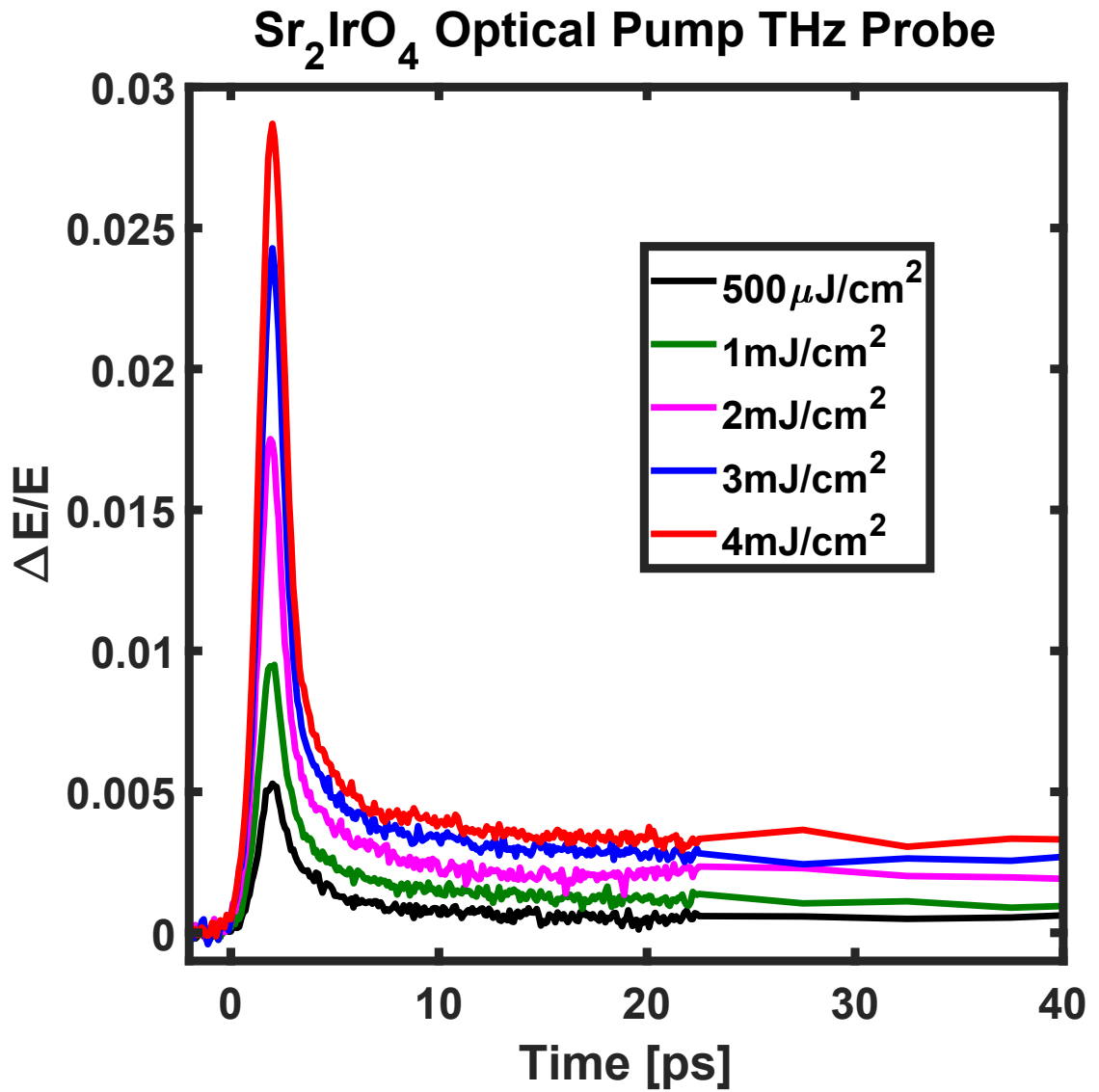
Figure 3.12: Optical Pump THz Probe 1d scans on Strontium Iridate, varying fluence from $500\mu J/cm^2$ to $4mJ/cm^2$. These measurements were performed on a single crystal of Sr_2IrO_4 in reflection geometry at 80K.
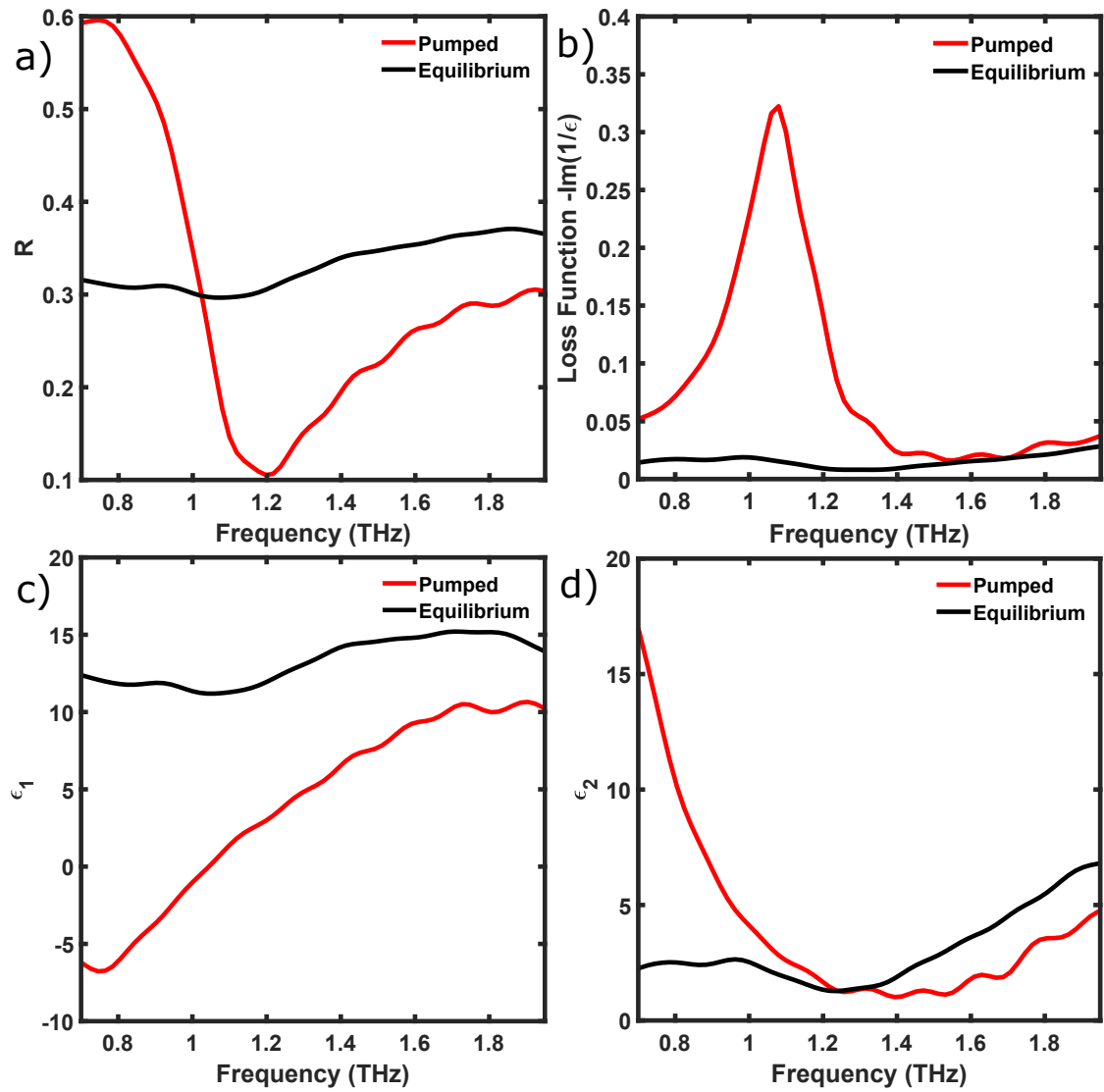
Figure 3.13: Optical Pump THz Probe 2d scans on GaAs, showing photoexcited a) reflectivity, b) loss function, c) ϵ_1 and d) ϵ_2.

the details of getting to a working mid-IR pump, optical probe configuration.

3.3.1   Mid-Infrared Pulse Generation

The mid-IR pulses used in experiments in this thesis were generated using DFG in a GaSe crystal. The pulses that were mixed in the GaSe crystal were generated by a commercially TOPAS-TWINS noncollinear optical parametric amplifier (NOPA). The TOPAS-TWINS is a set of two NOPAs where the pulses are generated from the same white-light source, and then pumped and amplified in two separate arms, allowing their wavelength to be tuned independently. In this section I will review some of the practical actions taken when generating mid-IR pump pulses in this experiment. Additional detail on the basics of the design can be found in [54, 55, 56].

Starting with the NIR generation beams for the DFG, a consideration to be made is that the output wavelength of the TOPAS commercial OPA is sensitive to the alignment into the OPA. What this means is that even if the light is aligned into the TOPAS and OPA light is being generated with powers similar to past instances (200-300mW), the output wavelength may not match the set wavelength in the OPA software. For example, upon explicitly checking the output wavelength, we've found a value off from the software setting by up to 15nm, which can lead to the DFG output being off from the desired wavelength by as much as a micron.

Next, the OPA output from both arms of the TOPAS need to be combined in the GaSe DFG crystal in the same spot at the same time for maximum mid-IR generation efficiency. To be able to tune the temporal overlap between the generation beams one of the output beams is on a delay stage. Spatial overlap of the beams is also not too difficult to obtain since both of the the OPA beams generate their own SHG in the GaSe crystal, which for the NIR wavelengths here is orange or red by eye. As long as temporal overlap has been achieved, rough spatial overlap of the two beams can be achieved by overlapping the two visible SHG spots on the crystal. Once some mid-IR power is generated, one can tune all parameters (DFG crystal angle, spatial and temporal overlap of the generation beams, and focusing into the crystal) to maximize power. To ensure that what is

being measured is truly the DFG power, a long-pass filter is placed right after the generation crystal so that only the mid-IR is transmitted. For GaSe, we have found that maximizing the output solely for power always gets us towards a wavelength of $9\mu m$. Once sufficient optimization has been done for power at $9\mu m$, one can then tune to the desired wavelength. Generally the maximum achievable power in this experimental setup at $9\mu m$ is around 10mW. The two parameters that most straightforwardly determine the output wavelength of the DFG process are the input beam energies, since the output is their difference, and the angle of the crystal, since this determines the phase-matching condition. In reality, for given pulse energies and crystal angles a variety of mid-IR output wavelengths can be generated, so one can't simply set the OPA output and crystal angle and optimize power. In reality to set the mid-IR wavelength one gradually changes the crystal angle and OPA output in the direction one wants to go (OPA pulses closer in energy along with a crystal more normal to the incoming beams for longer wavelength output and further apart in energy along with a less normal crystal for shorter wavelength output), while re-optimizing for power as you go. Once parameters are pretty close to give the desired output wavelength based on calculations, align the output beam into the prism spectrometer to see the current wavelength. Then, while watching the spectrum on the spectrometer, tune spatial overlap, temporal overlap, and crystal angle to make the spectrum redshift and blueshift towards the desired output wavelength. After shifting the spectrum as close as possible to the desired output, one can then measure the mid-IR power again and make some minor adjustments to optimize it, before realigning into the prism spectrometer and tuning the wavelength again closer to the desired output. This process essentially then needs to be iterated until one gets the desired power and output spectrum. After setting the power and spectrum with the prism spectrometer, the spectrum should be measured with the interferometer, which will be described in more detail below.
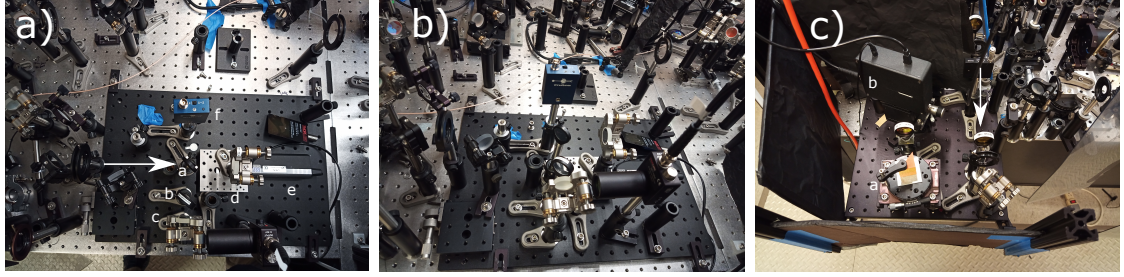
Figure 3.14: Pictures of mid-IR spectrometers used to characterize mid-IR pump pulses. a) Top-down view of interferometer, incoming mid-IR is indicated by white arrow. It will then be split by the KBr beam splitter (a), to arm 1, with a KBr beam compensator (b) and its mirror (c). The beam that transmits through the beamsplitter will go to arm 2, reflecting off its mirror (d) which is on a delay stage (e). Both beams are recombined and measured with a WiredSense detector (f) with the delay adjusted, changing between constructive and destructive interference of the two arms. b) Perspective view of the interferometer. c) Prism spectrometer, the incoming beam is indicated by the white arrow. The beam is dispersed by the ZnSe prism (a) and is measured with a Pyreos detector (b).

3.3.2   Mid-Infrared Pulse Characterization

Characterizing mid-IR pulses is actually a nontrivial procedure, since they are too low-energy to show up on many conventional photodiodes, and this also does not give any information about the frequency content of the pulses. At the same time, they are generally high-enough in frequency that they can only be measured by Electro-Optic-Sampling (EOS) with very broadband, compressed pulses, which are not trivially generated by many conventional ultrafast lasers. For the pulses in this thesis, we use two different methods for characterizing the mid-IR pulses, which have their own advantages as will be discussed below.

The first method used to characterize the mid-IR pulses is interferometry. This is where a mid-infrared pulse is split by a beam splitter, the two arms of the interferometer go through close but slightly different path lengths, and the pulses are recombined in a photodetector. The photodetector used is a WiredSense MPY-01 pyrodetector, which is sensitive both at mid-IR and optical wavelengths, which aids in alignment. A schematic of the interferometer is shown below.

To measure the pulses, the path length of one of the arms of the interferometer is varied with respect to the other, which will cause the pulses in each of the two

arms of the interferometer to interfere constructively and destructively when the peaks and troughs overlap. This interferogram can then be Fourier transformed to obtain the spectrum of the pulse. An example pulse and the corresponding Fourier transform are shown below, along with a measurement of the HeNe beam with the interferometer. For realistic alignment of the interferometer, it is easier to use a HeNe beam first since it can be seen by the eye, then making the mid-IR beam colinear with the HeNe beam.

Although the interferogram is an accurate way to characterize the mid-IR pump pulses generated, it does create some difficulties when optimizing the mid-IR output and setting the wavelength. This is because each interferogram is generated by a scan of the delay stage, which for our pulses takes about 15 minutes for an acceptable signal to noise. For setting the mid-IR wavelength, an active, "real-time" measurement of the spectrum is necessary. This is why a second way of measuring the mid-IR light is necessary, using a prism spectrometer that was designed and built by a lab-member (Mustafa Ali). The essential idea is that the mid-IR pulses are sent through a ZnSe prism, which spatially spreads the mid-IR pulses exiting the prism. Then a photodetector with a series of spatially separated detectors individually measure the amplitude of the spectral content at different wavelengths. Since all of the different wavelengths are being measured simultaneously, it is possible to use this to have a real time measurement of the spectrum. An example of a mid-IR pump spectrum measured with this interferometer is shown below.

There are a few reasons this is not the sole spectrometer used to characterize the mid-IR light in our lab. First, the spectral precision is much lower than the interferometer, since each wavelength has its own detector and there is a finite number of pixels. Second, this spectrometer is more at risk of having slight inaccuracies during alignment. This is because the spectrum measured is a result of the spatial dispersion of the beam throuh a prism, so changes to the pointing of the beam going into the spectrometer will change the output spectrum. These effects are minimized by using a pinhole at the entrance to the spectrometer, but they are not completely eliminated. Although an accurate measurement of the pump spectrum can be obtained by aligning well into the spectrometer, various tunings
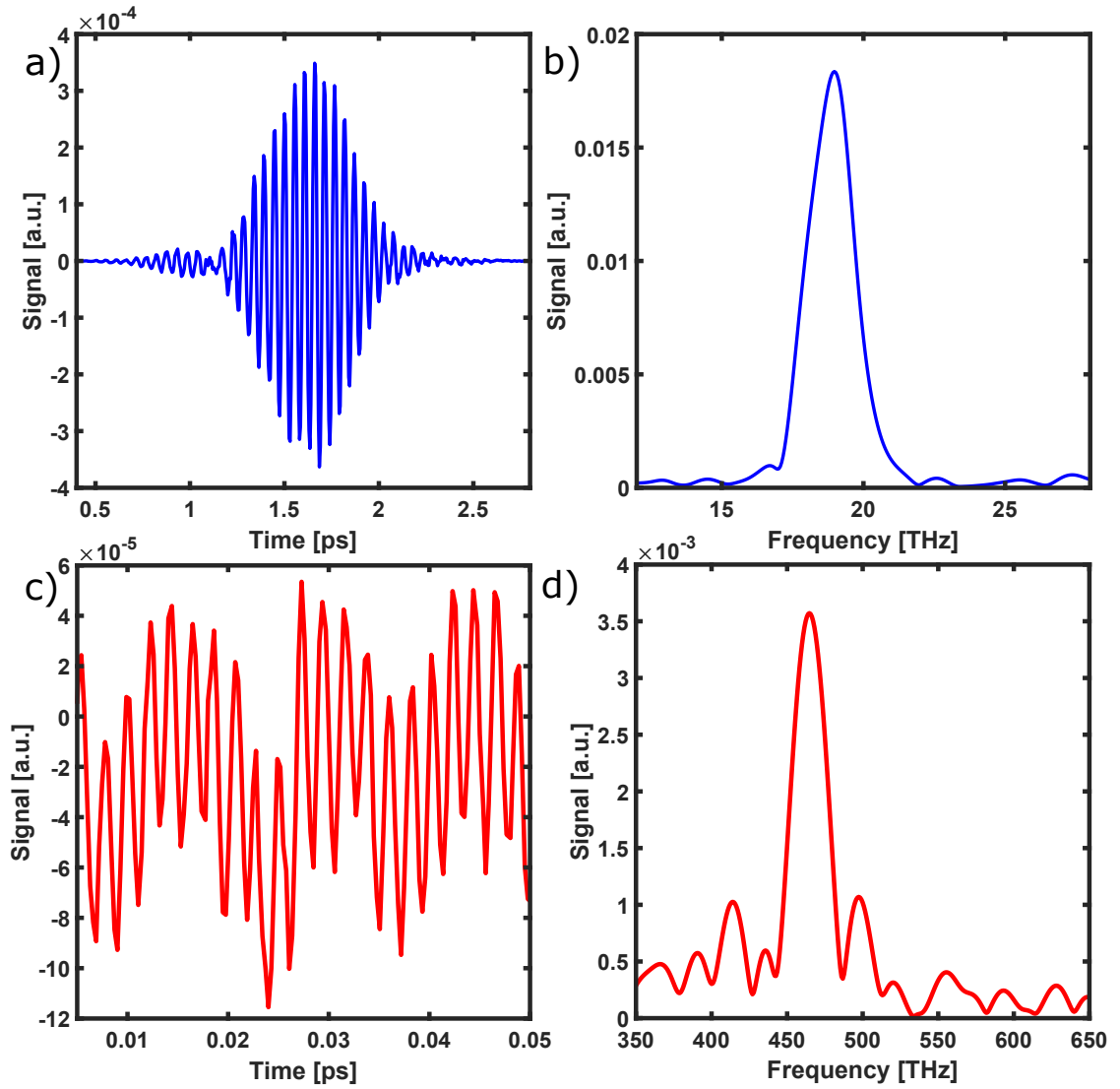
Figure 3.15: Example interferograms a) Direct time-domain interferogram of a mid-IR pulse and b) its spectrum. c) Interferogram of a HeNe beam, which is good for initial alignment of the interferogram and d) its spectrum.
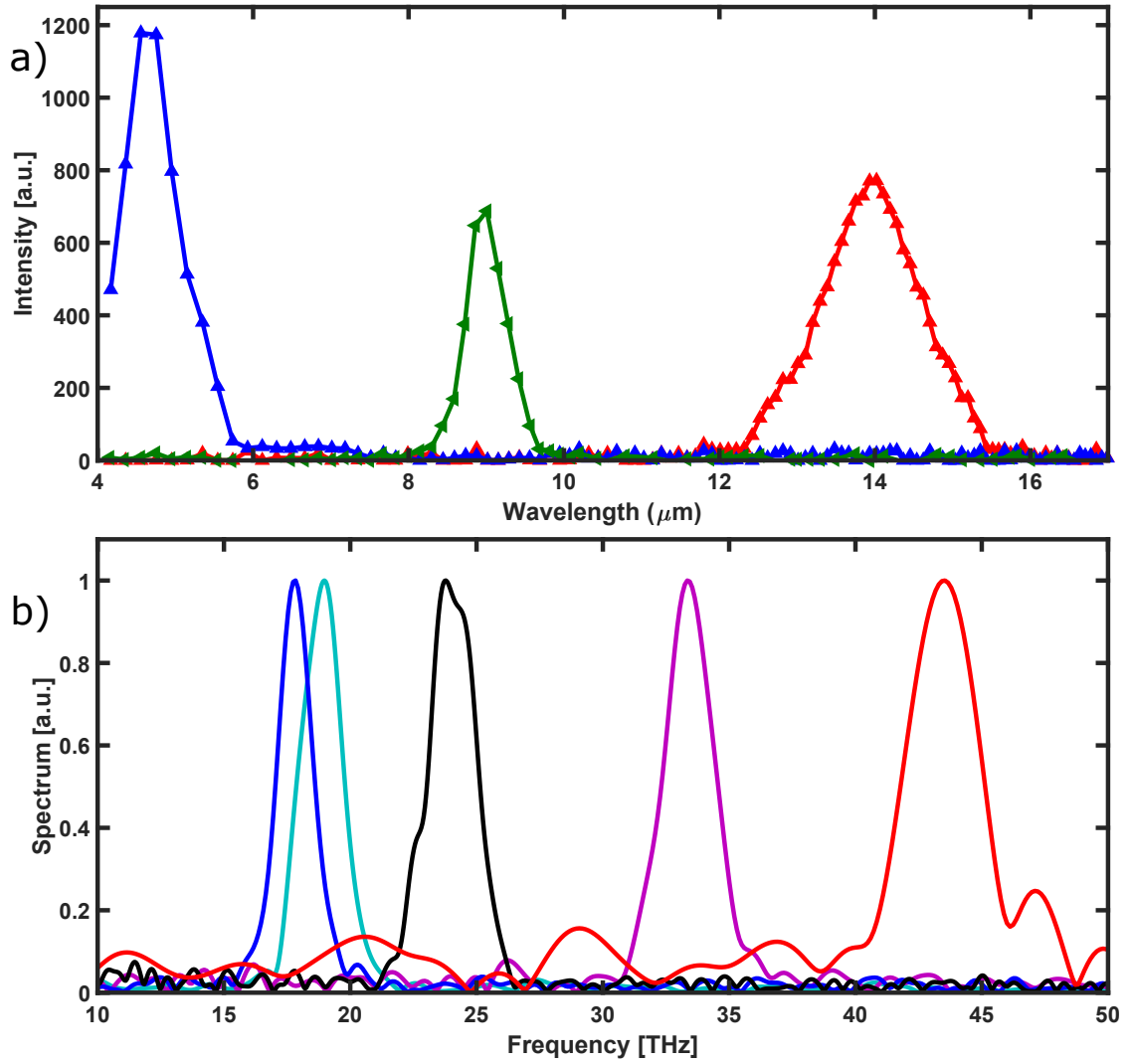
Figure 3.16: a) 3 Representative pump spectra generated by the mid-IR experiment measured on the prism spectrometer. b) 5 Representative pump spectra generated by the mid-IR experiment measured on the interferometer.

done to increase pump power and change the wavelength do slightly change the pointing of the mid-IR out of the generation crystal. So the mid-IR would have to be real-time realigned into the spectrometer while tuning parameters to have a fully trusted pump spectrum. This spectrometer is, however, good at measuring relative changes, so for example when the desired pump wavelength is much longer or shorter than the current set wavelength, this spectrometer can be used to know relatively that the pump is tuned in the right direction, even if the central value is not completely accurate. Thus, both spectrometers are used to characterize the pump beam used for mid-IR pump, optical probe experiments.

3.3.3   Mid-Infrared Pump, Optical Probe Experiment

In this section I will discuss some of the finer details to setting up the mid-IR pump, optical probe experiment that has been used to measure dynamics of various different compounds during the course of this thesis. This section includes the steps taken once the pump pulse has been set and characterized.

For the mid-IR pump, optical probe experiment, both the pump and probe beams need to be focused and overlapped in the same place at the same time, where then changes in the optical probe reflectivity can be measured as a function of pump-probe time delay. First, multiple optics are needed to get the pump to the sample spot. As stated, a long-pass filter is first used to filter out any second harmonic and sum frequency generation that the DFG crystal produces. It would be possible to then bring this beam to an off-axis parabolic mirror to focus it at the sample spot. However, with the current beam size of the output of the DFG crystal ($\sim$3.5mm $1/e^2$) and the long wavelength of the light, the minimum focused beam size possible for light with wavelength of $9\mu m$ is $340\mu m$ $1/e^2$ (given the 4 inch focal length parabolic mirror used for focusing). To be able to focus the beam down further, we expand the beam before focusing it down. Although this could be done with a pair of lenses, since the pump beam will be varied over a large wavelength range, it is desired to use achromatic optics for this. This is why a pair of off-axis parabolic mirrors (OAPs) is used. Here the ratio of the mirrors focal lengths is four, to expand the beam by a factor of 4. This is then steered to

a 4-inch focal length OAP which is used to focus the beam down onto the sample spot. With the beam expanded, mid-IR pump beam sizes as small as ∼60 microns (diameter) have been achieved. To have a properly focused beam with minimal aberrations, the steering into the OAP and the OAP angle should be tuned while observing the beam on a THz FLIR camera.

Once the pump has been properly focused, the probe beam must be focused and overlapped to the pump beam spot. For focusing of the probe, a lens is used. Since 800nm is a much shorter wavelength than the mid-IR pump, it is not necessary to use an expanded beam or steep focusing optic to achieve usable beam sizes, with a one half or one third meter focal length lens probe beam sized below 50 microns can be achieved. Spatial overlap of the pump and probe beams is then needed for pump probe dynamics, to do this a pinhole is used. By putting a power meter behind a pinhole, one can measure the pump-probe beam sizes as well as achieve overlap by having both beams go through the pinhole at a fixed position. Since the pump must be more carefully aligned into the focusing optics, the pinhole must be moved into the position of the pump beam, as opposed to moving the pump beam to a given pinhole position. This can be tricky to do with a pinhole of ∼100 microns and a pump beam of ∼100 microns since these are both small. To aid in this, one can align a HeNe path through the pump path, and then move the pinhole to the position that the HeNe goes through it, then turn the pump beam on again and it will be as close as the care taken to align it to the HeNe. Another way to make it easier to align the pinhole to the mid-IR is to go away from the focus, where the beam is larger. Once the pinhole is aligned to the pump, it's position should stay fixed for probe alignment. The probe can be aligned through the pinhole fairly easily by making it intense enough to see by eye. Caution is needed though as it is also easy to burn the pinhole with the probe, so it should be made just barely visible.

Once the pump and probe have been made collinear, a sample can be put into the experiment and the detection optics aligned. For time-resolved reflectivity and transmission measurements there aren't too many careful considerations needed, as the probe light just needs to be routed from the sample to the photodiode detector

without clipping on any mirrors. Since the probe is focused onto the sample, a lens or another optic will be needed to used to re-collimate the light.

At this point the experiment should hypothetically be aligned, although in reality some tuning of pump and probe overlap by improving a found pump probe signal is generally necessary. The best way to do this successfully is to have a good calibration crystal, that will have a relatively large, long-lived mid-IR pump optical probe signal at room temperature. Although GaAs is a very good calibration crystal for experiments with optical pumping, since an optical pump generates carriers in the conduction band that cause a huge change to the optical response of the crystal, we have not found that it has a very big mid-IR pump, optical probe signal since the pump photon energy in this case is 10-20 times smaller than the gap energy. A sample that we have found works very well as a calibration crystal for mid-IR pump experiments is Cd_3As_2. This is a semimetal that hosts a lot of interesting, rich physics, including being a 3d dirac semimetal, having extremely high carrier mobility, and possibly hosting non-trivial topological phases [57]. However, all of these details are not particularly important to us (nor is an 800nm probe at room temperature a particularly sensitive probe for this). What is important is that this sample is a semimetal with a Dirac point that, in thin-films grown by our collaborator [58], is generally $\sim 100 meV$ below the fermi-energy. This means that there are excitations at low-energies that can be pumped in the mid-IR and give a pump-probe response. The measured pump-probe response on a Cd_3As_2 thin film sample for a variety of mid-IR pump wavelengths is shown in figure 3.17. What is key here, to act as a good calibration crystal, is that the signal is large and quite noticeable for even the lowest pump-energy used, and that it is relatively long-lived, meaning that if you are unsure of the exact pump-probe overlap in time the long-lived response gives a larger window in time to look for the signal.
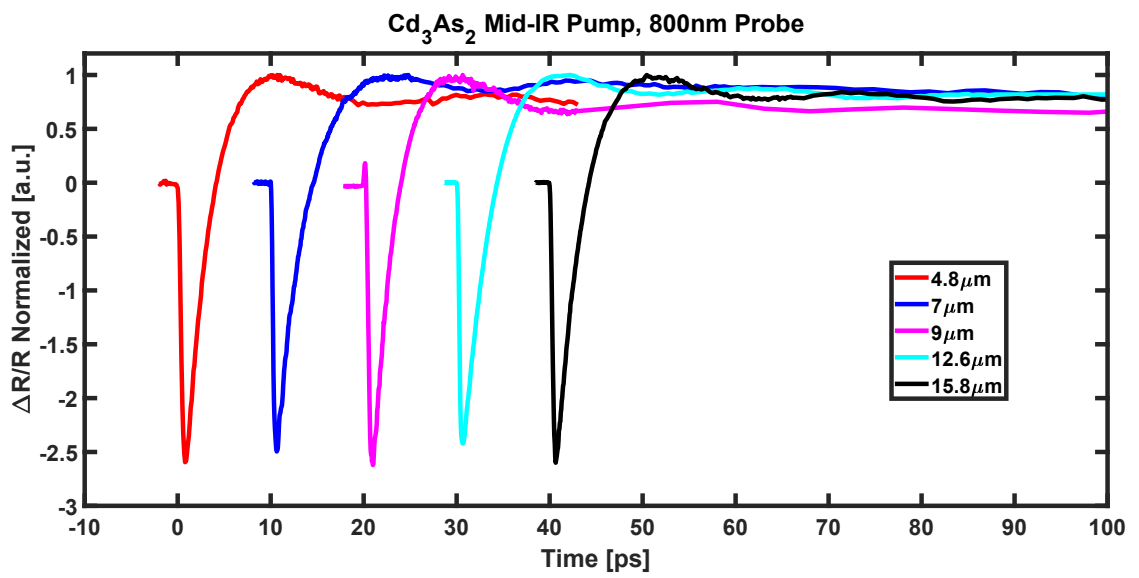
Figure 3.17: Normalized mid-IR pump, 800nm probe scans for Cd_3As_2 for pump wavelengths spanning the shortest wavelengths generated by the GaSe experiment ($4.8\mu m$) to the longest wavelengths generated ($15.8\mu m$).

Chapter 4

Terahertz third harmonic generation in c-axis $La_{1.85}Sr_{0.15}CuO_4$

4.1   Abstract

In this section Terahertz nonlinear optics was used to investigate a supercon-
ducting collective mode, the c-axis Josephson phase mode, through THz high-
harmonic generation. Specifically, we have investigated the nonlinear c-axis re-
sponse of optimally doped $La_{1.85}Sr_{0.15}CuO_4$ using high-field THz time domain spec-
troscopy at field strengths up to $\sim 80kV/cm$. With increasing field, we observe
a distinct redshift of the Josephson plasma edge and enhanced reflectivity (above
the plasma edge) arising from third harmonic generation. The non-monotonic
temperature-dependent response is consistent with nonlinear drive of the Joseph-
son plasma mode (JPM) as verified with comparison to theoretical expectations.
Our results add to the understanding that, using THz light, the JPM (in addition
to the Higgs mode) provides a route to interrogate and control superconducting
properties.

4.2 Introduction

Terahertz spectroscopy has emerged as a powerful probe of non-equilibrium dynamics in quantum materials [2, 59]. More recently, the generation of intense terahertz (THz) high-field pulses has enabled nonlinear drive of the low energy electrodynamics, offering new insights into the many-body response while also providing a route for on-demand control of emergent properties [60, 61, 62, 4]. Superconductors are particularly amenable to high-field interrogation and manipulation of the condensate with terahertz pulses. This includes the Higgs amplitude mode in conventional superconductors where light couples non-linearly to the condensate, driving oscillations of the order parameter amplitude at twice the pump frequency, leading to harmonic generation [63, 64, 65, 66, 67, 68, 69]. Higgs mode spectroscopy has been extended to cuprate superconductors with novel mode dynamics associated with the d-wave gap symmetry and to iron pnictides where multiband effects have been observed [70, 71].

In the high-T_c cuprates the phase mode response (Josephson plasma mode – JPM) manifests at THz frequencies [36, 72]. Briefly, the copper-oxygen planes are weakly interacting and Josephson coupling dictates c-axis Cooper pair tunneling based on the interlayer phase difference of the superconducting order parameter between adjacent planes. This results in a plasma edge in the c-axis reflectivity at the Josephson plasma frequency ω_p. For single layer cuprates, ω_p typically manifests at THz frequencies with ω_p^2 proportional to the condensate density n_s (e.g., see Fig.4.1, discussed in more detail below). As such, the JPM serves as a reporter of the condensate response which includes nonlinearities such as field-induced renormalization of ω_p and harmonic generation [73, 39, 74, 75].

We investigate the nonlinear spectral response of c-axis $La_{1.85}Sr_{0.15}CuO_4$ (LSCO) using high field THz-TDS as a function of field strength and temperature. A redshift of ω_p with increasing field ($2.4\,\mathrm{kV/cm}$ up to $80\,\mathrm{kV/cm}$) arises from the Josephson effect. With increasing temperature the maximum redshift increases from $\sim$110 GHz at 10 K $\sim$220 GHz at 32 K. This temperature dependent frequency shift cannot be explained solely using the Josephson equations which predict a high-field shift of the JPM is a constant fraction of the equilibrium JPM frequency at each
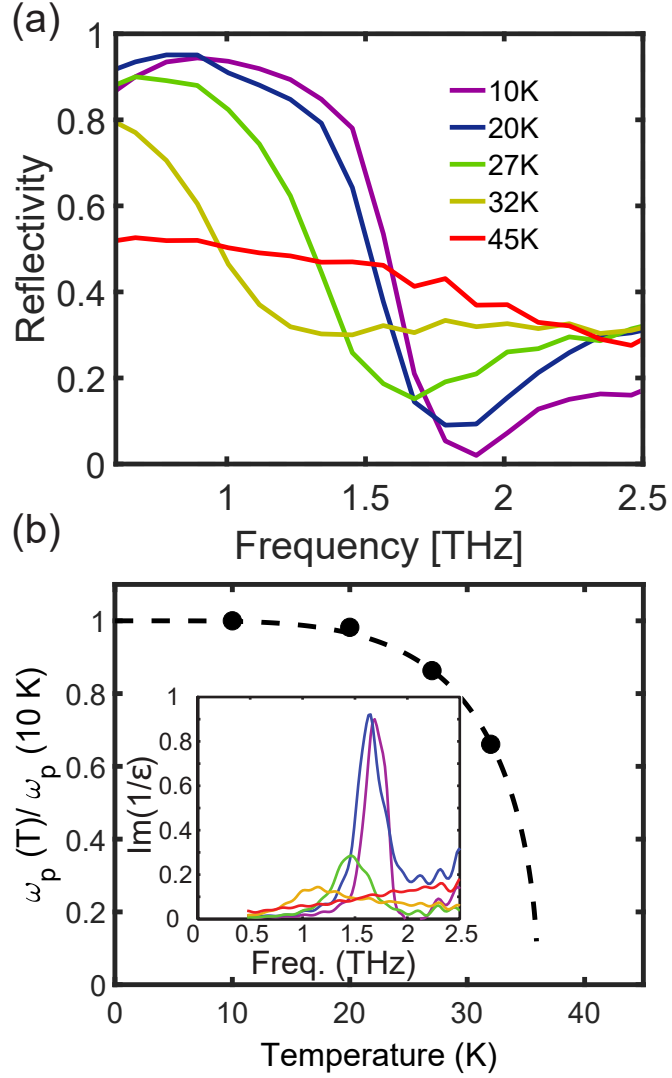
Figure 4.1: a) Low field c-axis reflectivity of $La_{1.85}Sr_{0.15}CuO_4$ at several temperatures. At 10K, ω_p is ~1.7 THz. b) Temperature dependence of ω_p below T_c normalized to the low temperature measurement $\omega_p(T = 10 \text{ K})$. The dashed line is a fit to a BCS-like order parameter temperature dependence, as described further in the text. The inset shows the (normalized) loss function, $-\text{Im}(1/\epsilon)$, using the same legend in panel a).

temperature. This is the opposite of the observed behavior, and could be related to increased quasiparticle damping at higher temperatures. Commensurate with this is broadband third harmonic generation above the plasma edge which exhibits a slight increase with decreasing temperature below T_c, dropping off in the normal state. The temperature dependence is compared with calculations based on the theory in Reference [75]. The qualitative agreement between calculations and experiment suggests that the temperature dependence is related to the competing factors of Josephson coupling strength, the resonance of the pump with the JPM, thermal population of excited plasmon states, and quasiparticle damping. For our broadband drive, we estimate a power conversion efficiency of $\sim 6 \times 10^{-5}$.

4.3 Methods

THz radiation is generated via optical rectification using a Ti:sapphire regenerative amplifier (1 KHz, 800 nm, 100 fs, 3 mJ) using tilted pulse front generation in a Mg-LiNbO$_3$(LNO) crystal [76, 77]. The THz output from the LNO crystal surface is collimated with a lens ($f = 120$ mm) and focused onto the sample with an angle of incidence of 15º and a beam diameter of $\sim$2.3 mm FWHM (pulse energy $\sim$2 μJ). Before reaching the sample, the THz light passes through a pair of wire grid polarizers which are used to attenuate the THz pulse, covering the range from 2 - 80 kV/cm. The reflected beam from the sample surface is collected and focused onto a 300 μm thick (110) GaP crystal for EO sampling. The GaP crystal is mounted on a 2 mm thick (100) GaP crystal to delay the internal etalon inside the GaP to times beyond our temporal measurement window. Roughly 1% of the pump beam is split off and used for gating the THz pulse in the GaP crystal. The entire THz beam path is in a vacuum chamber (schematic of the experimental setup is shown in Fig. 2a). The bandwidth of the pulses extends from 0.2 - 3 THz (see Fig. 3a) with a maximum at $\sim$0.65 THz. The full spectral content is used for the nonlinear studies and is not spectrally filtered.

The LSCO crystal was cut and polished to expose the a-c plane and was grown via a traveling-solvent floating-zone method [78] with a surface size of approxi-

mately 3mm × 3mm. Reflectivity measurements were performed by taking time domain scans of the electric field reflected off the sample and from a gold reference mirror at the sample position in both nonlinear and linear regimes. The reflectivity was then obtained by calculating the Fourier transforms of the time domain scans and taking their ratios, $R_{NL} = |E_{NL}(\omega)/E_{NL}^{Au}(\omega)|^2$. Measurements were performed above and below $T_c = 38$K as described below.

4.4 Results

We first measured the temperature dependent c-axis response at the lowest available electric field to characterize the linear response. The c-axis reflectivity is plotted in Fig. 4.1(a) for several temperatures above and below $T_c = 38$ K, and shows a clear plasma edge emerge and sharpen with decreasing temperature from 32 K to 10 K, coinciding with an increase in superconducting condensate. The low temperature (10K) plasma edge ω_p is at $\sim$1.7 THz is in agreement with previous c-axis measurements for $x = 0.15$ doping [36, 79]. Figure 4.1(b) shows the plasma frequency $\omega_p(T)$ normalized by the low temperature measurement $\omega_p(10$ K) and scales with BCS-like order parameter temperature dependence, as $\omega_p^2 \propto \tanh(2.26\sqrt{T_c/T - 1}))$ [80, 81]. The inset of Fig.4.1(b) displays the normalized loss function -Im($1/\epsilon$) at each temperature.

For frequencies below ω_p the reflectivity is $\sim$90%, whereas near-unity reflection is expected as $\omega \to 0$. This deviation is attributed to imperfect referencing since the sample size and beam diameter are comparable. This effect is more pronounced at lower frequencies as the focused THz beam diameter is frequency dependent. However, the low temperature $\omega_p(T)$ (and associated temperature dependence) is consistent with previous studies for $x = 0.15$ doping, indicative of a high-quality crystal. The reflectivity presented in Fig. 1 and 2 are normalized to match reflectivity measurements using Fourier transform infrared spectroscopy (FTIR) on the same LSCO crystal at 1 THz [82].

The nonlinear terahertz reflectivity results are shown in Fig. 2b-f. As shown in Fig. 2b (base temperature 10 K), two pronounced effects occur: There is a
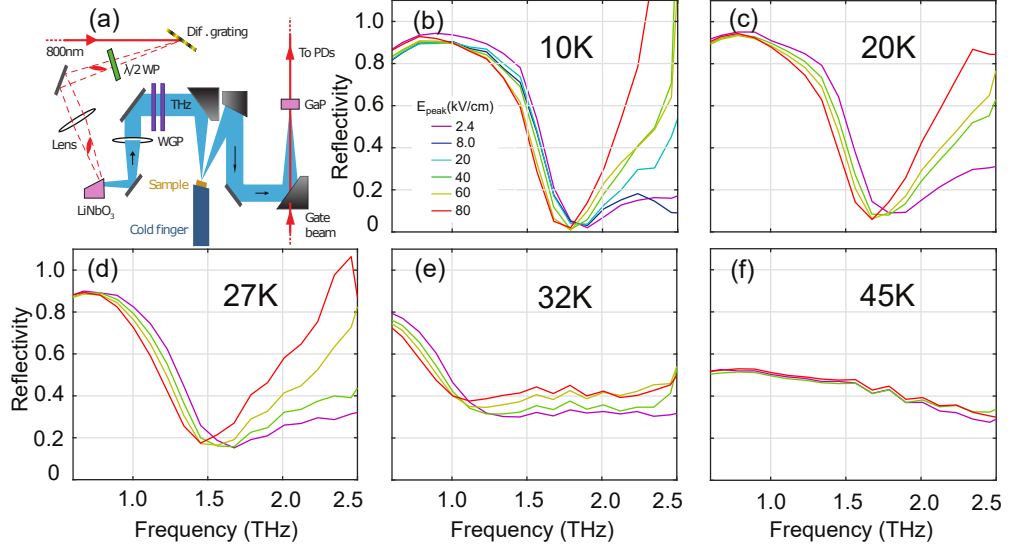
Figure 4.2: La$_{1.85}$Sr$_{0.15}$CuO$_4$ c-axis THz reflectivity. a) Schematic of experimental setup. Panels b)-f) show the reflectivity taken at temperatures 10 K, 20 K, 27 K, 32 K, and 45 K respectively. At each temperature, the reflectivity was measured for fields ranging from 2.4 – 80 kV/cm as indicated in the legend.

redshift of the plasma edge with increasing field and, above the plasma edge, there is an increase in the reflectivity corresponding to third harmonic generation (as described in greater detail below). With increasing temperature, there is a decrease in the condensate density, but there is still a clear redshift in the plasma edge and enhanced reflectivity. At 32 K (Fig. 2e), the plasma edge shift as a function of field is ~220GHz, larger than the ~110GHz shift at 10 K, but the reflectivity increase is relatively small. Above T$_C$ (Fig. 2f), there is no longer a superconducting response and the nonlinear increase in reflectivity is minimal to nonexistent. The nonlinear reflectivity data in Figure 2 is informative as it reveals both the JPM redshift and the increase in reflectivity above ω_p. However, the increase in reflectivity requires a more careful analysis as we now discuss.

Figure 3a plots the spectral amplitude of the electric fields reflected from the LSCO at 10K, comparing the reflectivity of the nonlinear (NL) and linear (L) response. The red curve is E$_{NL}(\omega)$ at the highest field (80kV/cm). The black curve is E$_L^*(\omega)$ at the lowest field, appropriately normalized to enable quantitative comparison with the spectral changes that arise in the nonlinear regime.

As with the reflectivity data in Figure 2, the redshift of the plasma edge is evident when comparing $E_L^*(\omega)$ and $E_{NL}(\omega)$ in Fig. 3a. Moreover, the increase in the spectral amplitude above the plasma edge is also evident (blue shaded region). The peak spectral amplitude of the terahertz pulses is at $\sim$0.65 THz. The second peak in $E_{NL}(\omega)$ is at $\sim$1.9 THz, consistent with third harmonic generation. The data in Fig. 3a reveals that the nonlinear signal is relatively small in comparison to the peak amplitude of the incident pulse (i.e.,$E_L^*(\omega)$ at 0.65 THz), but considerably larger than the spectral spectral amplitude of $E_L^*(\omega)$ between 2 - 3 THz. Nonetheless, the dynamic range is sufficient to enable a determination of the field dependence of the integrated spectral amplitude above the plasma edge (Fig. 3b), which further verifies that the enhanced signal arises from third harmonic generation (THG).

The THG response in Fig. 3(b) is quantified by integrating

$$E_{3\omega} \equiv \int \left[E_{NL}(\omega) - E_L^*(\omega) \right] d\omega \tag{4.1}$$

where $E_{NL}(\omega)$ and $E_L^*(\omega)$ are the reflected signals from the sample as defined above. To avoid integrating over the Josephson plasma edge, the integration is taken from 1.8 THz to 2.4 THz. Figure 4.3(b) displays the magnitude of the third harmonic $E_{3\omega}$ as a function of field strength at 10 K, along with a cubic polynomial fit (red line, R-squared value of 0.99). This further confirms the reflectivity/spectral amplitude increase arises from third harmonic generation in the superconducting phase. The lowest field strengths have more third harmonic intensity than the cubic fit, which may be attributed to the fit over-favoring the highest fields.

4.5   Discussion

The experimental observations can be further understood by examining the higher order terms in the phase dynamics of layered superconductors described by the Josephson equations [73, 37].

In a layered superconductor, the interlayer phase difference $\theta(t)$ changes with time according to the second Josephson equation

$$\frac{\partial \theta(t)}{\partial t} = \frac{2edE(t)}{\hbar} \qquad (4.2)$$

where $2e$ is the cooper pair charge, d is the interlayer spacing ($\sim$1 nm), $\hbar$ is Planck's constant divided by 2π, and $E(t) = E_0\sin(\omega_{\text{pump}}t)$ is an electric field along the c-axis with E_0 the field strength which oscillates at frequency ω_{pump}. Solving equation 4.2 yields the relation $\theta(t) = (2edE_0/\hbar)\cos(\omega_{\text{pump}}t)$. Since the c-axis superfluid density ρ_c scales as the order parameter phase difference, $\rho_c \propto \cos\theta$ and $\rho_c \propto \omega_p^2$ as shown in Fig. 4.1(b), the plasma frequency renormalizes according to $\omega_{NL}^2 = \omega_p^2\cos\theta(t)$ where ω_{NL} is the new Josephson plasma frequency under intense field strengths. By inserting $\theta(t)$ and expanding the ω_{NL} we arrive at

$$\omega_{JPM}^2 = \omega_{JPM0}^2\cos(\theta) = \omega_{JPM0}^2\cos\left[\theta_0\cos(\omega_{pump}t)\right]$$

$$\approx \omega_{JPM0}^2\left[1 - \frac{\theta_0^2}{4} - \frac{\theta_0^2\cos(2\omega_{pump}t)}{4} + \ldots\right] \quad (4.3)$$

where $\theta_0 = 2edE_0/\hbar$. From this expansion we can see that the next leading order term is subtracting, resulting in a redshift in the plasma frequency. This is what is observed below T_c for high fields as shown in Fig. 4.2.

The tunneling interlayer current depends on the phase difference as $I(t) = I_0\sin[\theta(t)]$, and solving for $I(t)$ gives the following.

$$I(t) = I_c\sin\left[\theta_0\cos(\omega_{\text{pump}}t)\right] \approx I_c\left[\theta_0\cos(\omega_{\text{pump}}t) - \frac{\theta_0^3}{6}\cos^3(\omega_{\text{pump}}t) + \ldots\right] \quad (4.4)$$

Where the leading higher order in the expansion is cubic. This expanded term leads to driving the current at the third harmonic and is observed as THz emission at 3ω, which manifests as a reflectivity increase above the plasma edge as shown in Fig. 4.2(a)-(d).

The above equations predict the third harmonic signal to scale with the superfluid density, as observed in previous work on LBCO [74]. The temperature dependence of the third harmonic emission for our LSCO studies is shown in Fig.
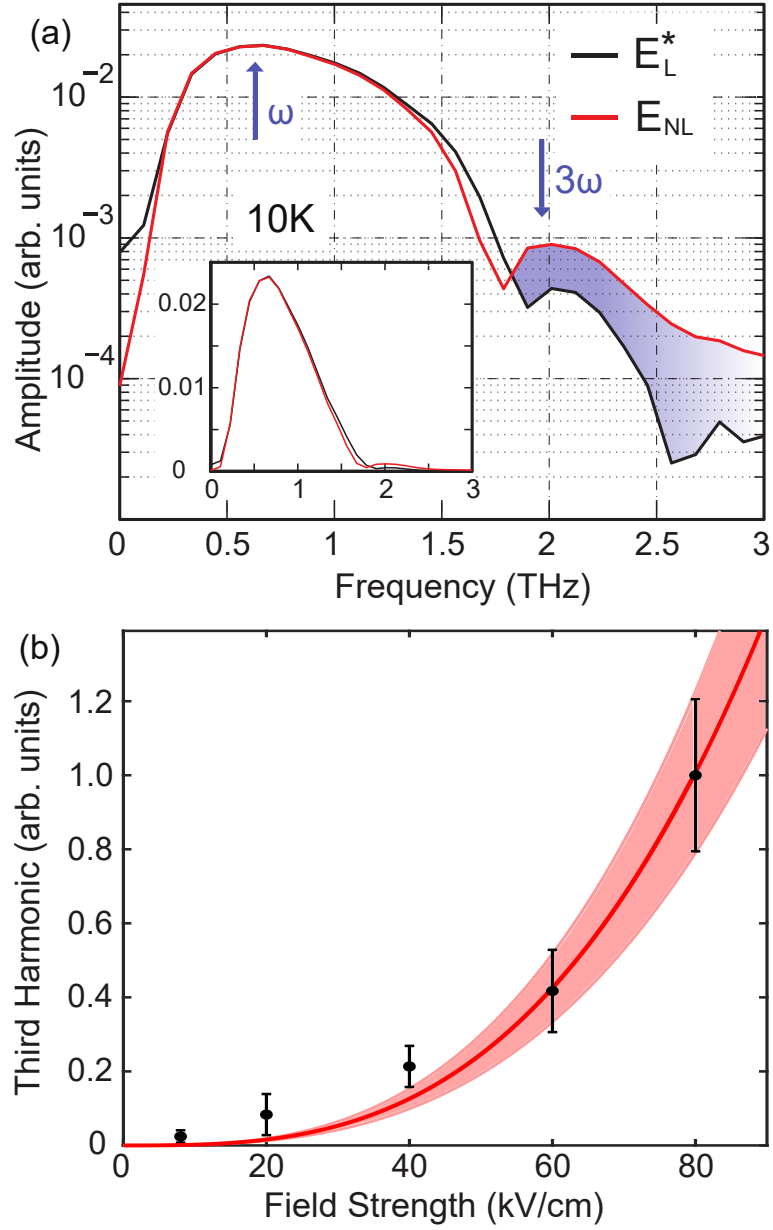
Figure 4.3: Third harmonic generation from c-axis LSCO at 10K. a) Linear (black) and nonlinear (red) spectral amplitude of the THz pulses reflected from the sample. The nonlinear spectrum is at the maximum field strength of $\sim$80 kV/cm, and the linear spectrum is at the minimum field strength (renormalized as explained in the text). The shaded region in blue is the spectral content attributed to third harmonic generation. The inset contains a plot of the spectral amplitudes with a linear y-axis. b) Third harmonic generation as a function of incident THz field strength at 10K. Each data point is from integrating Eq. 1 over the third harmonic region. The red line is a cubic polynomial fit, and the shaded area is bounded by cubic fits of the data including the upper and lower bounds of the data including the error bars.
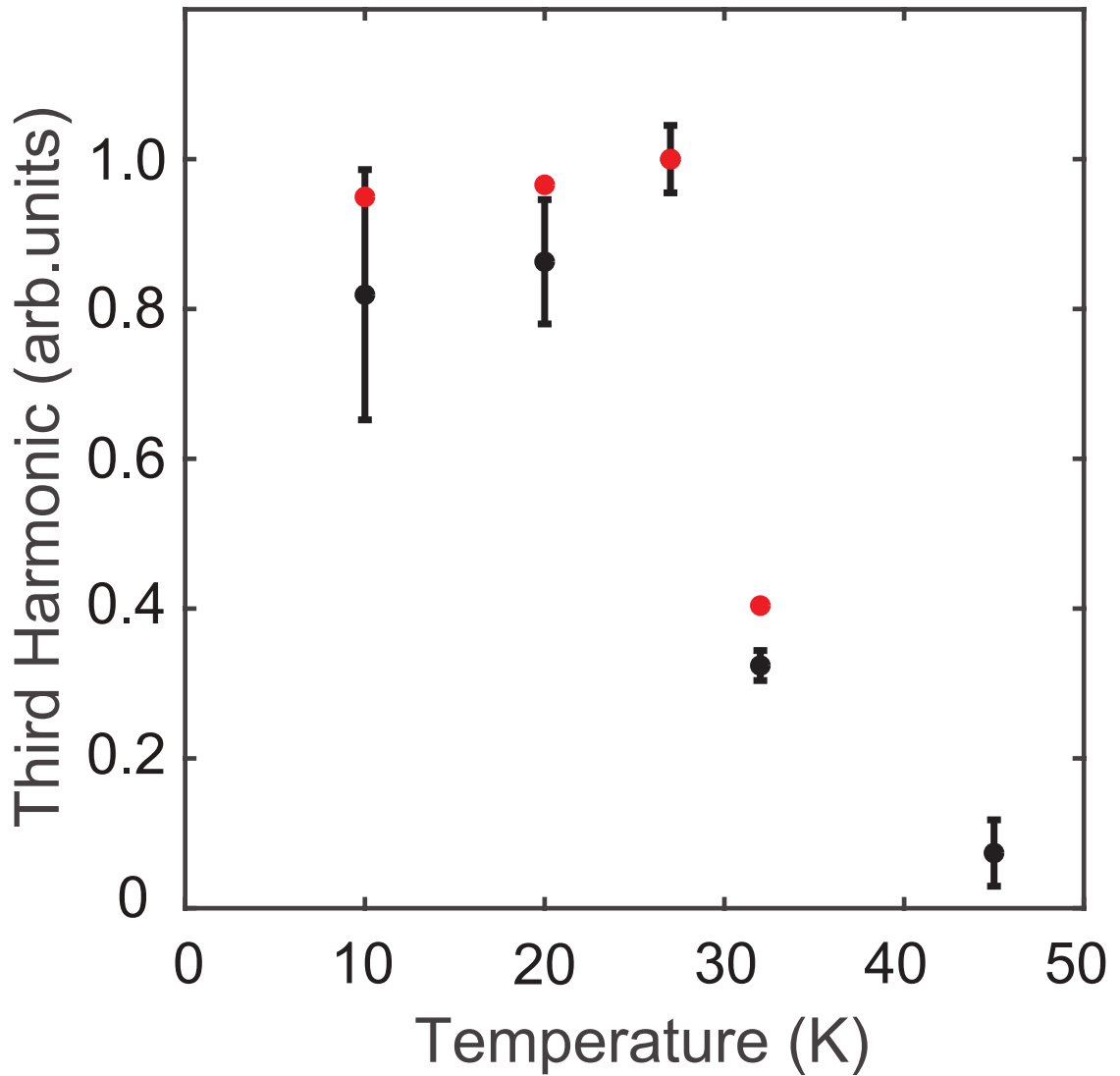
Figure 4.4: Magnitude of c-axis THG from LSCO versus temperature. All data points were taken with maximum field strengths of 80 kV/cm. The black circles are experimental data and the red circles are calculations as described in the text. The experimental data and calculations are normalized to the maximum value, which occurs at 27K in both experiment and simulation.

4.4 (black dots). Clearly, the signal does not solely scale with the superfluid density (which is directly proportional to the square of the JPM frequency), but instead decreases slightly for temperatures lower than 27K. Recent work has shown that detailed calculations are necessary to understand the temperature dependence of the third harmonic signal. Calculations based on this theory are plotted as red dots in Fig. 4[83]. The third harmonic signal is calculated from the nonlinear optical kernel of the Josephson phase, and its overlap with the spectral amplitude of the pump pulse, as shown in equation 4.5.

$$I^{NL}(\omega) = \int d(\omega')A(\omega - \omega')K(\omega')A^2(\omega')K \propto \frac{\omega_J^3 coth(\beta\omega_J/2)}{4\omega_J^2 - (\omega + i\gamma(T))^2} \qquad (4.5)$$

A is the spectral amplitude of the electric field profile and K is the nonlinear optical Kernel. This kernel does have an overall scaling with the superfluid density as ω_J^3. However, there is also a factor in the kernel, $coth(\beta\omega_J/2)$, that comes from the thermal excitation of plasmon modes, which causes third harmonic emission to increase with temperature [75]. The kernel also has a resonance at the Josephson plasma frequency. For our experiment, the pump pulse is centered at a frequency lower than the Josephson plasma frequency for all measured temperatures. However, with increasing temperature this process is closer to being on resonance since the condensate density (and hence ω_p) is reduced. Finally, quasiparticle damping increases with temperature, causing third harmonic emission to decrease. Thus, there are four competing factors that determine the overall temperature dependence of third harmonic emission due to Josephson plasma waves. These calculations capture the qualitative features of the data including a maximum in third harmonic emission at 27K, a decrease as the temperature is decreased, and a sharp decline in third harmonic emission in the vicinity of T_C.

The work in [75] and the results shown here motivate looking at the temperature dependence of third harmonic emission from other c-axis cuprates since the non-monotonic temperature dependence goes beyond basic Josephson-equations predictions. To our knowledge, third harmonic emission from c-axis cuprates has only been previously reported in $La_{2-x}Ba_xCuO_4$[74] and shares some similarities with our results. More detailed studies of third harmonic generation and THz nonlinearities have been performed in many superconductors, including cuprates,

focusing on light polarized in the ab-plane. The interpretation of the data has been in terms of the Higgs mode and quasiparticle contributions [70, 84, 85, 86, 63, 64]. We note that there is a prediction of contribution of plasma waves to the third harmonic generation for light polarized in the ab-plane [75]. The nonlinear THz response of cuprates can also be studied with pump-probe protocols, with [75] giving predictions for the response using the nonlinear optical kernel formalism. Experimentally, this pump-probe protocol has been used to study LBCO, where both amplification of Josephson Plasma Waves [39] and long-lived oscillations in the THz pump-probe signal [87] were observed.

4.6   Conclusion

We have explored the nonlinear c-axis response of LSCO and have observed THz third-harmonic generation arising from the Josephson plasma mode. The emission from the sample under intense THz radiation displays cubic behaviour indicative of third harmonic generation, which has been shown to be consistent with phase dynamics between the copper-oxygen planes in LSCO. An interesting future direction on the cuprates would be to investigate the relationship between the phase mode and amplitude mode and their potentially coupled contributions to the nonlinear terahertz response.

4.7   Acknowledgements

Chapter 5

THz Strong Coupling Between Metamaterials and Superconducting Josephson Plasmons

5.1 Abstract

The study and manipulation of quantum materials with light and cavities offers the tantalizing possibility to couple to and control macroscopic quantum phases. We investigate light-matter coupling with metamaterial resonator arrays (MRAs) placed on top of a c-axis oriented $La_{1.85}Sr_{0.15}Cu0_4$ single crystal to enable coupling with the Josephson Plasma Mode (JPM). Replaceable metamaterial tapes allow precision placement of MRAs from the LSCO surface: in the present study we compare the electrodynamic response for MRAs that are $\sim$200nm and $\sim$9μm from the LSCO surface. Measurements of THz reflectivity as a function of temperature show an edge-feature with the same behavior as the JPM but at a highly renormalized frequency. Measurements of the reflectivity for both samples reveal a renormalization of the JPM frequency, ω_{JPM}, from 1.7THz to $\sim$1THz at 10K. The observed shift is consistent with the appearance of a lower superconducting po-

lariton branch arising from strong electrodynamic coupling between the resonators and the JPM. With increasing temperature, the polariton redshifts as expected for decreasing superfluid density. The renormalization is larger for the 200nm sample and the temperature dependence tracks the JPM closer, consistent with stronger coupling. The response is modeled using both homogenized effective medium theory and as a multilayered system, and additionally with full-wave electromagnetic simulations. For the idealized effective medium description, the coupling of the resonators splits the JPM into upper and lower polaritons. However, the more realistic multilayer modeling shows that the upper polariton does not clearly manifest in the reflectivity, consistent with experiment. This establishes the lower polariton as the observable for light-matter coupling in layered metamaterial-cuprate samples. Our results demonstrate strong light-matter coupling as a step towards optimizing the ability to tune and manipulate superconductivity using terahertz cavity-based approaches.

5.2   Introduction

The use of light to study and manipulate materials has led to many interesting and important developments in the study of quantum materials, such as photoinduced phase transitions, tunable devices, and light-enhanced phases [4, 88, 89]. The incorporation of cavities with quantum materials has further enhanced the ability of researchers to couple light with the phases and collective modes of quantum materials [90]. The integration of cavities with quantum materials provides a potential route to modify ferroelectric phase transitions, enhance superconducting correlations, or induce topological switching [91, 92, 93, 94]. Integrating cavities with superconductors is a particularly intriguing possibility as it has been shown that cavities can be used to cool superconducting phase fluctuations, and calculations suggest that coupling strengths and field strengths necessary to accomplish this are achievable [93, 95, 96]. However, experimentally realizing cavities integrated with quantum materials is a challenging task, further complicated by the fact that cavities fabricated directly with quantum materials may require the
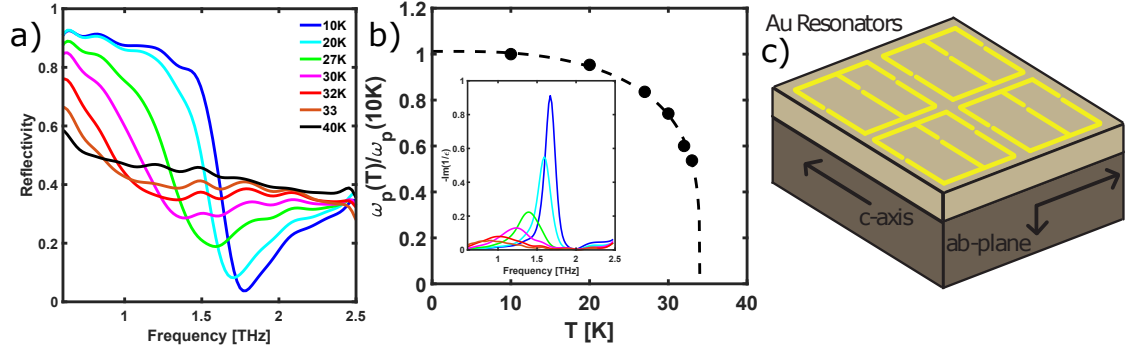
Figure 5.1: a) Reflectivity of LSCO crystal. b) JPM frequency vs. temperature normalized to the 10K value, inset: loss function extracted from LSCO reflectivity. c) Schematic of gold MM resonators in tape, placed on a c-axis oriented LSCO crystal.

growth of multiple samples to perform a frequency sweep of the cavity resonance to clarify or optimize the coupling.

In this work, we study the interaction between cavities and excitations in quantum materials by integrating metallic metamaterial resonators with a superconducting cuprate, coupling to the Josephson Plasma Mode (JPM) in the THz frequency range. There have been proposals to modify the superconducting state with cavity interactions, possibly changing the transition temperature [93, 37, 97, 98, 95, 96]. Essentially, through the parametric dependence of the cavity frequency on the superconducting phase degree of freedom, the coupling can be tuned to be quadratic in the phase. This allows the back-action of the cavity to decrease the damping rate of the phase, similar to cooling in opto-mechanical cavity systems[93, 95, 96, 99, 100, 101, 102]. A reduction in the damping rate essentially cools phase fluctuations, which can enhance superconductivity.

Superconducting cuprates are comprised of layers of quasi-2-d superconducting copper-oxygen planes. The c-axis is perpendicular to the planes [36]. In the normal state ($T > T_c$, where T_c is the superconducting transition temperature), cuprates are insulating along the c-axis. However, in the superconducting state transport along the c-axis arises from tunneling of Cooper pairs between Cu-O planes. The tunneling is described by the Josephson equations (as described in Chapter 1), where the current is directly related to the order parameter phase

difference between the two layers, which can be modified by an electric field [73]. The c-axis plasma frequency associated with this transport is the JPM, and it manifests in the reflectivity as a plasma edge. For example, the reflectivity of the $La_{1.85}Sr_{0.15}Cu0_4$ (LSCO) single crystal studied here is shown in figure 5.1a. Given that the JPM is a plasma frequency, it is a longitudinal excitation and shows up as a peak in the loss function (defined as $-1/Im(\epsilon)$), as shown in the inset of figure 5.1b. The JPM frequency is proportional to the square root of the superfluid density. Thus, as the sample is cooled further into the superconducting state, the plasma edge blueshifts to higher frequencies, following the superconducting order parameter, as shown in figure 5.1b. For many cuprates, the JPM lies in the THz regime, and is often used as a probe of superconducting correlations, including in nonequilibrium experiments [89, 103]. The LSCO sample studied here has a JPM of 1.7 THz at 10K, which is at the peak of the loss function shown in the inset of figure 5.1b. To study the interaction of this longitudinal electromagnetic feature with a cavity, we have directly placed metamaterial resonators on top of the LSCO as depicted schematically in 5.1c.

To investigate the coupling of the JPM to cavity-like resonances, we use metallic metamaterial (MM) resonators. Metamaterials are periodic sub-wavelength structures where the resonance is controlled by the shape and geometry of the structures[104]. Instead of fabricating the metamaterials directly onto the surface of the single crystal, the gold structures are fabricated as free-standing polyimide tapes, and then placed on the surface of a c-axis oriented LSCO single crystal, as shown schematically in figure 5.1c. The total thickness of the polyimide tapes is $9.4 \mu m$, and the position of the resonators within the tape can be controlled, thereby changing the distance between the resonators and the LSCO crystal surface. The metamaterial consists of two asymmetric E-shaped gold split ring resonators, with geometric parameters labelled in 5.2c, and a microscope image of the array is shown in 5.2b. Full-wave electromagnetic simulations of the transmission of the bare tape (not on LSCO), along with experimentally measured transmission is shown in figure 5.2a, along with calculated transmission of the tape modelled with a dielectric function with two lorentzian oscillators. The surface currents for the
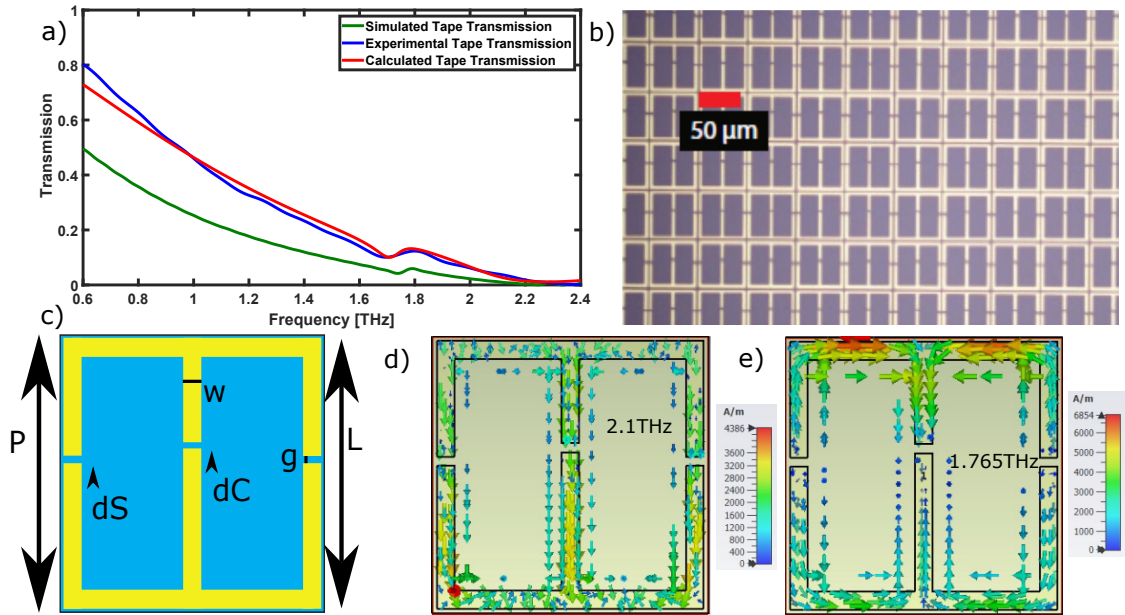
Figure 5.2: a) Simulated (green), Experimentally measured (blue), and modelled with 2 lorentzian oscillators (red) metamaterial tape transmission. b) Microscope image of a portion of the metamaterial array, with red scale of $50\mu m$. c) Single MM unit cell, with parameters shown by arrows and black bars. The metamaterial parameters are as follows: total periodicity P=$61\mu m$, gold bar length L=$59\mu m$, bar width w=$4\mu m$, gap value g=$2\mu m$, center gap offset dC=$6\mu m$, side gap offset dS=$3\mu m$. Simulated surface currents at d) dipole resonance frequency of 2.1THz and e) asymmetric resonance frequency of 1.765THz, simulated with full-wave electromagnetic simulations.

two modes of the metamaterial, at 2.1THz and 1.765THz are shown in figure 5.2d and 5.2e, respectively. The 2.1THz mode is the dipole mode of the metamaterial, characterized by currents in each of the dipole bars flowing parallel to each other. When placed on the LSCO crystal, the dipole bars are parallel to the c-axis, as is the incident THz electric field. The simulations and experimental measurement of the bare tape are also this same orientation. The small feature at 1.765 THz mode is the asymmetric mode of the metamaterial, as can be seen by the out-of-phase relationship of the currents both between parallel bars and between the 2 asymmetric "E" shaped split ring resonators. The metamaterial is modeled using a 2-Lorentzian model for each resonance, given by the following equation:

$$\epsilon(\omega) = \epsilon_{pol} + \frac{F_1}{\omega_{MM1}^2 - \omega^2 - i\omega\gamma_{MM1}} + \frac{F_2}{\omega_{MM2}^2 - \omega^2 - i\omega\gamma_{MM2}} \qquad (5.1)$$

In this equation, ϵ_{poly} is the polyimide dielectric constant, F_1, ω_{MM1} and γ_{MM1} are the oscillator strength, resonant frequency and damping of the dipole resonance, and F_2, ω_{MM2} and γ_{MM2} are the oscillator strength, resonant frequency and damping of the asymmetric resonance. To be specific, the resonant frequencies stated here are the transverse frequencies for the two metamaterial resonances. The parameters in the 2-Lorentzian models are given in table 5.1. The dipole resonance has a large oscillator strength and large damping, giving the broad downward slope in the transmission in figure 5.2a. This is consistent with a previously reported metamaterial structure of a similar 2 "E"-shaped split ring resonator geometry [105]. The asymmetric resonance is much sharper with much weaker oscillator strength, it gives the peak-dip feature in the THz transmission at ~1.75THz in figure 5.2a. Similar sharp modes in metamaterial split ring resonator structures have been seen when symmetries are broken by moving the gaps in a resonator to different points along the bars [106]. In this case the gaps in the resonators are displaced by a distance dS=3μm on the side bars of the resonator and a distance dC=6μm from the center of the gold bars, as shown by the arrows on the metamaterial unit cell in figure 5.2c.

The primary goal of this chapter is to investigate the electrodynamic response of metamaterial resonator arrays (MRAs) integrated with the c-axis cuprate $La_{1.85}Sr_{0.15}CuO_4$ (LSCO) with a view towards cavity augmented superconductivity. We first provide two methods to analytically model the response of the coupled resonator-JPM system, highlighting the key similarities and differences. Full-wave simulations of the MRA on LSCo will be presented later along with the experimental data in figure 5.5. Specifically, the response is modeled using homogenized effective medium theory and as a multilayered a system. The effective medium description highlights that coupling of the JPM with the metamaterial resonators leads to polaritonic coupling, with upper and lower branches being evident. However, more realistic multilayer modeling shows that the upper polariton does not clearly manifest in the reflectivity. This is consistent with experimental measurements of the THz reflectivity as a function of temperature within the superconducting state. We investigate the terahertz response for arrays that are placed $\sim$200nm and $\sim$9μm from the LSCO surface, and both samples reveal a renormalization of the JPM frequency, ω_{JPM}, from 1.7 THz to 1.1 THz at 10K. The observed shift is consistent with the appearance of the lower superconducting polariton branch arising from strong electrodynamic coupling between the resonators and the JPM. With increasing temperature, the polariton redshifts as expected for a decreasing superfluid density. The temperature dependence for the 200nm sample is more pronounced, consistent with stronger coupling. The present results build upon our previous work showing the coupling between a metamaterial resonance and the JPM in LSCO [82]. In this work, the improved fabrication of the MRAs enables changing the resonator array - LSCO surface spacing. The coupling between the MRAs and the LSCO is much stronger for 200nm spacing in comparison to 9μm. We note that the present results can be explained using electromagnetic coupling and there is no evidence of cavity-based modification of the microscopic parameters that determine the superconducting response of LSCO. Nonetheless, our results demonstrate strong light-matter coupling as a step towards optimizing the ability to tune and manipulate superconductivity using terahertz cavity-based approaches.

Table 5.1: Table of MM oscillator parameters for MRA.

ω_{MM1} [THz]	γ_{MM1} [THz]	F_1 [THz^2]	ω_{MM2} [THz]	γ_{MM2} [THz]	F_2 [THz]
2.2	0.45	28	1.71	0.1	1.25

5.3 Materials and Methods

The metamaterial tapes were fabricated with conventional surface-micromachining. First, the polyimide film (PI-2600 series, HD MicroSystems) was coated onto a silicon wafer at a specified thickness. The polyimide thin film was then cured using rapid thermal annealing (RTA) in nitrogen. The ramp up speed is 3 ℃/min and is held at 350 ℃ for 30 minutes. For the thinner polyimide layers (i.e., 200nm) the thicker film was etched with reactive ion etching (RIE) with an etching rate of 150nm/min with 10sccm CF4 and 40 sccm O2 under 200mTorr and 300W plasma environment. Then the gold metamaterial structures were defined through photolithography and lift-off processes. A second polyimide film was coated on top of the metamaterial structures followed by the same curing process described above. Finally, the polyimide film was peeled off from the silicon substrate. The metamaterial tapes were mounted onto the LSCO surface with the dipole bars pointing along the c-axis of the LSCO crystal.

THz measurements were performed in an evacuated, home-built vacuum box. The THz was generated using a portion of the output of a 1KHz, 6W laser system with a ZnTe crystal. After reflecting from the sample surface, the THz was measured using electro-optic sampling (EOS) in another ZnTe crystal with an 800 nm gate beam. A gold mirror was used as the reference. The LSCO crystal was mounted onto a continuous flow cryostat and cooled with liquid helium. The ZnTe generation and detection crystals are in the vacuum chamber thereby eliminating drift issues associate with water vapor. The LSCO crystal was cut to expose the a-c plane and has a doping of approximately 15%, with a JPM of 1.67THz, agreeing with previous measurements [36].

5.4 Results

Before presenting the experimental results, we first investigate electromagnetic coupling between the metamaterials and the c-axis superconducting response using a simple analytical effective medium analysis and an analytical multilayered model. Full-wave electromagnetic simulations will be shown in figure 5.5. This is important to interpret features that can appear in the reflectivity, which serves as a baseline in the search for cavity-based modifications of superconductivity. In the simplest approach, the integrated MRA-LSCO sample is treated as a single-medium material with a frequency dependent dielectric response comprised of a Drude response for the LSCO JPM and Lorentzian oscillators for the metamaterial resonances [36]. This single-medium model has the following dielectric function:

$$\epsilon(\omega) = f\left(\epsilon_{LSCO} - \frac{\omega_j^2}{\omega^2 + i\omega\gamma}\right) + (1-f)\left(\epsilon_{pol} + \frac{F_1}{\omega_{MM1}^2 - \omega^2 - i\omega\gamma_{MM1}}\right.$$
$$\left. + \frac{F_2}{\omega_{MM2}^2 - \omega^2 - i\omega\gamma_{MM2}} \right) \quad (5.2)$$

where f is the volume fraction for the LSCO, ϵ_{LSCO} is the dielectric background of LSCO, ω_j is the JPM frequency, γ is an effective damping for the LSCO capturing the effects of quasiparticles, and the rightmost term in the brackets is equation 5.1 with the same terms, which is the metamaterial resonator contribution to the dielectric function. The Drude component for the LSCO portion of the dielectric function is shown in equation 5.2 for clarity. However, for the calculation of the reflectivity of the MRA structure, the dielectric function extracted from the experimental reflectivity of LSCO in figure 5.1a is used. The oscillator strength of the metamaterial resonances $F_{1,2}$ is referred to as the coupling strength as it is directly related to the shift of the effective JPM response (i.e. lower polariton), as will be shown below. The reflectivity calculated from 5.2 for the $9\mu m$ LSCO-MM is shown in figure 5.3a, which exhibits edges in reflectivity both above and below the bare LSCO JPM frequency (see figure 5.1a, ω_{jpm} 1.67 THz at 10K). Both features redshift with increasing temperature, tracking the JPM which is proportional to the square root of the superfluid density.

However, it should be noted that the analytically calculated 40K reflectivity (black curve of 5.3a), where the LSCO is characterized by a dielectric response of $\epsilon \sim 27$, also shows an upper edge in reflectivity. This directly comes from the dipole resonance of the metamaterial. More insight is gained by looking at the calculated loss function, $-im(1/\epsilon)$, for equation 5.3, shown in figure 5.3b. Starting with the black curve, the loss function has two peaks at 2.06 and 1.47THz, these are the longitudinal frequencies of the two oscillators when the tape is placed onto LSCO, with the higher frequency, larger peak being the dipole resonance and the smaller, lower frequency that of the asymmetric resonance. It should be made clear that these modes of the metamaterial are transverse, however they do still have a longitudinal frequency associated with them. Additionally, when the tape is placed on the LSCO at 40K, both the transverse and longitudinal frequencies are redshifted compared to the bare tape (comparing the MRA parameters in table 5.1 and the last line of table 5.2). These two peaks are present even without the JPM response that is only present below the LSCO superconducting T_c. This response at 40K can be directly compared with the calculation at 10K, where the loss function has peak at 2.25, 1.48, and 1.1THz. The two upper peaks that were present at 40K are also present at 10K, but both at higher frequencies than 40K (the upper peak has a larger shift of $\sim$200GHz, compared to the minimal shift of the other peak). There is also a lower peak in the loss function that is not present at 40K. The bare LSCO loss function at 10K is peaked at $\sim$1.7THz, and there is no clear peak in the loss function there. From this it can be seen that the coupling between the JPM and MM resonances has two effects. First, the JPM is highly renormalized and corresponds to the lower polariton. For 10K this is at 1.1THz, corresponding to a shift of $\sim$30% from the bare JPM frequency. Second, the upper peak of the loss function is shifted to higher frequencies, although it is also present without the JPM. These two peaks are essentially the upper and lower polaritons generated by the coupling between the MRA and the JPM. The temperature dependence of the loss-function peaks (the polariton frequencies) can then be seen as a redshift of both peaks as temperature is increased, consistent with the decrease in JPM frequency as temperature is increased. This shows that

metamaterial-JPM coupling splits the JPM into upper and lower superconducting-polaritons (SCP), both with JPM characteristics.

It should also be noted that the loss function peaks correspond to longitudinal frequencies of the coupled system, illustrating that SCPs are longitudinal modes, as is the JPM. The loss function is dominated by the peaks at the frequencies of the upper and lower SCPs, arising from coupling induced splitting of the bare LSCO loss function (see inset, Fig. 5.1b). This coupling and shift of the longitudinal frequencies MRA-JPM coupling is analogous to the shifts observed from longitudinal optical phonon-plasmon coupling in doped semiconductors [107, 108, 109, 110] when the the doping is such that the plasma frequency is proximal to the optical phonon. For MRA-JPM coupling, the tuning results from temperature tuning of the condensate density.

The parameters used in the calculation are shown in table 5.2. The parameters of the tape are not taken to be the same as the bare tape (table 5.1), but are instead varied to match the lower polariton frequency and peak-dip feature to the experimental reflectivity (shown below). This is to take into account the dielectric frequency shift of the resonances when placed on top of LSCO, which has $\epsilon \sim 27$. That is, local increase of the dielectric constant will cause a redshift of the resonances compared to the isolated bare tape. Here the resonance frequency of the dipole resonance shifts from 2.2THz for the bare tape to 1.8THz when the tape is placed on the LSCO with resonators $9\mu m$ from the LSCO surface. The asymmetric resonance shifts from a value of 1.71THz for the bare tape to 1.44THz on the LSCO below T_c. Additionally, near-field coupling will also cause shifts to the resonances. Specifically, interlayer capacitance and inductance when metallic resonators are brought close to a metallic surface (which LSCO is in the superconducting state) will also lead to redshifts of the metamaterial resonances[111]. Looking at the resonator parameters in table 5.2, we can see that for all temperatures the resonators are redshifted compared to the bare tape values (table 5.1). It should however be noted that even if all resonator parameters are kept constant, either to the bare tape value or to fit the lower polariton frequency of the experimental data at 10K, the same qualitative behavior of the polariton is still present. The results of these
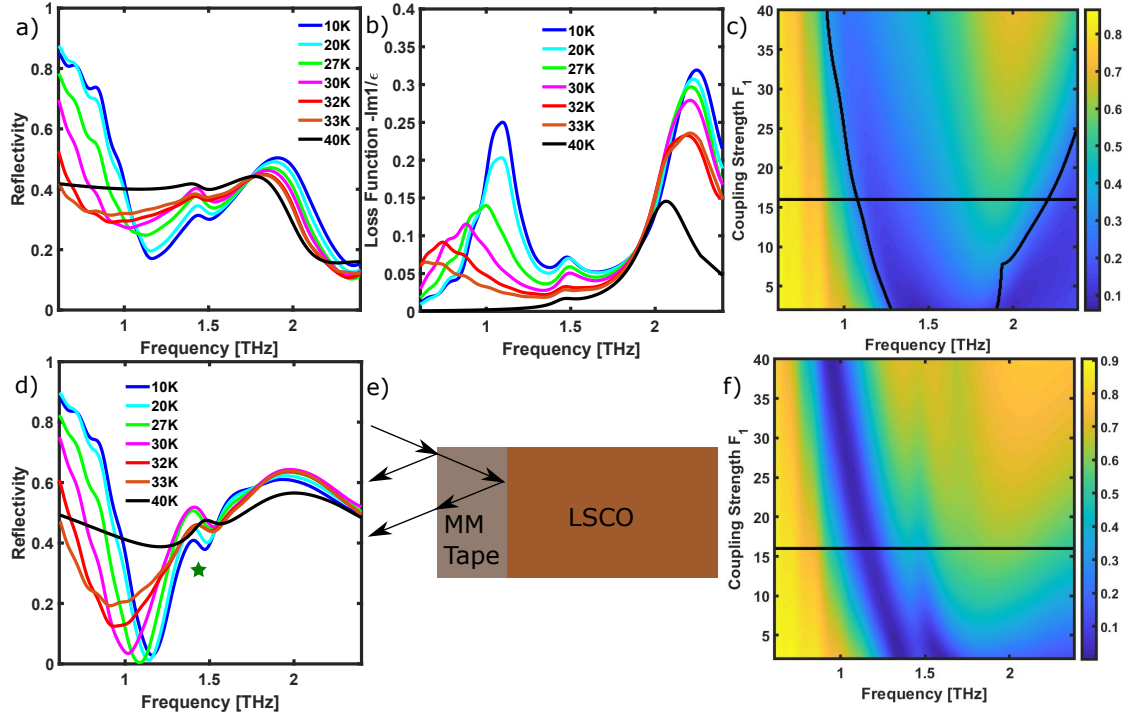
Figure 5.3: a-b) Effective medium theory calculation of reflectivity (a) and loss function (b) as a function of temperature, using dielectric function of equation 5.2, LSCO parameters extracted from the bare crystal reflectivity, and MRA parameters in table 5.2. c) 2-d color plot of reflectivity calculated using the dielectric function in equation 5.2 as a function of coupling strength F_1 for 10K LSCO. d) Calculation of reflectivity as a function of temperature using the multilayered interference theory model. e) Schematic of interference theory model, where MM-tape is modelled as a film on top of bulk LSCO. f) 2-d color plot of reflectivity calculated using multilayered interference theory model as a function of coupling strength F_1 for 10K LSCO.

Table 5.2: Table of MM oscillator parameters for $9\mu m$ MRA.

T	$\omega_1[THz]$	$\gamma_1[THz]$	$F_1[THz^2]$	$\omega_2[THz]$	$\gamma_1[THz]$	$F_2[THz]$
10	1.8	0.35	16	1.44	0.15	1.25
20	1.8	0.35	16	1.44	0.15	1.7
27	1.8	0.35	16	1.44	0.15	2.1
30	1.8	0.35	16	1.44	0.15	2.5
32	1.8	0.35	16	1.44	0.15	1.25
33	1.8	0.35	16	1.44	0.15	1.25
40	1.8	0.55	16	1.47	0.15	1.25

calculations are shown in figure 5.4.

Using equation 5.2, it is also possible to calculate the loss function $(-Im(1/\epsilon(\omega))$ as shown in figure 5.3b. Peaks in the loss function correspond to zeros of the real part of the dielectric function, illustrating that the superconducting polaritons are longitudinal modes as is the JPM. The loss function is dominated by the peaks at the frequencies of the upper and lower SCPs, arising from coupling induced splitting of the bare LSCO loss function (see inset, Fig. 5.1b). This coupling and shift of the longitudinal frequencies MRA-JPM coupling is analogous to the shifts observed from longitudinal optical phonon-plasmon coupling in doped semiconductors [107, 108, 109, 110] when the the doping is such that the plasma frequency is proximal to the optical phonon. For MRA-JPM coupling, the tuning results from temperature tuning of the condensate density.

To further clarify the electrodynamic response, the reflectivity calculated as a function of F_1 is shown in Fig. 5.3c. The previously shown calculated reflectivity establishes the lower polariton manifesting as an edge in reflectivity and as the lower peak in the loss function. The lower polariton tracks the JPM temperature dependence and is only present when the JPM is present (the lower polariton is absent at 40K). Reflectivity calcualted as a funciton of MM dipole oscillator strength further demonstrate it is coupling with the MM resonator that splits the lower polariton from the bare JPM. The black lines in figure 5.3e track the upper and lower peaks of the calculated loss function. With increasing F_1, the splitting between the upper and lower reflectivity edges increases as expected for strong
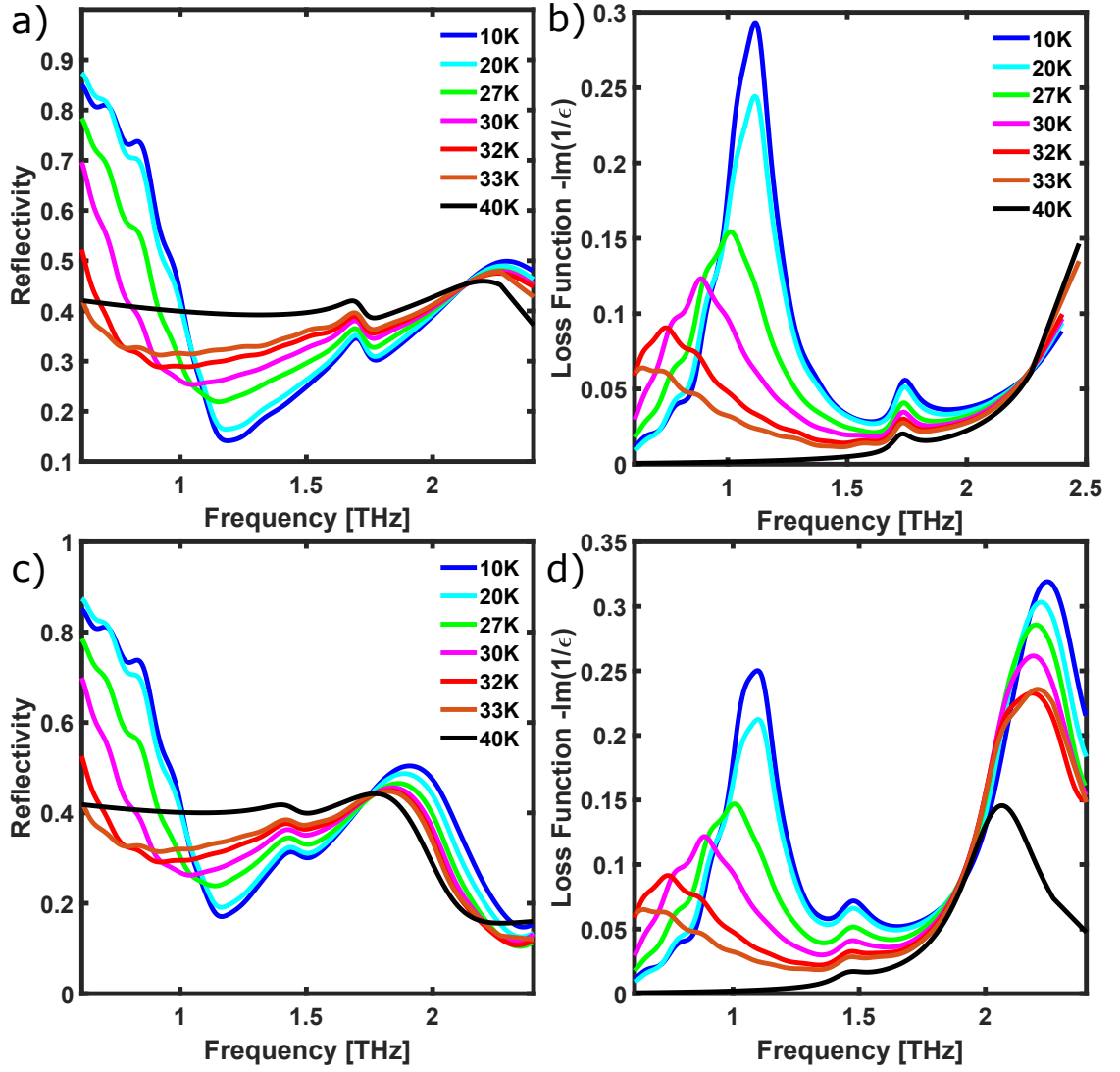
Figure 5.4: Analytically modelled reflectivity for LSCO-MM keeping oscillator parameters constant with temperature. a-b) Effective medium theory calculation of reflectivity (a) and loss function (b) as a function of temperature, keeping the MRA parameters constant with temperature, using the bare tape parameters in table 5.1. The lower edge in reflectivity and lower peak in loss function are still present and follow JPM temperature dependence. The upper peak is beyond 2.5THz, the measurement bandwidth used in THz experiments. c-d) Effective medium theory calculation of reflectivity (c) and loss function (d) as a function of temperature, keeping the MRA parameters constant with temperature, using the 10K $9\mu m$ tape parameters in the first line of table 5.2. The lower edge in reflectivity and both lower and upper peaks in loss function are still present and follow JPR temperature dependence.

light-matter coupling. This further clarifies that oscillator-JPM coupling yields longitudinal upper and lower polaritons where the magnitude of the splitting is largely determined influenced by F_1. The horizontal black curve is the value of F_1 that matches the frequency of the reflectivity minimum in figure 5.3d to the minimum in the experimental reflectivity, which will be shown in figure 5.5f. It is also true that the strength of the asymmetric resonance, F_2 also determines the lower polariton frequency as it is also coupled to the JPM. However, since it has a much smaller oscillator strength, it's effect on the lower SCP is not as strong as the dipole resonance, so we have focused on that here.

In the absence of this analysis, it could be tempting to relate the coupling induced redshift of the lower polariton (at a given temperature, compared to the bare ω_{JPM}) to a modification of the condensate density (as occurs for the bare JPM with temperature). However, this analysis shows that the renormalization of the polariton compared to the bare JPM is from the electromagnetic coupling of the JPM to the metamaterials oscillators and the resultant change of the zero-crossing of the effective dielectric function, and does not arise from any weakening of the superconductivity or oscillator induced change of the superfluid density. This is an important result that highlights that any actual modification of the condensate will have to be disentangled from the electrodynamics that arise from polaritonic coupling. For example, a modification of the condensate density would manifest as a clear change of the superconducting transition temperature. We note that figure 5.3 a) – c) was presented to provide some insight into the coupling. However, it is a severe approximation, so we next consider an analytical multilayer model which will more accurately capture the MRA-JPM coupling.

We now present realistic analytical calculations treating MRAs as a layer on top of the c-axis LSCO as in the experiment (see Fig. 5.3e). To be specific, the MRA is taken as a $9.4 \mu m$ thick planar array of lorentzian oscillators on top of the bulk LSCO, with the following dielectric function in equation 5.1. The reflectivity is then analytically calculated using the following Fresnel equations for the multilayered system, which includes multiple reflections inside of the MRA (but not in the thick LSCO crystal).

$$r = \frac{r_{air,MM} + r_{MM,LSCO}e^{i2\delta}}{1 + r_{air,MM} * r_{MM,LSCO}e^{i2\delta}} \tag{5.3}$$

$$\delta = 2\pi d\sqrt{\epsilon_{MM}}\omega/c \tag{5.4}$$

where $r_{air,MM}$ and $r_{MM,LSCO}$ are the Fresnel reflection coefficients for the air-MM and MM-LSCO interfaces respectively, d is the thickness of the MRA, and c is the speed of light. As previously mentioned, the MRA oscillator parameters when the MRA is placed on the LSCO crystal are varied to match the frequencies of key features in the analytically calculated reflectivity with the experiment, which will be shown in figure 5.5. Specifically the lower polariton frequency and the peak-dip feature related to the asymmetric resonance, which will be shown below. The results of this interference theory calculation for reflectivity as a function of temperature are shown in 5.3d. There is a clear reflectivity edge that redshifts with increasing temperature consistent with the effective medium model and the associated lower polariton peak. At 10K this is at 1.15THz, redshifed by 550GHz from the bare JPM frequency. Additionally there is a peak-dip feature whose frequency is nearly temperature independent at ∼1.5THz, as indicated by a green star in figure 5.3d. This feature is at the transverse frequency of the asymmetric resonance, ω_{MM1}. However, the reflectivity edge with similar temperature dependence corresponding to the upper polariton is much broader, and doesn't show the same clear temperature dependence as the effective medium model in Fig. 5.3a. Finally, Fig. 5.3f shows the calculated reflectivity for the layered model as a function of coupling strength F_1, where the effective lower polariton edge shifts to lower frequencies compared to the bare JPM as the coupling strength is increased. This is the dark blue curve in the 2d plot in Fig. 5.3f that shifts from ∼1.4THz to 1THz as F_1 is increased. The black horizontal curve is the value of the coupling strength F_1 that gives the same lower polariton frequency as seen in experiment, which will be discussed next. However, as the coupling strength is increased the upper edge in reflectivity broadens and becomes ill-defined. This is in contrast to the effective medium calculation, where the upper polariton is also seen as a

sharp edge splitting from the lower polariton. In short, these calculations reveal that the lower reflectivity edge corresponds to the lower polariton and serves as the observable for the coupling in this MRA-LSCO structure. Additionally, for the multilayered calculation, a calculated loss function is not shown as the model is not characterized by a single dielectric function, thus making the extraction of a single loss function invalid.

With the understanding afforded by the simulations and analysis above, We now turn to the experimental data, shown in figure 5.5. For comparison, the reflectivity of the bare LSCO crystal is replotted in Fig. 5.5a,d. The JPM-edge redshifts with increasing temperature as the superfluid density decreases. The data is also shown as a 2-d color plot, and the JPM-edge can be seen as the change from the gold (high-reflectivity) to the blue (low reflectivity). The JPM frequency corresponds to the reflectivity edge. That is, the change between high and low reflectivity which is explicitly marked by a black curve (same fit as in Fig. 5.1b for clarity). The order parameter behavior can be seen as the gold wedge-like feature of high reflectivity, which becomes smaller as temperature is increased (going up the y-axis).

The experimental reflectivity for the MMTP with the metamaterial array 200 nm from the LSCO surface is shown in Fig. 5.5b,e. A similar edge in the reflectivity (1.1 THz at 10K) is evident and redshifts with increasing temperature as does the bare JPM. From the discussion and analysis associated with Fig. 5.3, it is clear that this is the lower superconducting polariton (SCP). The SCP edge is at a highly renormalized frequency compared to the bare JPM. For example, at 10K, the bare JPM frequency is 1.7 THz while the SCP is at 1.1 THz. This is a shift of ∼30% of the bare JPM frequency. Some of the reflectivity curves of the LSCO-MM samples exhibit R slightly larger than 1 at low frequencies, attributed to imperfect referencing. The reflectivity shown here is normalized to one for the highest value measured. The trend with temperature is again captured in the 2-d plot of reflectivity shown in 5.5b. Similar to the bare crystal the reflectivity edge shows the change from high reflectivity to low reflectivity as a function of frequency, and this maps a gold wedge-like feature in the 2-d plot. However for the

MM-LSCO sample this reflectivity edge is at a highly redshifted frequency, and the gold region of high reflectivity, although showing similar temperature dependence (along the y-axis), is much smaller. Finally, the reflectivity of Fig. 5.5e has a local maximum at ∼1.6THz, decreasing gradually at higher frequencies. This is related to the dipole resonance, as seen in the multilayer reflectivity calculated in Fig. 5.3d. It should be noted, however, that this maximum in the reflectivity is very broad and is also present at 40K (black curve of Fig. 5.5e). The frequency of the dipole resonance is however clearly shifted compared to the bare tape. The dipole resonance has a transverse frequency of 2.2THz for the bare tape versus 1.6THz when the resonators are 200nm from the LSCO surface. However, the resonance is very broad and this maximum in the reflectivity does not have the strong temperature dependence that the lower polariton has. This is also captured by the analytical calculations of figure 5.3d. Thus the observation of the lower-polariton edge feature at a highly renormalized frequency compared to the bare JPM is the experimental signature of strong light-matter coupling in this system.

Figure 5.5c,f shows the experimental reflectivity for the LSCO-MM sample with the metamaterial array $9\mu m$ from the LSCO surface. The lower SCP is again clearly evident and exhibits the same redshift with increasing temperature. It should be noted that the distance between the metamaterial structures and the LSCO surface is varied by a factor of ∼40 between the ∼$9\mu m$ and 200nm tapes. Even when the oscillators are further away the demonstration of coupling to the JPM is evident from the shifting of polariton with temperature and the renormalized reflectivity edge (∼1.2 THz at 10K). As with the 200nm spacing, the upper polariton is very broad without a strong temperature dependence, in accordance with the analytical multilayer calculations in 5.3d. The $9\mu m$ reflectivity also clearly shows the peak-dip feature of the asymmetric resonance, at ∼1.45THz for all temperatures below T_c. The feature is also at a slightly but noticeably higher frequency at 40K compared to all temperatures below T_c. This is indicative that not only is there a shift of the resonance due to the dielectric constant of LSCO, which is present at 40K, but also near-field coupling (interlayer capacitance and inductance), which will be most relevant when the LSCO has a metallic response,
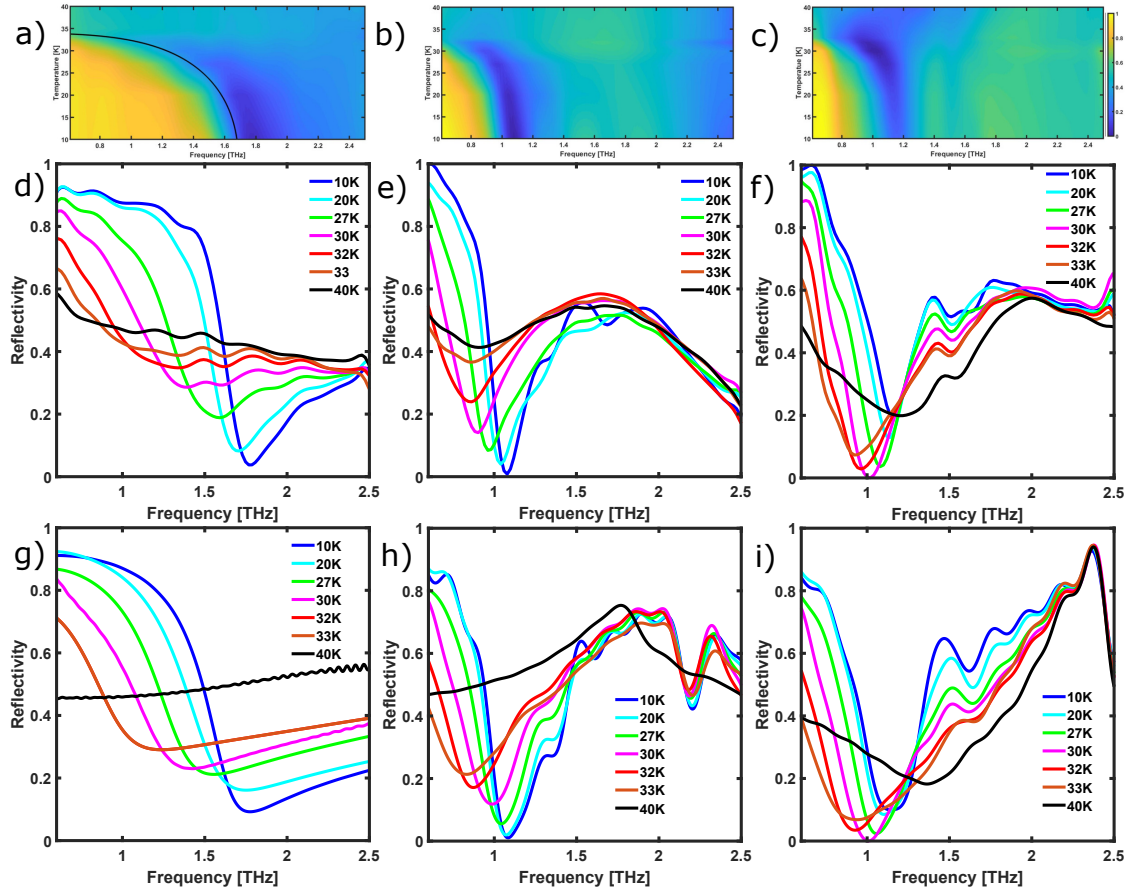
Figure 5.5: Experimental results and full-wave simulations for LSCO-MM reflectivity. a-c) 2-d color plot to show trends of experimental THz reflectivity as a function of temperature for a) bare LSCO crystal, b) 200nm MM-tape on LSCO and c) $9\mu m$ MM-tape on LSCO. d-f) Individual experimental reflectivity curves for d) bare LSCO crystal, e) 200nm MM-tape on LSCO and f) $9\mu m$ MM-tape on LSCO. g-i) Full-wave simulation results for reflectivity of g) bare LSCO crystal, g) 200nm MM-tape on LSCO and i) $9\mu m$ MM-tape on LSCO.

in the superconducting state[?].

The previously shown analytical models of the LSCO-MM system are helpful in creating intuition for the JPM-MRA coupling, but they are phenomenological in nature. In addition to this, full-wave electromagnetic simulations of the LSCO-MM samples were performed. The gold resonator geometry of the MRA is shown in figure 5.2c, with its structural parameters. One unit cell of the resonator in a $9.4\mu m$ thick polyimide film places on top of bulk LSCO was then simulated with full-wave electromagnetic simulations. The LSCO dielectric function used was extracted from the experimental reflectivity in figure 5.1a. The full-wave simulation results are shown in figure 5.5g-i. First, the simulated bare crystal reflectivity is shown in figure 5.5g. Full-wave simulations of the LSCO-MM samples for the 200nm and $9\mu m$ MRAs are shown in panels h and i, respectively. Figure 5.5h captures the qualitative features of the 200nm experimental data, namely the lower polariton that redshifts with increasing temperature, the weak feature of the asymmetric resonance, and a broad hump at higher frequencies. The simulations of the $9\mu m$ reflectivity in panel i also show the lower polariton feature and the asymmetric resonance, except for at 40K. Both the 200nm and $9\mu m$ simulations do have an additional sharp dip in the reflectivity, at 2.25THz for the 200nm sample and slightly above 2.5THz for the $9\mu m$ sample that is not present in the experiment. It should be noted that inhomogeneous broadening due spatial variations in the metamaterial parameters can cause features in the experimental reflectivity to broaden compared to the simulations, which use a perfect periodic array based on identical unit cells. The full-wave simulations also match the trends with temperature of how deep the reflectivity minimum of the lower polariton is, for the 200nm sample the reflectivity minimum is deepest at 10K and increases with increasing temperature. On the other hand the $9\mu m$ sample has the lowest reflectivity minimum at 30K, with the minimum less deep for both higher and lower temperatures.

The experimental data and full-wave simulations show some clear similarities between the 200nm and $9\mu m$ LSCO-MM samples. Both show the lower polariton with JPM-like temperature dependence, and the broad feature at higher frequencies. The lower polariton is at lower frequencies for the 200nm sample, indicative of

Table 5.3: Table of MM oscillator parameters for $200nm$ MRA.

T	$\omega_1[THz]$	$\gamma_1[THz]$	$F_1[THz^2]$	$\omega_2[THz]$	$\gamma_1[THz]$	$F_2[THz]$
10	1.6	0.4	15	1.3	0.2	1.5
20	1.6	0.4	15	1.2	0.25	1.7
27	1.475	0.4	15	1.1	0.35	1.35
30	1.475	0.4	15	1.05	0.35	1.35
32	1.475	0.4	15	1.05	0.35	1.25
33	1.475	0.4	12	1.05	0.35	1.35
40	1.425	0.4	10	1.05	0.35	0.5

stronger coupling compared to the $9\mu m$ sample. There are however some qualitative differences in their behavior, specifically looking at the asymmetric mode. The peak-dip feature associated with the asymmetric mode can be seen at $\sim$1.45THz in the experimental reflectivity of figure 5.5f. This frequency of this feature is temperature independent for all measured temperatures below T_c. This is in contrast to the 200nm data, which does show some of this peak-dip feature as a shoulder in the 10K reflectivity at 1.3THz. This feature is still slightly present, but noticeably weaker and at a slightly lower frequency for the 20K reflectivity in figure 5.5e. This feature can be captured in both the effective medium and multilayer modelling of the reflectivity as well by a change in the frequency of the asymmetric resonance frequency (the sharp, small oscillator strength resonance). The results of these analytical calculations, to match the behavior of the asymmetric resonance for the 200nm sample, are shown in figure 5.6. As a reminder, the previous analytical calcualtions in figure 5.3 are for parameters to match the behavior of the $9\mu m$ sample. The MRA oscillator parameters are shown in table 5.3. It should be noted that both the dipole and asymmetric resonances are redshifted not only compared to the bare tape, but also the $9\mu m$ MRA parameters in table 5.2. This is not unexpected since the gold resonators are closer to the LSCO surface for the 200nm MRA sample, which would increase both the dielectric shift and near-field coupling of the resonators with the LSCO surface.
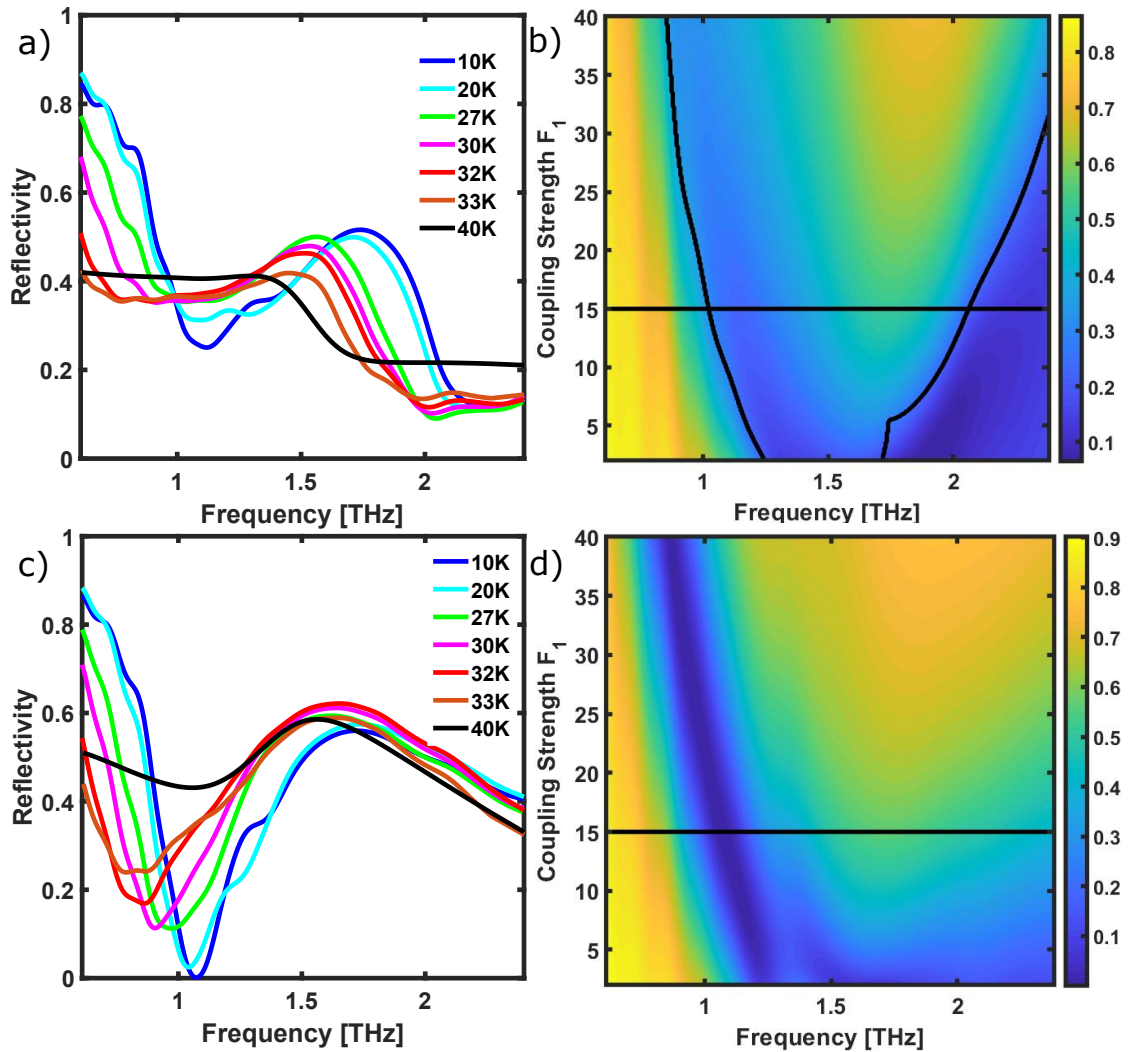
Figure 5.6: Reflectivity Calculations for 200nm LSCO-MM Parameters. a) Single-medium reflectivity as a function of temperature calculated using equation 5.2 with parameters in table 5.3. b) 2-d color plot of Single-medium reflectivity as a function of dipole oscillator strength F_1. c) Multilayer reflectivity as a function of temperature calculated using equation 5.3 with parameters in table 5.3 for the MRA. d) 2-d color plot of Multilayer reflectivity as a function of dipole oscillator strength F_1.

5.5 Conclusion

The modeling presented above shows that very large shifts to the effective longitudinal response of the SC-MM system can be achieved with classical electromagnetic coupling. Although it does not correspond to a fundamental change to the quantum phase, such as a change to the superfluid density or critical temperature, achieving this does prime the system in the desired direction towards modification of superconductivity. It could be possible to explain the shift of resonances using a quantum model, such as in [93], however it should be noted that simply using optical measurements such as reflectivity do not necessitate a quantum model, and it is classical electromagnetic calculations that are able to explain the large splitting seen in the resonances in reflectivity. This demonstrates that although a large Rabi-splitting is indicative of strong or ultra-strong light matter coupling, a change to the properties of the quantum phase or other non-classical-electromagentic effects such as radiative transitions or vacuum Bloch-Siegert Shift are needed to show effects of vacuum fluctuations or quantum coupling is achieved[112, 113].

In this work the interaction between MM structures and the JPM in LSCO was investigated with THz reflection spectroscopy. Measurements as a function of temperature and modelling of the response both demonstrate coupling between the JPM and MM resonances. Models were developed to explain how the lower SCP seen in reflectivity is fully indicative of the strong coupling of the system, and that the edges in reflectivity show a shift to the longitudinal excitations of the system. By looking at MM-tape systems, which allow the MM-LSCO distance to be varied, stronger coupling was acheived when the gold MM resonators were closer to the LSCO surface, 200nm compared to $9\mu m$. This work experimentally demonstrates coupling between a cavity-like MM resonance and the collective mode of a quantum material, and identifies the observables for coupling in this kind of system. It also shows the ability to have a light-matter-cavity type system using a replaceable metamaterial tape as the cavity system, allowing multiple cavity-resonator-structures to be used with the same single-crystal sample. Further work and design optimization could result in stronger coupling thereby modify the superconducting state, or realizing some of the nontrivial, nonlinear light-matter

coupling effects [19-20]. However, considerable care will be required to extract true modification of the quantum phase from electrodynamic coupling.

5.6   Acknowledgements

Chapter 6

Photoinduced Insulator-to-Metal Transition in Ca$_2$RuO$_4$ Thin Films

6.1 Introduction

Transition metal oxides host a wide variety of quantum phases, and many of these, such as Mott insulators, superconductivity, orbital order, and exotic magnetism, manifest in the ruthenates [17]. Ultrafast pump-probe techniques give new ways to study these phases, as well as control them[4]. Calcium ruthenate Ca$_2$RuO$_4$ is an example of a material of interest due to the sensitivity the insulating state has to external stimuli, orbital order and its relation to Sr$_2$RuO$_4$, a non-cuprate transition metal oxide superconductor [114]. Previous ultrafast measurements on this material have studied orbital transitions, Keldysh-crossover physics, and quadrupolar order [115, 116, 117]. However, all of these experiments have been at fluence and temperature regimes away from the insulator-to-metal transition (IMT), which occurs at ∼357K for bulk crystals [18, 19]. This transition occurs along with a structural transition, and when the transition is cycled many times for a sample, structural defects form and damage the sample [20]. This makes ultrafast studies of the IMT difficult, as the photoinduced IMT can also drive the material through the structural transition. One way that this material can be made more stable to cycling through the transition is to grow it as a thin film on a substrate [118].

Ca_2RuO_4 (CRO) grown on $LaAlO_3$ (LAO) has an insulator-to-metal transition at 220K, lower than in bulk crystals, and an antiferromagnetic transition at 150K, higher than the bulk crystal transition at 110K [118, 18, 26, 119].

In addition to gaining insight into Ca_2RuO_4, this material is another platform to study first-order photoinduced IMT dynamics. Previous studies on the photoinduced IMT in VO_2, V_2O_3, and $NdNiO_3$ have shown manifestations of the first-order nature of the phase transition in their dynamics. In particular, the percolation of a new phase in the background of another [120, 11]. However there are distinct differences in the dynamics of these materials, and Ca_2RuO_4 is another material that has distinct dynamics from these, adding to the library of strongly-correlated IMTs that have been studied with ultrafast techniques [120, 11, 121].

In this work, we study the photoinduced IMT in Ca_2RuO_4 by performing 800nm-pump, THz probe measurements. We study thin films of Ca_2RuO_4 grown on LAO over a range of temperatures below the IMT temperature, focusing on high-fluence measurements where the film is driven through the IMT by the pump. They measured dynamics include relatively fast switching into the metallic state, followed by relaxation back into the insulating state indicative of nucleation and growth of insulating domains, a hallmark of a first-order phase transition.

6.2   Methods and Sample

The sample studied here is a 25-nm thin film of Ca_2RuO_4 grown on $LaAlO_3$. It has an insulator-to-metal transition between 200-220K, which corresponds to a drop in resistivity with hysteresis, indicative of a first-order phase transition. Along with the change from insulator to metal, the transition also involves a structural transition that preserves the PBCA symmetry, from a short c-axis (S-PBCA) structure to a long c-axis (L-PBCA) structure, as measured with x-ray diffraction [18].

THz is an ideal probe for how metallic a sample is, as it involves very low energy scales, as close as is possible to measuring DC-like conductivity on ultrafast timescales. Here we measure optical-pump, THz probe dynamics using 100fs,
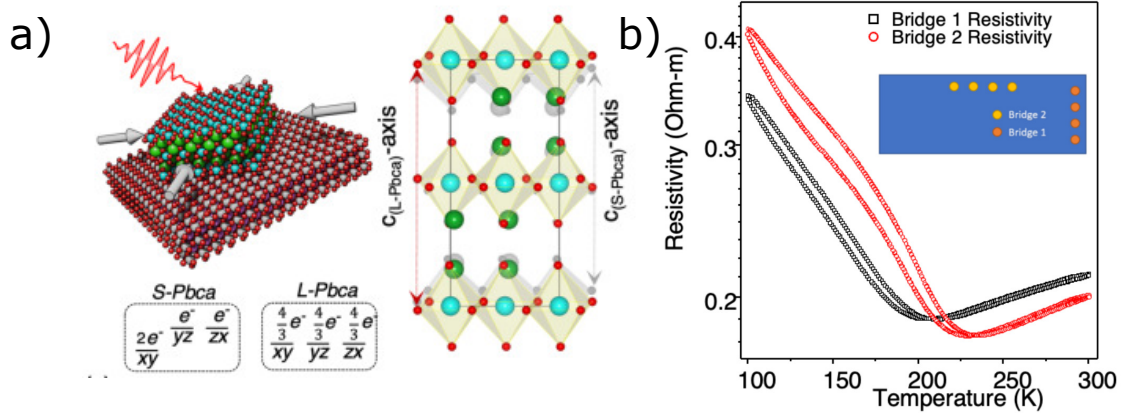
Figure 6.1: From [27] a) Schematic crystal structure of Ca_2RuO_4, as well as orbital configuration in the insulating short c-axis (S-PBCA) phase and long c-axis (L-PBCA) phase. b) Resistance of Ca_2RuO_4 sample measured with two different orientations and spots on the sample. T_{IMT} is the minimum in resistance, occurring at 200K for bridge 1 and 220K for bridge 2.

800nm pump pulses, and THz probe pulses generated via optical rectification in ZnTe, with a bandwidth of 1-10meV. The experiment is performed in a reflection geometry, with a continuous flow cryostat cooled with liquid nitrogen in a vacuum THz box. The THz gate pulse and 800nm pump pulse are each on their own delay stage, so that they can be moved independently, giving the ability to measure THz "1d scans" where the gate is fixed and the pump is varied, and to do 2-d "spectroscopy scans" where the gate-pump time is kept fixed and the THz is scanned, so look at changes to the reflected THz pulse over the whole probe bandwidth at fixed pump time.

6.3 Dynamics

We can first examine in detail the OPTP dynamics at a representative temperature far below the transition (T_{IMT}) pumped with high fluence. Figure 6.2a shows a 1-d pump-probe scan at a base temperature of 130K with an 800nm pump fluence of $11.6mJ/cm^2$. The dynamics exhibit three distinct regimes, colored red, green, and blue in fig 6.2a. First, there is a rapid, $\sim 8ps$ rise, shown in red. This relatively fast rise in the reflectivity can be understood as the destruction of the insulating

state by the pump, driving the sample area into the higher-temperature, metallic phase. We note that the measure rise time is longer than the time-resolution of the OPTP experiment is (as compared to measurements of GaAs on the same system). This fast rise in the signal and quenching of the insulating state can already be compared to some similar insulator-to-metal transition compounds. For example, VO_2 has a rise time of hundreds of picoseconds. This can be understood as the rise time being limited by the speed at which metallic regions can nucleate and grow in the background insulating state. On the other hand, $NdNiO_3$, another IMT compound, shows a $\sim 1ps$ rise time, faster than Ca_2RuO_4. This timescale in $NdNiO_3$ is on the order of that of electron-phonon thermalization. So in total for the initial rise of the signal, Ca_2RuO_4 sits closer to $NdNiO_3$, so the quench of the insulating state does not appear to be limited by nucleation and growth of metallic domains.

After the initial rise, there is a second, $\sim$100ps rise time, shown in green in fig 6.2a. This long rise in the signal can be associated with the pump causing the sample temperature to overshoot T_{IMT}, where the conductivity is highest, and relaxing back towards T_{IMT}. If the pump fluence is high enough, not only can the insulating state be fully quenched, but the temperature after the initial rise will be higher than the IMT temperature. As can be seen in figure 6.1b, as temperature is increased above T_{IMT}, the resistance increases. This is consistent with the fact that the scattering rate in metals generally increases with increasing temperature, decreasing the conductivity. After being pumped to a temperature above T_{IMT}, the sample will relax back to the lower equilibrium temperature (for example as energy diffuses out of the pump spot) leading to an increase in conductivity and a corresponding rise in the reflectivity.

The final part of the dynamics, shown in blue, is the decay of the signal back towards zero. This occurs with a timescale of hundreds of picoseconds, but is best contextualized looking at a fit of the dynamics, which is shown in figure 6.2b. The fit here is given by the following equation:

$$\Delta E/E = \frac{1}{e^{-t/t_r}+1}(A_1 - A_2(e^{-t/t_1}-1))e^{-(t-t_d)/t_2} \tag{6.1}$$

The first term of this is the initial rise of the signal, with t_r as the rise time, which has a fit value of 1ps. The amplitudes of the ensuing dynamics are given by A_1 and A_2, whose values are both kept positive here while their signs in 6.1 are opposite. It should be noted in this form, a positive coefficient with an exponential corresponds to a decay of the signal $(+A_1)$ while a negative coefficient $(-A_2)$ corresponds to a rise of the signal. From this we can see that t_1 corresponds to the longer rise of the signal, which for this temperature and fluence is $\sim 60ps$. Finally, the decay of the signal is captured by the final term $e^{-(t-t_d)/t_2}$. Here t_d is the time at which the signal is peaked, which following the previous discussion is when the sample reaches T_{IMT}. After this it decays with a rate of t_2, which for this temperature and fluence is $\sim 323ps$. At t_d, the relaxation of the sample is not only a decrease in temperature, but also a change in phase, where insulating domains grow out of the metallic state, creating an inhomgenous state, since the IMT in Ca_2RuO_4 is first order. Similar work on $NdNiO_3$ has shown that relaxation dynamics are well captured by the Avrami model, which describes nucleation and growth a new phase in a background of a different phase following a rapid quench. The Avrami model has been used to successfully describe the dynamics of nucleation and growth of the metallic phase in the equilibrium insulating background in VO_2 and of nucleation and grown of insulating domains growing in the metallic background during the relaxation of $NdNiO_3$. The Avrami equation for nucleation and growth of a new phase is given by the following.

$$f(t) = 1 - e^{-Kt^n} \tag{6.2}$$

where f is the fraction of the new phase, K is the growth rate of the phase, and n is the Avrami exponent. An Avrami exponent of $n = 1$ is associated with diffusion-limited growth, while $n = 2$ is associated with interface limited growth[122]. The decay dynamics in $NdNiO_3$ are best fit with a decay of the form $e^{-((t-t_d)/t_2)^2}$, with a corresponding Avrami exponent of 2, consistent with interface limited growth. In contrast, the dynamics of Ca_2RuO_4 are best fit by a decay of the form $e^{-((t-t_d)/t_2)}$, corresponding to an Avrami exponent of 1 which corresponds to diffusion-limited growth.
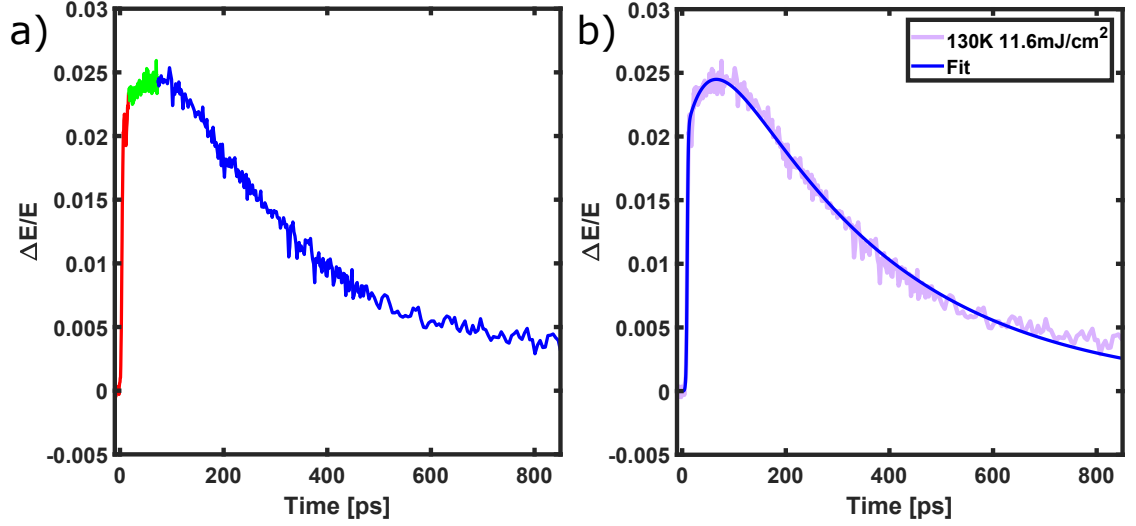
Figure 6.2: OPTP 1d scan of Ca_2RuO_4 thin film on LAO at 130K with $11.6mJ/cm^2$ fluence. a) $\Delta E/E$ data color coded to show different regimes of the dynamics, as explained in the text. b) Pump probe data along with a fit to equation 6.1 in the text.

6.4   Fluence Dependence

The previous interpretation can be further examined by looking at the fluence dependence of the dynamics. Figure 6.3 shows the 1-d scans for a range of fluences for six different temperatures. The low fluence dynamics (at all temperautures except 200K) exhibits a simpler form than described above, consisting of a fast rise and single exponential decay. This can be interpreted as the dynamics that occur when the fluence is well below the fluence threshold to drive the full IMT (i.e. the pumped sample temperature does not go above T_{IMT}). As the fluence is increased the non-trivial dynamics described in the previous section start to emerge. For example, the dynamics at 130K shows single exponential dynamics for 3.4 and $5.8mJ/cm^2$, while starting at 6.9 and $8.1mJ/cm^2$ a bump during the relaxation $\sim 50ps$ into the decay starts to emerge. This is consistent with some fraction of the pumped sample area being driven above the transition temperature. Thus, the long-rise is present in addition to the decay of energy out of the pumped area. At the higher fluences of 9.2-$11.6mJ/cm^2$ the long rise time associated with overshooting the transition temperature, where conductivity is maximum, can be
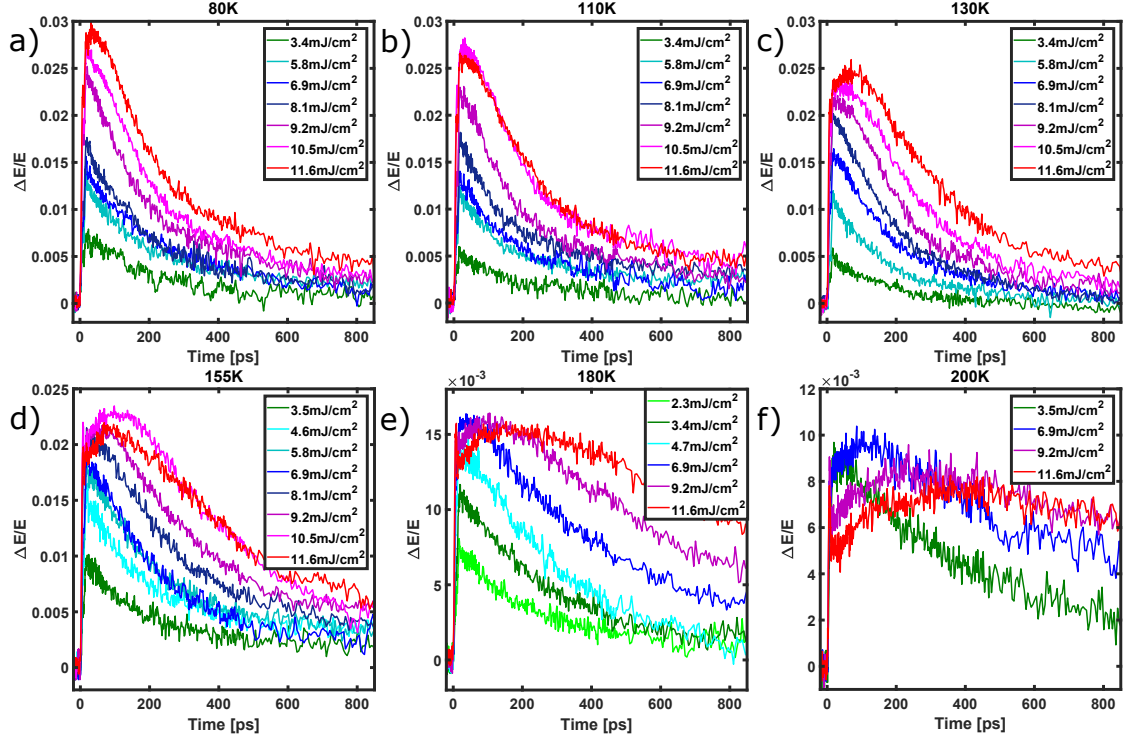
Figure 6.3: OPTP 1d scans for a range of fluences for a) 80K, b) 110K, c) 130K, d) 155K, e) 180K, and f) 200K

seen.

As described above, the long-rise time is associated with overshooting T_{IMT}. Thus, it is clear that with increasing fluence, this rise-time should increase (i.e., it will take longer to cool back to T_{IMT}. This is evident for the 130K, 155K, 180K, and 200K scans. For example the 180K data has the local maximum of the signal at $\sim 50ps$ for $6.9mJ/cm^2$, $\sim 150ps$ for $9.2mJ/cm^2$, and $\sim 200ps$ for $11.6mJ/cm^2$. For 80K and 110K the long rise time is only fully present at the highest fluences used. However, the clear bump in the exponential decay indicative of some of the pumped area being driven through the transition is present for both of these temperatures.

6.5 Temperature Dependence

The interpretation of the dynamics in terms of driving through and overshooting the insulator-to-metal transition and observing the decay back through the transition also has a clear prediction for the temperature dependence. As the base sample temperature is raised (keeping fluence constant) the long rise time of the sample will increase, since the same amount of energy will get the sample to a higher final temperature. Direct comparisons of a wide range of temperatures for two fluences are shown in figure 6.4. Looking at figure 6.4a, the higher fluence, we can see a clear increase in the long rise time of the sample as temperature is increased.

In addition to this relationship between sample temperature and rise time, there is another clear observation that can be seen with the temperature dependence of the $10.5mJ/cm^2$ data. As the temperature is raised the maximum of the signal, which is the maximum increase in reflectivity during the scan, shows a clear decrease. This is consistent with the base conductivity having an increase over a broad temperature range below the transition temperature. Based on the pump probe signal, 80K and 120K are nearly the same in magnitude, indicating that the conductivity has at least somewhat saturated to it's low-temperature value. Based on the above interpretation of the results, the maximum of the photoinduced reflectivity change is when the sample is at the IMT transition temperature. The maximum of the photoinduced reflectivity change decreasing at higher base temperatures is consistent with a significant increase in the equilibrium conductivity of the sample with temperature. Signatures of this have been seen, for example in VO_2 [120], although only over a very narrow temperature range, (within $\sim 15^o$ of the transition temperature). In Ca_2RuO_4 on the other hand, this decrease in the maximum conductivity increase exists for $\sim 100K$ below the transition. This is also reflected in the equilibrium DC conductivity as well (inverse of resistivity in Fig. 2.4b). The existence of finite conductivity over a broad temperature range below the transition temperature is likely related to disorder in the sample. Specifically, the substrate $LaAlO_3$ generally hosts twin domains in crystal samples. Since the structure of the Ca_2RuO_4 is tied to that of the substrate, it also inherits

the nano and mesoscale domain texture of the substrate. Direct measurements of conductivity with the spatial resolution to look at the spatial configuration of conductivity in this material at temperatures below the transition have only been performed on doped single crystals [123], and insulator-metal phase coexistence is only observed over a narrow temperature range (∼5K). Spatially resolved measurements of the c-axis lattice parameters have however been performed on Ca_2RuO_4 on $LaAlO_3$ [124]. Domains of long-and short c-axis were observed down to 100K, and as described in the introduction and figure 2.4 the insulator to metal transition in the electronic configuration is accompanied by a structural transition from one with a short c-axis to a long c-axis [124]. It should be noted however that this is not a direct measurement of the metallic and insulating volume fractions since this is a measurement of the lattice parameters, but they are indicative and consistent with finite conductivity at temperatures far below the transition temperature.

6.6 Conclusion

In summary, we have studied the photoinduced insulator-to-metal transition in Ca_2RuO_4 with 800nm-pump, THz probe spectroscopy. We observe a fast (but not resolution limited) ∼10ps switch into the metallic state, followed by a longer rise in the reflectivity increase associated with cooling back to the maximum in conductivity at T_{IMT}. The relaxation back into the insulating state is well captured by a fit to the dynamics based on the Avrami model with diffusion limited growth. This interpretation of the dynamics is corroborated by the fluence and temperature dependence of the dynamics. The decrease of the maximum reflectivity increase with increasing temperature also indicates finite conductivity over a wide temperature range, ∼100K below the transition, which is not observed over such a wide range in similar materials, such as VO_2, V_2O_3, and $NdNiO_3$ [120, 121, 11]. The ability to study the photoinduced IMT in Ca_2RuO_4 is enabled by studying a thin-film. Our work serves as another manifestation of nucleation and growth dynamics in a photoinduced insulator-to-metal transition, as well as characterizing the switching speed and relaxation on ultrafast timescales, which are necessary for
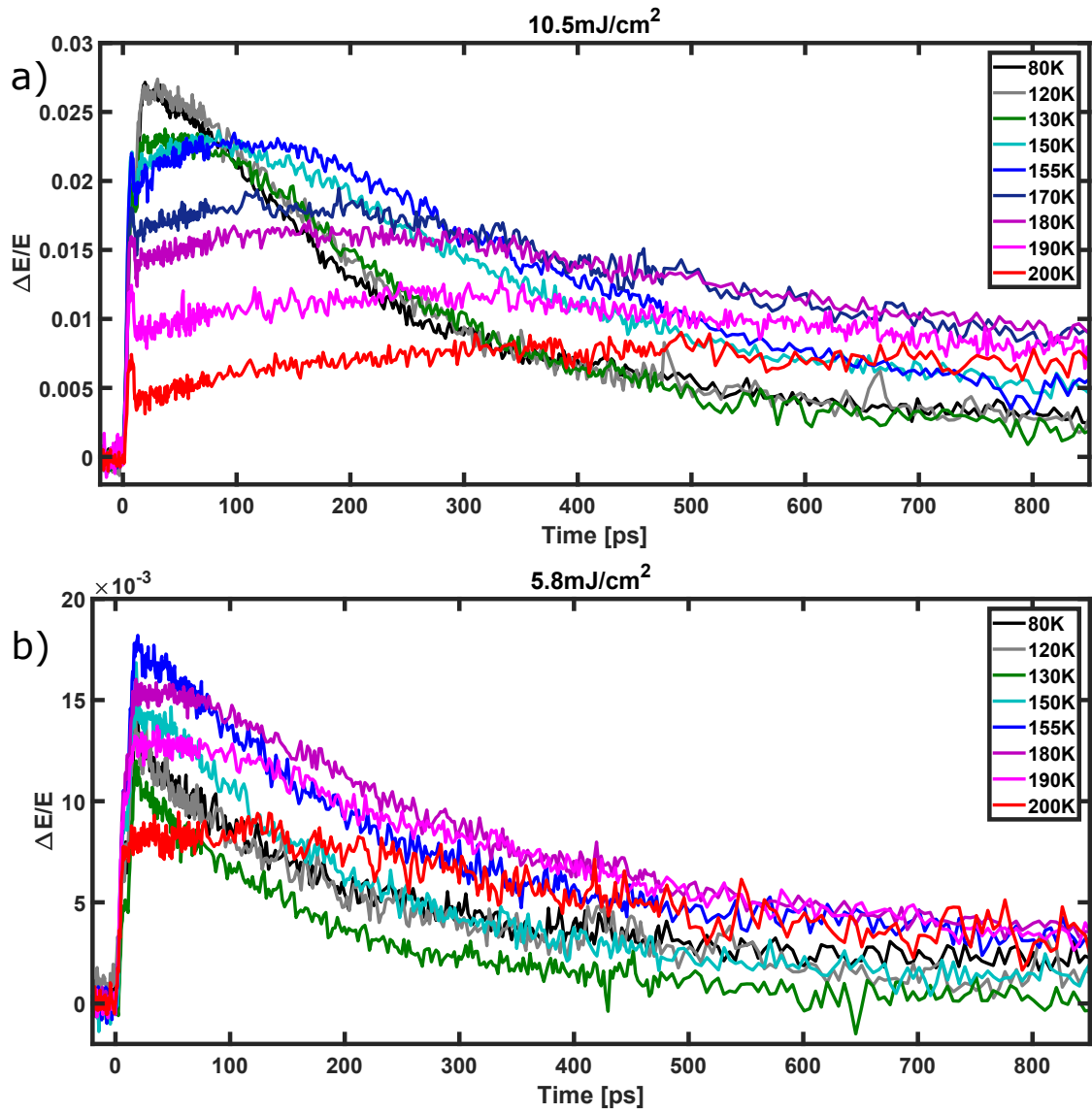
Figure 6.4: OPTP 1d scans for a range of temperatures for fluences of a)$10.5mJ/cm^2$ and b)$5.8mJ/cm^2$

fast computing and electronic switching applications. Additionally, the study of the photoinduced IMT with optical pump is the first step to ultrafast studies of this material's IMT, which up to now has been avoided in other studies due to sample instability [20, 115, 116, 117]. Recent work on Ca_2RuO_4 on $LaAlO_3$ using optical pump, x-ray diffraction probe, has established some signatures of a non-thermal state when pumped with intense optical pulses [27]. Specifically, this experiment focused on a Bragg peak that was sensitive to the c-axis lattice parameter and pumped it with fluences up to $50mJ/cm^2$. First, the rise time of the pump-probe diffraction signal is faster than the THz signal, indicating that the lattice actually changes faster than the increase in metallicity. Second, The c-axis lattice constant and intensity of the photoinduced state do not follow that of equilibrium measurements. Specifically, the growth of the c-axis in the photoinduced state (which does occur during the structural transition that occurs along with the IMT) is larger than what is measured in equilibrium for the given increase in intensity of the Bragg peak. The combination of the time resolved x-ray and THz measurements show that for a very short time early in the dynamics the sample undergoes structural changes before the electronic transition has been driven. However even at longer times, when the sample is in the photoinduced metallic state, the c-axis still does not follow the equilibrium structural parameters. Further measurements could work to gain more complete information of both the electronic and structural properties of the photoinduced state, as well as look into other ways of driving this transition, such as with lower frequency pump pulses.

6.7   Acknowledgements

Chapter 7

Conclusion and Future Directions

I will first discuss future directions for the three lines of research outlined in chapters 4-6 of this thesis. Instead of repeating the conclusions reached for each of the projects completed in this thesis, I will give an overall conclusion to the sum of research completed in this thesis.

The THz high-harmonic generation on LSCO project joins the growing set of THz nonlinear optics experiments on cuprates in the last decade. Up to now, these results are generally interpreted as purely being related to the Josephson phase mode when measuring parallel to the c-axis of cuprates or purely in terms of the Higgs mode when measuring in the *ab*-plane of cuprates [70]. Although there are no suggestions that the measured c-axis response in our LSCO crystal has any contributions from the Higgs mode, the theory that explains the non-monotonic temperature dependence of the third harmonic generation does suggest that the Josephson phase mode can contribute to THz high-harmonic generation when measuring in the ab plane [75]. This suggests re-examining the purely Higgs-mode interpretation of some previous experiments[70, 84, 68, 125]. Of specific interest is that some third harmonic generation is observed at temperatures above the superconducting critical temperature[70, 84, 68, 125]. This was suggested to be related to signs of the Higgs mode in a fluctuating superconducting state above T_c. However, careful optical conductivity measurements [126] along with the mentioned theory suggest that a fluctuating superconducting state above T_c can have contributions to third harmonic generation from the phase mode [75]. The point is that

the phase mode is likely a relevant contribution to THz high-harmonic generation both when examining c-axis crystals and ab-plane thin films. A future experiment that would be helpful would be to perform THz third-harmonic generation experiments on an ab-plane oriented sample where the JPM can be seen. This being possible is contrary to what is expected in thin-film cuprate samples, since the JPM is a result of Josephson tunneling along the c-axis. However, previous experiments on a thallium based cuprate have shown suggestions of seeing the JPM in a thin film sample [127, 128, 129], so high-field THz experiments are a natural experiment to perform here.

The LSCO-MM has demonstrated coupling between the JPM and a MM resonance, and there are some natural follow up experiments. A straightforward line of research to follow up with is improved metamaterial-unit cell designs in the tape geometry to shift the Josephson plasmon polariton even further from the bare crystal JPM value. However, it should be noted that by the calculations shown in Fig. 5.3d, the tape geometry, where a layer of oscillators are placed on top of a bulk single crystal, will always obscure the upper polariton. In order to see a more straightforward splitting of the JPM into upper and lower polaritons, a different geometry from the tape-on-crystal must be devised. Some MM-cavity designs have been previously proposed [93] although they are difficult to fabricate. It is also true that one of the main overall goals of coupling the JPM to a MM or cavity resonance is to use this to control superconductivity, specifically to raise the critical temperature. The measurements reported here do not show a change in T_c, so this is still a goal to worthy of additional investigation. It could be that strong coupling strengths are needed to achieve this, or that the MM/cavity resonance must be tuned to a different frequency with respect to the JPM than the reported experiment (e.g. the low JPM values when LSCO is near T_c). It could also be the case that the LSCO-MM sample needs to be driven with high-intensity THz light, as that is a method where calculations of cavity coupling have been proposed to be able to strengthen superconductivity [93].

The Ca_2RuO_4 project has demonstrated first-order phase transition dynamics in the photoinduced phase transition, and is the first ultrafast study of the pho-

toinduced phase transition in this material. Other previous studies on Ca_2RuO_4 have had to work in temperature and fluence regimes to avoid this transition since it causes the crystals to fracture and break apart. Now that the photoinduced phase transition has been established through direct absorption of optical light, which has a straightforward interpretation of ultrafast heating of the sample, the next line of research would be to look at other frequencies of light to induce the insulator-to-metal transition. Specifically mid-IR and THz light enable access to phonons, and have also been thought of in a tunneling Keldysh framework to generate carriers in Ca_2RuO_4, so the affect these have on a photoinduced insulator to metal transition can give additional insight into Ca_2RuO_4 and these excitation mechanisms. Additionally, other aspects of the first order nature of the insulator to metal transition can be optimally probed with THz. Specifically, a project I worked on in a minor role in during this thesis was looking at the effect the inhomogeneous state that VO_2 has during it's insulator to metal transition has on a THz metamaterial resonance [12]. Specifically, a large positive increase in the background THz dielectric constant is needed to explain the observed redshift of the THz resonance. Although this is interesting, it is true that it occurs over a very narrow 2K temperature range in VO_2. The ultrafast measurements in this thesis suggest that some remnants of metallic conductivity survive for $\sim 100K$ below the transition temperature. This indicates that this large increase to the dielectric function could manifest over a much wider temperature range in Ca_2RuO_4 than in VO_2. This motivates THz metamaterial experiments with Ca_2RuO_4.

In total, this thesis shows three examples of using time-resolved THz techniques to gain insight into some of the ordered phases of transition metal oxides, further setting the stage for their control with light and at ultrafast timescales. All three of these projects also very specifically benefit from the use of THz light, as opposed to working in another frequency range. For LSCO, the JPM varies from 1.7THz down to 0 within the superconducting state, so both looking at JPM nonlinearities and light-matter coupling with the JPM requires working in the THz regime. Additionally, for Ca_2RuO_4, THz light is the frequency range closest to DC that can be utilized for ultrafast measurements, so it is the most unambiguous probe of the

ultrafast insulator-to-metal transition. These highlight how the field of ultrafast studies of quantum materials has reached the maturity where the correct pump and correct probe can be chosen for a given experiment, instead of being wholly limited by what can be generated in the lab. There is certainly still progress to be made, particularly in generating pump pulses that can span the entire THz range to as high of field strengths needed [43, 44, 45, 46, 130, 131, 132, 133], along with probing schemes that cover as many types of material excitations as possible.

It should also be noted that the youngest experimental area explored in this thesis is the coupling of metamaterials with excitations in quantum materials, and there is a huge set of possibilities for the possible benefits of the incorporation of quantum materials with metamaterials and cavities. Some key experiments have already demonstrated the ability of metamaterials to enhance our ability to pump materials, both to drive photoinduced phase transitions [61] and enhance optical nonlinearities such as high harmonic generation [134, 135]. The sensing power of metamaterials can additionally improve our ability to probe the optical properties of quantum materials [12, 136, 137]. Finally, and perhaps most importantly, there is a growing body of theoretical literature studying the tantalizing possibility of the modification of material properties by increasing their coupling strength to light [138, 139, 90, 93, 37, 140, 141, 142, 143, 144, 145, 146, 147, 148, 149, 150, 151, 152, 153, 154, 155, 156]. Here experiments are still working on catching up, particularly in the regime of modifying macroscopic quantum phases through coupling to light, although some initial experiments do seem to be promising [157, 158, 159, 160].

Appendix A

High-Field THz on LSCO-MM

Although the temperature dependence of the JPM gives the ability to clearly demonstrate coupling by tuning the JPM frequency, it is true that other properties, such as quasiparticle contributions which could contribute to damping, also vary with temperature. Another route to tune the JPM response is to use high-field THz pulses. Due to the JPM being governed by the Josephson equations, the application of a large electric field causes a redshift of the JPM, as discussed in Chapter 3. The high-field THz reflectivity of the LSCO crystal is shown in figure A.1a, and a clear redshift of the JPM with applied field strength can be seen. The high-field THz reflectivity of the MM-LSCO systems are shown in Fig. A.1b,c for the 200nm and 9um tapes, respectively. In both of these cases it can be seen that the lower polariton feature, 0.5Thz renormalized from the bare JPM, also shows the same characteristic redshift with applied field strength. This is a further demonstration of the coupling between the metamaterial resonances and the JPM, and that the lower polariton seen in reflectivity has mixed JPM-MM resonance character.
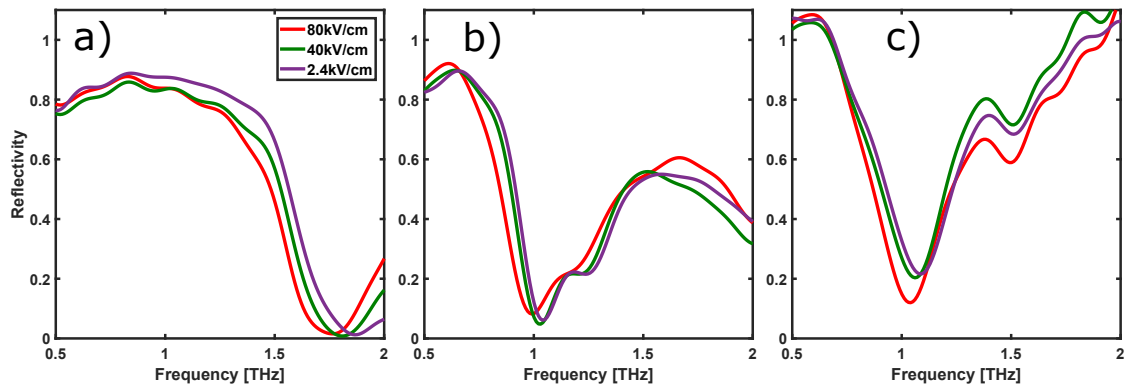
Figure A.1: a) Experimental high-field terahertz reflectivity measurements of the bare LSCO crystal. b) Experimental high-field THz of the MRA on LSCO with the resonators 200nm from the LSCO surface. c) Experimental high-field THz of the MRA on LSCO with the resonators $9\mu m$ from the LSCO surface.

Bibliography

[1] K. Kaj, K. A. Cremin, I. Hammock, J. Schalch, D. N. Basov, and R. D. Averitt, "Terahertz third harmonic generation in c-axis $La_{1.85}Sr_{0.15}CuO_4$," no. 107, p. L140504, 2023.

[2] J. Zhang and R. Averitt, "Dynamics and control in complex transition metal oxides," *Annual Review of Materials Research*, vol. 44, pp. 19–43, July 2014.

[3] C. Ahn, A. Cavalleri, A. Georges, S. Ismail-Beigi, A. J. Millis, and J.-M. Triscone, "Designing and controlling the properties of transition metal oxide quantum materials," *Nature Materials*, no. 20, pp. 1462–1468, 2021.

[4] D. N. Basov, R. D. Averitt, and D. Hsieh, "Towards properties on demand in quantum materials," *Nature Materials*, vol. 16, pp. 1077–1088, Oct. 2017.

[5] H. Y. Hwang, S. Fleischer, N. C. Brandt, B. G. Perkins, M. Liu, K. Fan, A. Sternbach, X. Zhang, R. D. Averitt, and K. A. Nelson, "A review of nonlinear terahertz spectroscopy with ultrashort tabletop-laser pulses," *Journal Of Modern Optics*, vol. 62, no. 18, pp. 1447–1479, 2014.

[6] C. Kittel and P. Mceuen, *Introduction to Solid State Physics*. New York: Wiley New York, 1986.

[7] N. W. Ashcroft and N. D. Mermin, *Solid State Physics*. Philadelphia: Saunders College, 1976.

[8] P. Drude, "Zur Elektronentheorie der Metalle," *Annalen Der Physik*, vol. 306, no. 3, p. 566, 1900.

[9] E. Abreu, M. Liu, J. Lu, K. G. West, S. Kittiwatanakul, W. Yin, S. A. Wolf, and R. D. Averitt, "THz spectroscopy of VO_2 epitaxial films: controlling the anisotropic properties through strain engineering," *New Journal of Physics*, no. 14, p. 083026, 2012.

[10] E. Abreu, S. Wang, J. G. Ramirez, M. Liu, J. Zhang, K. Geng, I. K. Schuller, and R. D. Averitt, "Dynamic conductivity scaling in photoexcited V_2O_3 thin films," *Physical Review B*, no. 92, p. 085130, 2015.

[11] E. Abreu, D. Meyers, V. K. Thorsmolle, J. Zhang, X. Liu, K. Geng, J. Chakhalian, and R. D. Averitt, "Nucleation and Growth Bottleneck in the Conductivity Recovery Dynamics of Nickelate Ultrathin Films," *ACS Nano Letters*, vol. 10, no. 20, pp. 7422–7428, 2020.

[12] Y. Huang, X. Wu, J. Schalch, G. Duan, C. Chen, X. Zhao, K. Kaj, H. Zhang, R. Engel-Herbert, R. D. Averitt, and X. Zhang, "Complementary Vanadium Dioxide Metamaterial with Enhanced Modulation Amplitude at Terahertz Frequencies," *Physical Review Applied*, no. 18, p. 054086, 2022.

[13] T. Jeon and D. Grischkowsky, "Characterization of optically dense, doped semiconductors by reflection THz time domain spectroscopy," *Applied Physics Letters*, no. 72, pp. 3032–3034, 1998.

[14] J. Hubbard, "Electron correlations in narrow energy bands," *Proceedings of the Royal Society of London*, vol. 1365, no. 1365, p. 238, 1963.

[15] T. Lancaster and S. J. Blundell, *Quantum Field Theory for the Gifted Amateur*. Oxford: Oxford University Press, 2014.

[16] G. Kotliar and D. Vollhardt, "Strongly Correlated Materials: Insights From Dynamical Mean Field Theory," *Physics Today*, vol. 57, no. 3, pp. 53–59, 2004.

[17] S. Nakatsuji and Y. Maeno, "Quasi-Two-Dimensional Mott Transition System $Ca_{2-x}Sr_xRuO_4$," *Physical Review Letters*, vol. 84, no. 12, p. 2666, 2000.

[18] C. S. Alexander, G. Cao, V. Dobrosavljevic, S. McCall, J. E. Crow, E. Lochner, and R. P. Guertin, "Destruction of the Mott insulating ground state of Ca_2RuO_4 by a structural transition," *Physical Review B*, vol. 60, no. 12, p. R8422, 1999.

[19] E. Gorelov, M. Karolak, T. O. Wehling, F. Lechermann, A. I. Lichtenstein, and E. Pavarini, "Nature of the Mott Transition in Ca_2RuO_4," *Physical Review Letters*, no. 104, p. 226401, 2010.

[20] F. Nakamura, M. Sakaki, Y. Yamanaka, S. Tamaru, T. Suzuki, and Y. Maeno, "Electric-field-induced metal maintained by current of the Mott Insulator Ca_2RuO_4," *Scientific Reports*, no. 3, p. 2536, 2013.

[21] J. Y. Zhang, E. Kim, H. Mikheev, A. J. Hauser, and S. Stemmer, "Key role of lattice symmetry in the metal-insulator transition of $NdNiO_3$ films," *Scientific Reports*, no. 6, p. 23652, 2016.

[22] J. L. Garcia-Munoz, M. A. G. Aranda, J. A. Alonso, and M. J. Martinez-Lope, "Structure and charge order in the antiferromagnetic band-insulating phase of $NdNiO_3$," *Physical Review B*, no. 79, p. 134432, 2009.

[23] A. Zylbersztejn and N. F. Mott, "Metal-insulator transition in vanadium dioxide," *Physical Review B*, no. 11, p. 4383, 1975.

[24] R. M. Mentzcovitch, W. W. Schulz, and P. B. Allen, "VO_2: Peierls or Mott-Hubbard? A view from band theory," *Physical Review Letters*, no. 72, p. 3389, 1994.

[25] H. V. Keer, D. L. Dickerson, H. Kuwamoto, H. L. C. B. Barros, and J. M. Honig, "Heat capacity of pure and doped V_2O_3 single crystals," *Journal of Solid State Chemistry*, vol. 19, no. 1, pp. 95–102, 1976.

[26] C. Dietl, S. K. Sinha, G. Christiani, Y. Khaydukov, T. Keller, D. Putzky, S. Ibrahimkutty, P. Wochner, G. Logvenov, P. A. Van Aken, B. J. Kim, and B. Keimer, "Tailoring the electronic properties of Ca_2RuO_4 via epitaxial strain," *Applied Physics Letters*, no. 112, p. 031902, 2018.

[27] A. Verma, D. Golez, O. Y. Gorobtsov, K. Kaj, R. Russell, J. Z. Kaaret, E. Lamb, G. Khalsa, H. P. Nair, Y. Sun, R. Bouck, N. Schreiber, J. P. Ruf, V. Ramaprasad, Y. Kubota, T. Togashi, V. A. Stoica, H. Padmanabhan, J. W. Freeland, N. A. Benedek, O. Shpyrko, J. W. Harter, R. D. Averitt, D. G. Schlom, K. M. Shen, A. J. Millis, and A. Singer, "Picosecond volume expansion drives a later-time insulator-metal transition in a nano-textured Mott Insulator," 2023.

[28] M. Tinkham, *Introduction to Superconductivity*. New York: McGraw-Hill, 1996.

[29] J. Bardeen, L. N. Cooper, and J. R. Schrieffer, "Theory of Superconductivity," *Physical Review*, vol. 108, no. 5, p. 1175, 1957.

[30] M. Van Camp, O. de Viron, L. Metivier, B. Meurers, and O. Francies, "The quest for a consistent signal in ground and GRACE gravity time-series," *Geophysical Journal International*, vol. 197, no. 1, pp. 192–201, 2014.

[31] F. London and H. London, "The Electromagnetic Equations of the Supraconductor," *Proceedings of the Royal Society A*, vol. 149, no. 866, pp. 71–88, 1935.

[32] D. Tanner, *Optical Effects in Solids*. Cambridge: Cambridge University Press, 2019.

[33] B. D. Josephson, "Possible new effects in superconductive tunnelling," *Physics Letters*, vol. 1, no. 7, pp. 251–253, 1962.

[34] J. Bednorz and K. Müller, "Possible high T c superconductivity in the Ba—La—Cu—O system Springer Netherlands, 1986. 267-271.," vol. 193, no. Ten Years of Superconductivity: 1980–1990, p. 5, 1986.

[35] B. Keimer, S. A. Kivelson, M. R. Norman, S. Uchida, and J. Zaanen, "From quantum matter to high-temperature superconductivity in copper oxides," *Nature*, no. 518, pp. 179–186, 2015.

[36] K. Tamasaku, Y. Nakamura, and S. Uchida, "Charge dynamics across the CuO_2 planes in $La_{2-x}Sr_xCuO_4$," *Physical Review Letters*, vol. 69, pp. 1455–1458, Aug. 1992.

[37] Y. Laplace and A. Cavalleri, "Josephson plasmonics in layered superconductors," *Advances in Physics: X*, vol. 1, no. 3, pp. 387–411, 2016.

[38] J. Aumentado, "Superconducting Parametric Amplifiers: The State of the Art in Josephson Parametric Amplifiers," *IEEE Microwave Magazine*, vol. 21, no. 8, pp. 45–59, 2020.

[39] S. Rajasekaran, E. Casandruc, Y. Laplace, D. Nicoletti, G. D. Gu, S. R. Clark, D. Jaksch, and A. Cavalleri, "Parametric amplification of a superconducting plasma wave," *Nature Physics*, vol. 12, no. 11, pp. 1012–1016, 2016.

[40] S. L. Dexheimer, *Terahertz Spectroscopy Principles and Applications*. CRC Press, 2007.

[41] F. Blanchard, L. Razzari, H. Bandulet, G. Sharma, R. Morandotti, J. C. Kieffer, T. Ozaki, M. Reid, H. F. Tiedje, H. K. Haugen, and F. A. Hegmann, "Generation of 1.5 µJ single-cycle terahertz pulses by optical rectification from a large aperture ZnTe crystal," *Optics Express*, vol. 15, no. 20, p. 13212, 2007.

[42] H. Hirori, A. Doi, F. Blanchard, and K. Tanaka, "Single-cycle terahertz pulses with amplitudes exceeding 1 MV/cm generated by optical rectification in $LiNbO_3$," *Applied Physics Letters*, vol. 98, no. 9, 2011.

[43] C. Rader, Z. B. Zaccardi, S. H. H. Ho, K. G. Harrell, P. K. Peterson, M. F. Nielson, H. Stephan, N. K. Green, D. J. H. Ludlow, M. J. Lutz, S. J. Smith, D. J. Michaelis, and J. A. Johnson, "A New Standard in High-Field Terahertz Generation: the Organic Nonlinear Optical Crystal PNPA," *ACS Photonics*, vol. 11, no. 9, pp. 3720–3726, 2022.

[44] C. Ruchert, C. Vicario, and C. P. Hauri, "Scaling submillimeter single-cycle transients toward megavolts per centimeter field strength via optical rectification in the organic crystal OH1," *Optics Letters*, vol. 5, no. 37, pp. 899–901, 2012.

[45] C. P. Hauri, C. Ruchert, C. Vicario, and F. Ardana-Lamas, "Strong-field single-cycle THz pulses generated in an organic crystal," *Applied Physics Letters*, vol. 16, no. 99, p. 161116, 2011.

[46] I. C. Tangen, G. A. Valdivia-Berroeta, Z. B. Heki, L. K. andZaccardi, E. W. Jackson, C. B. Bahr, D. J. Michaelis, and J. A. Johnson, "Comprehensive characterization of terahertz generation with the organic crystal BNA," *Journal of the OPtical SOciety of America B*, vol. 38, no. 9, pp. 2780–2785, 2021.

[47] J. Hebling, A. G. Stepanov, G. Almási, B. Bartal, and J. Kuhl, "Tunable THz pulse generation by optical rectification of ultrashort laser pulses with tilted pulse fronts," *Applied Physics B: Lasers and Optics*, vol. 78, no. 5, pp. 593–599, 2004.

[48] J. Larmor, "On the theory of the magnetic influence on spectra; and on the radiation form moving ions," *The London, Edinburgh, and Dublin Philosophical Magazine and Journal of Science*, vol. 44, no. 271, pp. 503–512, 1897.

[49] Y. S. Lee, *Principles of Terahertz Science and Technology.* New York: Springer New York, 2009.

[50] R. Shimano, S. Watanabe, and R. Matsunaga, "Intense terahertz pulse-induced nonlinear responses in carbon nanotubes," *Journal of Infrared, Millimeter, and Terahertz Waves*, vol. 33, no. 8, pp. 861–869, 2012.

[51] A. Pashkin, C. Kubler, H. Ehrke, R. Lopez, A. Halabica, R. F. Haglund Jr., R. Huber, and A. Leitenstorfer, "Ultrafast insulator-metal transition in VO_2 studied by multiterahertz spectroscopy," *Physical Review B*, no. 83, p. 195120, 2011.

[52] R. D. Averitt, G. Rodriguez, J. L. W. Siders, S. A. Trugman, and A. J. Taylor, "Conductivity artifacts in the optical-pump THz-probe measurements of $YBa_2Cu_3O_7$," *Journal of the Optical Society of America B*, no. 2, pp. 327–331.

[53] R. H. M. Groeneveld, R. Sprik, and A. Lagendijk, "Femtosecond spectroscopy of electron-electron and electron-phonon energy relaxation in Ag and Au," *Physical Review B*, vol. 51, no. 17, p. 11433, 1995.

[54] S. J. Zhang, Z. X. Wang, H. Xiang, X. Yao, Q. M. Liu, L. Y. Shi, T. Lin, T. Dong, D. Wu, and N. L. Wang, "Photoinduced Nonequilibrium Response in Underdoped YBa2Cu3 O6+x Probed by Time-Resolved Terahertz Spectroscopy," *Physical Review X*, vol. 10, no. 1, pp. 1–9, 2020.

[55] M. Knorr, J. Raab, M. Tauer, P. Merkl, D. Peller, E. Wittmann, E. Riedle, C. Lange, and R. Huber, "Phase-locked multi-terahertz electric fields exceeding 13 MV/cm at a 190 kHz repetition rate," *Optics Letters*, vol. 42, no. 21, pp. 4367–4370, 2017.

[56] R. Huber, A. Brodschelm, F. Tauser, and A. Leitenstorfer, "Generation and field-resolved detection of femtosecond electromagnetic pulses tunable up to 41 THz," *Applied Physics Letters*, vol. 76, no. 22, pp. 3191–3193, 2000.

[57] Z. K. Liu, J. Jian, B. Zhou, Z. J. Wang, Y. Zhang, H. M. Weng, D. Prabhakaran, S. K. Mo, H. Peng, P. Dudin, T. Kim, M. Hoesch, Z. Fang, X. Dai, Z. X. Shen, D. L. Feng, Z. Hussain, and Y. L. Chen, "A stable three-dimensional topological Dirac semimetal Cd_3As_2," *Naure Materials*, no. 13, pp. 677–681, 2014.

[58] B. Cheng, N. Kanda, T. N. Ikeda, T. Matsuda, P. Xia, T. Schummann, S. Stemmer, J. Itatani, N. P. Armitage, and R. Matsunaga, "Efficient Terahertz Harmonic Generation with Coherent Acceleration of Electrons in the Dirac Semimetal Cd_3As_2," *Physical Review Letters*, no. 124, p. 117402, 2020.

[59] A. de la Torre, D. M. Kennes, M. Claassen, S. Gerber, J. W. McIver, and M. A. Sentef, "Colloquium: Nonthermal pathways to ultrafast control in quantum materials," *Reviews of Modern Physics*, vol. 93, Oct. 2021.

[60] T. Kampfrath, K. Tanaka, and K. A. Nelson, "Resonant and nonresonant control over matter and light by intense terahertz transients," *Nature Photonics*, vol. 7, pp. 680–690, Aug. 2013.

[61] M. Liu, H. Y. Hwang, H. Tao, A. C. Strikwerda, K. Fan, G. R. Keiser, A. J. Sternbach, K. G. West, S. Kittiwatanakul, J. Lu, S. A. Wolf, F. G. Omenetto, X. Zhang, K. A. Nelson, and R. D. Averitt, "Terahertz-field-induced insulator-to-metal transition in vanadium dioxide metamaterial," *Nature*, vol. 487, pp. 345–348, July 2012.

[62] T. F. Nova, A. S. Disa, M. Fechner, and A. Cavalleri, "Metastable ferroelectricity in optically strained $SrTiO_3$," *Science*, vol. 364, pp. 1075–1079, June 2019.

[63] R. Matsunaga, N. Tsuji, H. Fujita, A. Sugioka, K. Makise, Y. Uzawa, H. Terai, Z. Wang, H. Aoki, and R. Shimano, "Light-induced collective pseudospin precession resonating with Higgs mode in a superconductor," *Science*, vol. 345, no. 6201, pp. 1145–1149, 2014.

[64] R. Matsunaga and R. Shimano, "Nonlinear terahertz spectroscopy of Higgs mode in s-wave superconductors," *Physica Scripta*, vol. 92, no. 2, 2017.

[65] T. Cea, C. Castellani, and L. Benfatto, "Nonlinear optical effects and third-harmonic generation in superconductors: Cooper pairs versus higgs mode contribution," *Physical Review B*, vol. 93, May 2016.

[66] D. Pekker and C. Varma, "Amplitude/Higgs Modes in Condensed Matter Physics," *Annual Review of Condensed Matter Physics*, vol. 6, no. 1, pp. 269–297, 2015.

[67] N. Tsuji and H. Aoki, "Theory of Anderson pseudospin resonance with Higgs mode in superconductors," *Physical Review B*, vol. 92, no. April 2014, p. 064508, 2015.

[68] K. Katsumi, N. Tsuji, Y. I. Hamada, R. Matsunaga, J. Schneeloch, R. D. Zhong, G. D. Gu, H. Aoki, Y. Gallais, and R. Shimano, "Higgs Mode in the d -Wave Superconductor $Bi_2Sr_2CaCu_2O_{8+x}$ Driven by an Intense Terahertz Pulse," *Physical Review Letters*, vol. 120, no. 11, p. 117001, 2018.

[69] R. Shimano and N. Tsuji, "Higgs mode in superconductors," *Annual Review of Condensed Matter Physics*, vol. 11, pp. 103–124, Mar. 2020.

[70] H. Chu, M.-J. Kim, K. Katsumi, S. Kovalev, R. D. Dawson, L. Schwarz, N. Yoshikawa, G. Kim, D. Putzky, Z. Z. Li, H. Raffy, S. Germanskiy, J.-C. Deinert, N. Awari, I. Ilyakov, B. Green, M. Chen, M. Bawatna, G. Cristiani, G. Logvenov, Y. Gallais, A. V. Boris, B. Keimer, A. P. Schnyder, D. Manske, M. Gensch, Z. Wang, R. Shimano, and S. Kaiser, "Phase-resolved higgs response in superconducting cuprates," *Nature Communications*, vol. 11, Apr. 2020.

[71] C. Vaswani, J. H. Kang, M. Mootz, L. Luo, X. Yang, C. Sundahl, D. Cheng, C. Huang, R. H. J. Kim, Z. Liu, Y. G. Collantes, E. E. Hellstrom, I. E. Perakis, C. B. Eom, and J. Wang, "Light quantum control of persisting higgs modes in iron-based superconductors," *Nature Communications*, vol. 12, Jan. 2021.

[72] D. Basov and T. Timusk, "Electrodynamics of high-Tc superconductors," *Rev. Mod. Phys.*, vol. 77, no. April, pp. 721–779, 2005.

[73] S. Savel'ev, V. A. Yampol'skii, A. L. Rakhmanov, and F. Nori, "Terahertz josephson plasma waves in layered superconductors: spectrum, generation, nonlinear and quantum phenomena," *Reports on Progress in Physics*, vol. 73, p. 026501, Jan. 2010.

[74] S. Rajasekaran, J. Okamoto, L. Mathey, M. Fechner, V. Thampy, G. D. Gu, and A. Cavalleri, "Probing optically silent superfluid stripes in cuprates," *Science*, vol. 359, pp. 575–579, Feb. 2018.

[75] F. Gabriele, M. Udina, and L. Benfatto, "Non-linear terahertz driving of plasma waves in layered cuprates," *Nature Communications*, vol. 12, Feb. 2021.

[76] J. Hebling, G. Almasi, I. Kozma, and J. Kuhl, "Velocity matching by pulse front tilting for large area THz-pulse generation," *Optics Express*, vol. 10, p. 1161, Oct. 2002.

[77] J. Hebling, K.-L. Yeh, M. C. Hoffmann, and K. A. Nelson, "High-power THz generation, THz nonlinear optics, and THz nonlinear spectroscopy," *IEEE Journal of Selected Topics in Quantum Electronics*, vol. 14, no. 2, pp. 345–353, 2008.

[78] I. Tanaka, K. Yamane, and H. Kojima, "Single crystal growth of superconducting La2-xSrxCuO4 by the TSFZ method," *Journal of Crystal Growth*, vol. 96, no. 3, pp. 711–715, 1989.

[79] S. V. Dordevic, S. Komiya, Y. Ando, and D. N. Basov, "Josephson Plasmon and Inhomogeneous Superconducting State in La 2-xSrxCuO4," *Physical Review Letters*, vol. 91, no. 16, pp. 1674011–1674014, 2003.

[80] K. I. Sim, Y. C. Jo, T. Ha, J. H. Kim, and J. H. Kim, "Terahertz Electrodynamics and Superconducting Energy Gap of NbN," *Journal of the Korean Physical Society*, vol. 71, no. 9, pp. 571–574, 2017.

[81] Y. Yuan, P. Kissin, D. Puggioni, K. Cremin, S. Lei, Y. Wang, Z. Mao, J. M. Rondinelli, R. D. Averitt, and V. Gopalan, "Ultrafast quasiparticle dynamics in the correlated semimetal Ca3Ru2O7," *Physical Review B*, vol. 99, no. 15, p. 155111, 2019.

[82] J. S. Schalch, K. Post, G. Duan, X. Zhao, Y. D. Kim, J. Hone, M. M. Fogler, X. Zhang, D. N. Basov, and R. D. Averitt, "Strong Metasurface–Josephson Plasma Resonance Coupling in Superconducting La$_{2-x}$Sr$_x$CuO$_4$," *Advanced Optical Materials*, vol. 7, no. 21, pp. 1–8, 2019.

[83] F. Gabriele, M. Udina, and L. Benfatto, "Non-linear Terahertz driving of plasma waves in layered cuprates," *Nature Communications*, no. 12, p. 752, 2021.

[84] H. Chu, S. Kovalev, Z. X. Wang, L. Schwarz, T. Dong, L. Feng, R. Haenel, M. J. Kim, P. Shabestari, H. L. Phuong, K. Honasoge, R. D. Dawson, D. Putzky, G. Kim, M. Puviani, M. Chen, N. Awari, A. N. Ponomaryov, I. Ilyakov, M. Bluschke, F. Boschini, M. Zonno, S. Zhdanovich, M. Na, G. Christiani, G. Logvenov, D. J. Jones, A. Damascelli, M. Minola, B. Keimer, D. Manske, N. L. Wang, J. C. Deinert, and S. Kaiser, "Fano interference between collective modes in cuprate high-T$_c$ superconductors," *Nature Communications*, no. 1, p. 1343, 2023.

[85] R. Matsunaga and R. Shimano, "Nonequilibrium BCS state dynamics induced by intense terahertz pulses in a superconducting NbN film," *Physical Review Letters*, vol. 109, no. 18, pp. 3–7, 2012.

[86] S. Nakamura, Y. Iida, Y. Murotani, R. Matsunaga, H. Terai, and R. Shimano, "Infrared activation of Higgs mode by supercurrent injection in a superconductor NbN," *preprint*, pp. 1–5, 2018.

[87] S. J. Zhang, Q. M. Liu, Z. Sun, Z. X. Wang, Q. Wu, L. Yue, S. X. Xu, T. C. Hu, R. S. Li, X. Y. Zhou, J. Y. Yuan, G. D. Gu, T. Don, and N. L. Wang, "Out-of-plane nonlinear optical responses of superconducting cuprates detected by Terahertz pump-Terahertz probe spectroscopy," *preprint*, 2022.

[88] A. Schiffrin, T. Paasch-Colber, N. Karpowicz, V. Apalkvo, D. Gerster, M. Muhlbrandt, M. Korbman, J. Reichert, M. Schultze, S. Holzner, J. V. Barth, R. Kienberger, R. Ernstorfer, V. S. Yakovlev, M. I. Stockman, and F. Krausz, "Optical-field-induced current in dielectrics," *Nature*, no. 493, pp. 70–74, 2013.

[89] W. Hu, S. Kaiser, D. Nicoletti, C. R. Hunt, I. Gierz, M. C. Hoomann, M. Le Tacon, T. Loew, B. Keimer, and A. Cavalleri, "Optically enhanced coherent transport in YBa$_2$Cu$_3$O$_{6.5}$ by ultrafast redistribution of interlayer coupling," *Nature Mat.*, vol. 13, no. July, p. 705, 2014.

[90] F. Schlawin, D. M. Kennes, and M. A. Sentef, "Cavity quantum materials," *Applied Physics Review*, no. 9, p. 011312, 2022.

[91] Y. Ashida, A. Imamoglu, J. Faist, D. Jaksch, A. Cavalleri, and E. Demler, "Quantum electrodynamic control of matter: cavity-enhanced ferroelectric phase transition," *Physical Review X*, no. 10, p. 041027, 2020.

[92] S. Latini, D. Shin, S. A. Sato, C. Schafer, U. D. Giovannini, H. Hubener, and A. Rubio, "The ferroelectric photo ground state of $SrTiO_3$:cavity materails engineering," *Proceedings of the National Academy of Sciences*, no. 118, p. e2105618118, 2021.

[93] Y. Laplace, S. Fernandez-Pena, S. Gariglio, J. M. Triscone, and A. Cavalleri, "Proposed cavity Josephson plasmonics with complex-oxide heterostructures," *Physical Review B*, vol. 93, no. 7, pp. 1–6, 2016.

[94] H. Hubener, U. D. Giovannini, C. Schafer, J. Andberger, M. Ruggenthaler, J. Faist, and A. Rubio, "Engineering quantum materials with chiral optical cavities," *Nature Materials*, no. 20, pp. 438–442, 2021.

[95] M. V. Fistul and A. V. Ustinov, "Quantum Cavity modes in spatially extended Josephson systems," *Physical Review B*, no. 75, p. 214506, 2007.

[96] J. Hammer, M. Aprili, and I. Petkovic, "Microwave Cooling of Josephson Plasma Oscillations," *Physical Review Letters*, no. 107, p. 214506, 2007.

[97] S. J. Denny, S. R. Clark, Y. Laplace, A. Cavalleri, and D. Jaksch, "Proposed Parametric Cooling of Bilayer Cuprate Superconductors by Terahertz Excitation," *Physical Review Letters*, no. 114, p. 137001, 2015.

[98] R. Hoppner, B. Zhu, T. Rexin, A. Cavalleri, and L. Mathey, "Dynamical redistribution of phase fluctuations in bi-layer superconductors by periodic driving with an optical field," *Physical Review B*, no. 91, p. 104507, 2015.

[99] A. M. Jayich, J. C. Sankey, B. M. Zwickl, C. Yang, J. D. Thompson, S. M. Girvin, A. A. Clerk, F. Marquardt, and J. G. E. Harris, "Dispersive optomechanics: a membrane inside a cavity," *New Journal of PHysics*, no. 10, p. 095008, 2008.

[100] J. D. Thompson, B. M. Zwickl, A. M. Jayich, F. Marquardt, S. M. Girvin, and J. G. E. Harris, "Strong dispersive coupling of a high-finesse cavity to a micromechanical membrane," *Nature*, vol. 72, no. 452, pp. 13864–13878, 2008.

[101] A. Nunnenkamp, K. Borkje, J. G. E. Harris, and S. M. Girvin, "Cooling and squeezing via quadratic optomechanical coupling," *Physical Review A*, no. 82, p. 021806, 2010.

[102] F. Marquardt, J. P. Chen, A. A. Clerk, and S. M. Girvin, "Quantum Theory of Cavity-Assisted Sideband Cooling of Mechanical Motion," *Physical Review Letters*, no. 99, p. 093902, 2007.

[103] K. A. Cremin, J. Zhang, C. C. Homes, G. D. Gu, Z. Sun, M. M. Fogler, A. J. Millis, D. N. Basov, and R. D. Averitt, "Photoenhanced metastable c-axis electrodynamics in stripe-ordered cuprate $La_{1.885}Ba_{0.115}CuO_4$," *Proceedings of the National Academy of Sciences of the United States of America*, vol. 116, no. 40, pp. 19875–19879, 2019.

[104] K. Fan, R. D. Averitt, and W. J. Padilla, "Active and tunable nanophotnonic metamaterials," *Nanophotonics*, vol. 11, no. 17, pp. 3769–3803, 2022.

[105] X. Chen, W. Fan, X. Jian, and H. Yan, "High-Q Toroidal Dipole Metasurfaces Driven By Bound States in the Continuum for Ultrasensitive Terahertz Sensing," *Journal of Lightwave Technology*, vol. 40, no. 7, pp. 2181–2190, 2022.

[106] L. Cong and R. Singh, "Symmetry-Protected Dual Bound States in the Continuum in Metamaterials," *Advanced Optical Materials*, no. 7, p. 1900383, 2019.

[107] I. Yokota, "On the Coupling between Optical Lattice Vibrations and Carrier Plasma Oscillations in Polar Semiconductors," *Journal of the Physical Society of Japan*, no. 16, p. 2075, 1961.

[108] A. Mooradian and G. B. Wright, "Observation of the interaction of plasmons with longitudinal optical phonons in GaAs," *Physical Review Letters*, no. 16, p. 999, 1966.

[109] A. Mooradian and A. L. McWhorter, "Polarization and intensity of Raman Scattering from plasmons and phonons in gallium arsenide," *Physical Review Letters*, no. 19, p. 849, 1967.

[110] B. Tell and R. J. Martin, "Raman Scattering by coupled optical-phonon-plasmon modes in GaAs," *Physical Review*, no. 167, p. 381, 1968.

[111] C. Chen, S. Can, J. Schalch, X. Zhao, G. Duan, R. D. Averitt, and X. Zhang, "Ultrathin terahertz triple-band metamaterial absorbers: consideration of interlayer coupling," *Physical Review Applied*, no. 14, p. 054021, 2020.

[112] K. Cong, Q. Zhang, Y. Wang, G. T. Noe, A. Belyanin, and J. Kono, "Dicke superradiance in solids," *Journal of the Optical Society of America B*, vol. 33, no. 7, pp. C80–C101, 2016.

[113] X. Li, M. Bamba, Q. Zhang, S. Fallahi, G. C. Gardner, W. Gao, M. Lou, K. Yoshioka, M. J. Manfra, and J. Kono, "Vacuum Bloch-Siegert shift in landau polaritons with ultra-high cooperativity," *Nature Photonics*, no. 12, pp. 324–329, 2018.

[114] Y. Maeno, H. Hashimoto, K. Yoshida, S. Nishizaki, T. Fujita, J. G. Bednorz, and F. Lichtenberg, "Superconductivity in a layered perovskite without copper," *Nature*, no. 372, pp. 532–534, 1994.

[115] M. C. Lee, C. H. Kim, I. Kwak, J. Kim, S. Yoon, B. C. Park, B. Lee, F. Nakamura, C. Sow, Y. Maeno, T. W. Noh, and K. W. Kim, "Abnormal phase flip in the coherent phonon oscillations of Ca_2RuO_4," *Physical Review B*, no. 98, p. 161115, 2018.

[116] X. Li, H. Ning, O. Mehio, H. Zhao, M. C. Lee, K. W. Kim, F. Nakamura, Y. Maeno, Y. Cao, G. Cao, and D. Hsieh, "Keldysh space control of charge dynamics in a strongly driven Mott insulator," *Physical Review Letters*, no. 128, p. 187402, 2022.

[117] H. Ning, *Ultrafast Optical Control of Order Parameters in Quantum Materials*. PhD thesis, California Institute of Technology, 2023.

[118] A. Tsurumaki-Fukuchi, K. Tsubaki, T. Katase, T. Kamiya, M. Arita, and Y. Takahashi, "Stable and Tunable Current-Induced Phase Transition in Epitaxial Thin Films of Ca_2RuO_4," *ACS Applied Material Interfaces*, vol. 25, no. 12, pp. 28368–28374, 2020.

[119] L. Miao, P. Silwal, X. Zhou, I. Stern, J. Peng, W. Zhang, L. Spinu, Z. Mao, and D. H. Kim, "Itinerant ferromagnetism and geometrically suppressed metal-insulator transition in epitaxial thin films of Ca_2RuO_4," *Applied Physics Letters*, no. 100, p. 052401, 2012.

[120] D. J. Hilton, R. P. Prasankumar, S. Fourmaux, A. Cavalleri, D. Brassard, M. A. E. Khakani, J. C. Kieffer, A. J. Taylor, and R. D. Averitt, "Enhanced Photosusceptibility near T_c for the Light-Induced Insulator-to-Metal Phase Transition in Vanadium Dioxide," *Physical Review Letters*, no. 99, p. 226401, 2007.

[121] M. K. Liu, B. Pardo, J. Zhang, M. M. Qazilbash, S. J. Yun, Z. Fei, J. H. Shin, H. T. Kim, D. N. Basov, and R. D. Averitt, "Photoinduced phase transitions by time-resolved far-infrared spectroscopy in V_2O_3," *Physical Review Letters*, vol. 107, no. 6, p. 066403, 2011.

[122] P. Papon, J. Leblond, and P. H. E. Meijer, *Advanced Texts in Physics*, ch. The Physics of Phase Transitions: Concepts and Applications, pp. 37-55. Springer, Berlin; New York, 2000.

[123] R. A. Vitalone, A. Sternbach, B. A. Foutty, A. S. MclLeod, C. Sow, D. Golez, F. Nakamura, Y. Maeno, A. N. Pasupathy, A. Georges, A. J. MIllis, and D. N. Basov, "Nanoscale Femtosecond Dynamics of Mott Insulator $(Ca_{0.99}Sr_{0.01})_2RuO_4$," *Nano Letters*, vol. 22, no. 14, pp. 5689–5697, 20.

[124] Z. Shao, N. Schnitzer, J. Ruf, O. Y. Gorobtsov, C. Dai, B. H. Goodge, T. Yang, H. Nair, V. A. Stoica, J. W. Freeland, J. Ruff, L. Q. Chen, D. G. Schlom, K. M. Shen, L. F. Kourkoutis, and A. Singer, "Real-space imaging of polar and elastic nano-textures in thin films via inverstion of diffraction data," *arXiv:2211.01506*, 2022.

[125] K. Katsumi, Z. Z. Li, H. Raffy, Y. Gallais, and R. Shimano, "Superconducting fluctuations probed by the Higgs mode in $Bi_2Sr_2CaCu_2O_{8+x}$ thin films," *Physical Review B*, vol. 102, no. 5, p. 054510, 2020.

[126] L. S. Bilbro, R. V. Aguilar, G. Logvenov, O. Pelleg, I. Bozovic, and N. P. Armitage, "Temporal correlations of superconductivity above the transition temperature in $La_{2-x}Sr_xCuO_4$ probed by terahertz spectroscopy," *Nature Physics*, no. 7, pp. 298–302, 2011.

[127] R. Guo, S. Duan, Z. He, X. Liang, Z. Niu, M. He, Y. Jiang, J. Wu, L. Ji, B. Jin, J. Chen, H. Wang, and P. Wu, "Josephson Plasmon Resonance in $Tl_2Ba_2CaCu_2O_8$ High-Temperature Superconductor Tunable Terahertz Metamaterials," *Advanced Functional Materials*, no. 31, p. 2106891, 2021.

[128] V. K. Thorsmolle, R. D. Averitt, M. P. Maley, M. F. Hundley, A. E. Kohshelev, L. N. Bulaevskii, and A. J. Taylor, "Evidence for linelike vortex liquid phase in $Tl_2Ba_2CaCu_2O_8$ probed by the Josephson plasma resonance," *Physical Review B*, no. 66, p. 012519, 2002.

[129] V. K. Thorsmolle, R. D. Averitt, T. Shibauchi, M. F. Hundley, and A. J. Taylor, "Dynamic Coupling-Decoupling Crossover in the Current-Driven Vortex State in $Tl_2Ba_2CaCu_2O_8$ Probed by the Josephson Plasma Resonance," *Physical Review Letters*, no. 97, p. 237001, 2002.

[130] M. Budden, T. Gebert, and A. Cavalleri, "Hybrid CO2-Ti:sapphire laser with tunable pulse duration for mid-infrared-pump terahertz-probe spectroscopy," *Optics Express*, vol. 29, no. 3, pp. 3575–3583, 2021.

[131] B. Liu, H. Brombergre, A. Carella, T. Gebert, M. Forst, and A. Cavalleri, "Generation of narrowband, high-intensity, carrier-envelope phase-stable pulses tunable between 4 and 18 THz," *Optics Letters*, vol. 42, no. 1, pp. 129–131, 2017.

[132] A. Cartella, T. F. Nova, A. Oriana, G. Cerullo, M. Forst, C. Manzoni, and A. Cavalleri, "Narrowband carrier-envelope phase stable mid-infrared pulses at wavelengths beyond 10m by chirped-pulse difference frequency generation," *Optics Letters*, vol. 42, no. 4, pp. 663–666, 2017.

[133] Z. Chen, X. Zhou, C. A. Werly, and K. A. Nelson, "Generation of high power tunable multicycle terahertz pulses," *Applied Physics Letters*, no. 99, p. 071102, 2011.

[134] K. J. Tielrooij, A. Principi, D. S. Reig, A. Block, S. Varghese, S. Schreyeck, K. Brunner, G. Karczewski, I. Ilyakov, O. Ponomaryov, T. V. A. G. de Oliveira, M. CHen, J. C. Deinert, C. G. Carbonell, S. O. Valenzuela, L. W. Molenkamp, G. V. Kiessling, T. Astakhov, and S. Kovalev, "Milliwatt terahertz harmonic generation from topological insulator metamaterials," *Light: Science Applications*, vol. 11, no. 315, 2022.

[135] Y. Wen, F. Giorgianni, I. Ilyakov, B. Quan, S. Kovalev, C. Wang, C. Vicaria, J. C. Deinert, X. Xiong, J. Bailey, M. Chen, A. Ponomaryov, N. Awari, A. Rovere, J. Sun, R. Morandotti, L. Razzari, G. Aeppli, J. Li, and J. Zhou, "A universal route to efficient nonlinear response via Thomson scattering in linear solids," *National Science Review*, 2023.

[136] S. Shen, X. Liu, Y. Shen, J. Qu, E. Pickwell-MacPherson, X. Wei, and Y. Sun, "Recent Advances in the Development of Materials for Terahertz Metamaterial Sensing," *Advanced Optical Materials*, vol. 10, no. 1, p. 210108, 2022.

[137] W. Xu, L. Xie, and Y. Ying, "Mechanisms and applications of terahertz metamaterial sensing: a review," *Nanoscale*, no. 9, pp. 13864–13878, 2017.

[138] V. Rokaj, M. Penz, M. A. Sentef, M. Ruggenthaler, and A. Rubio, "Polaritonic Hofstadter butterfly and cavity control of the quantized Hall conductance," *Physical Review B*, no. 105, p. 205424, 2022.

[139] B. L. De, C. J. Eckhardt, D. M. Kennes, and M. A. Sentef, "Cavity engineering of Hubbard U via phonon polaritons," *Journal of Physics: Materials*, vol. 5, no. 2, p. 024006, 2022.

[140] J. Li and M. Eckstein, "Manipulating Intertwined Orders in Solids with Quantum Light ," *Physical Review Letters*, no. 125, p. 217402, 2020.

[141] T. Neuman, D. S. Wang, and P. Narang, "Nanomagnonic Cavities for Strong Spin-Magnon Coupling and Magnon-Mediated Spin-Spin Interactions ," *Physical Review Letters*, no. 125, p. 247702, 2020.

[142] Z. Zhang, H. Hirori, F. Sekiguchi, A. Shimazaki, Y. Iwasaki, T. Nakamura, A. Wakamiya, and Y. Kanemitsu, "Ultrastrong coupling between THz phonons and photons caused by an enhanced vacuum electric field," *Physical Review Research*, no. 3, p. L032021, 2021.

[143] D. M. Juraschek, T. Neuman, J. Flick, and P. Narang, "Cavity control of nonlinear phononics," *Physical Review Research*, no. 3, p. L032046, 2021.

[144] J. B. Curtis, A. Grankin, N. R. Poniatowski, V. M. Galitski, P. Narang, and E. Demler, "Cavity magnon-polaritons in cuprate parent compounds," *Physical Review Research*, no. 4, p. 013101, 2022.

[145] Z. Raines, A. A. Allocca, M. Hafezi, and V. M. Galitski, "Cavity Higgs polaritons," *Physical Review Research*, no. 2, p. 013143, 2020.

[146] A. Allocca, Z. M. Raines, J. B. Curtis, and V. M. Galitski, "Cavity superconductor-polaritons," *Physical Review B*, no. 99, p. 020504, 2019.

[147] J. B. Curtis, Z. M. Raines, A. A. Allocca, M. Hafezi, and V. M. Galitski, "Cavity Quantum Eliashberg Enhancement of Superconductivity," *Physical Review Letters*, no. 122, p. 167002, 2019.

[148] M. A. Sentef, M. Ruggenthaler, and A. Rubio, "Cavity quantum-electrodynamical polaritonically enhanced electron-phonon coupling and its influence on superconductivity," *Science Advances*, vol. 4, no. 11, 2018.

[149] F. Schlawin, A. Cavalleri, and D. Jaksch, "Cavity-Mediated Electron-Photon Superconductivity," *Physical Review Letters*, no. 122, p. 133602, 2019.

[150] H. Gao, F. Schlawin, M. Buzzi, A. Cavalleri, and D. Jaksch, "Photoinduced Electron Pairing in a Driven Cavity," *Physical Review Letters*, no. 125, p. 053602, 2020.

[151] E. Bostrom, A. Sriram, M. Claassen, and A. Rubio, "Controlling the magnetic state of the proximate quantum spin liquid α-rucl$_3$ with an optical cavity," *arXiv:2211.07247*, 2022.

[152] Y. Ashida, A. Imamoglu, and E. Demler, "Cavity Quantum Electrodynamics with Hyperbolic van der Waals Materials," *arXiv:2301.03712*, 2023.

[153] M. Bialek, W. Knap, and J. P. Ansermet, "Cavity-mediated coupling of antiferromagnetic spin waves," *arXiv:2212.01129*, 2022.

[154] H. Zhang, A. Chu, C. Luo, J. K. Thompson, and A. M. Rey, "Control and amplification of Bloch oscillations via photon-mediated interactions," *arXiv:2301.08296*, 2023.

[155] G. Passetti, C. J. Eckhardt, M. A. Sentef, and D. M. Kennes, "Cavity Light-Matter Entanglement through Quantum Fluctuations," *arXiv:2212.03011*, 2022.

[156] J. B. Curtis, M. H. Michael, and E. Demler, "Local Fluctuations in Cavity Control of Ferroelectricity," *arXiv:2301.01884*, 2023.

[157] G. Jarc, "Cavity control of the metal-to-insulator transition in 1T-TaS$_2$," 2022.

[158] A. Thomas, "Large Enhancement of Ferromagnetism under a Collective Strong Coupling of YBCO Nanoparticles," *Nano Letters*, vol. 10, no. 21, pp. 4365–4370, 2021.

[159] A. Thomas, E. Devaux, K. Nagarajan, T. Chervy, M. Seidel, D. Hagenmuller, S. Schutz, J. Schachenmayer, C. Genet, G. Pupillo, and T. W. Ebbesen, "Exploring Superconductivity under Strong Coupling with the Vacuum Electromagnetic Field," 2019.

[160] H. Xu, F. Tay, A. Baydin, J. M. Moya, M. Manjappa, M. Bamba, E. Morosan, and J. Kono, "Interplay between cavity quantum electrodynamics and superconductivity." APS March Meeting, 2023.